Politecnico di Torino

Corso di Laurea Magistrale in Ingegneria Energetica e Nucleare
A.a. 2022/2023

R134a recuperation system for the resistive plate chambers at CMS experiment

Candidato:

Michele BRUNO

Politecnico di Torino

Corso di Laurea Magistrale in Ingegneria Energetica e Nucleare
A.a. 2022/2023
Sessione di Laurea Ottobre 2023

R134a recuperation system for the resistive plate chambers at CMS experiment

Relatori:

Prof. Vittorio VERDA

Prof.ssa Martina CAPONE

Dott. Roberto GUIDA

Candidato:

Michele BRUNO

Remember to look up at the stars and not down at your feet. Try to make sense of what you see and wonder about what makes the universe exist. Be curious. And however difficult life may seem, there is always something you can do and succeed at. It matters that you don't just give up.

Stephen Hawking

Abstract

A new gas recovery system for the resistive plate chambers (RPCs) at CMS (Compact Muon Solenoid) experiment was installed, commissioned, and tested to find the optimal operating configuration in terms of recovered gas quality and system efficiency. The aim of the system was the R134a recuperation, using a distillation process, to solve both the environmental and the economical issues, considering the high global warming potential, of 1430, and the high specific cost of R134a. The system works with an input mixture composed by 95.2% of R134a (1,1,1,2-Tetrafluoroethane), 4.5% of isobutane (C_4H_{10}), and 0.3% of sulfur hexafluoride (SF_6).

The recovery system was designed with four units: the electric rack, the distillation unit, the pumping unit, and the storage unit. The electric rack contains all the electrical connections, in an ATEX environment, for the system automation. The distillation unit is composed by two racks, closed in an ATEX environment, each one containing two columns for the separation process. Each column develops vertically with two buffers: the top and the bottom buffers. The top buffers are cooled down with a series connected cooling system, whose temperature is controlled by a chiller (Lauda Integral XT 280), while the bottom buffers are maintained warm with a series connected cooling system controlled by a second chiller (Huber Ministat 125). The pumping unit (Gas booster 7LG-TS-7) is devoted to the recovered gas compression to the storage unit, which consists of a stainless-steel cylindrical tank with a storage capacity of 400 kg.

The system performances were investigated in terms of buffer pressure and temperature, filling and emptying flowrates, using thermocouples, absolute and differential pressure sensors, and flowmeters. Moreover, the gas quality was analysed quantifying the isobutane concentration in the recovered mixture, through the analytical columns PPU (PoraPlotU) and MS (Molecular Sieve) 5Å of the gas chromatograph.

Firstly, the tests were performed in manual mode, filling and emptying column by column manually. Secondly, the system managed to run automatically, 24 hours per day, with a fraction of the recovered gas sent to the RPCs mixer, to reduce the flowrate of fresh R134a to the chambers. The system was tested modifying five main operating parameters: filling flowrate (200 l/h, 300 l/h, and 400 l/h), emptying flowrate (600 l/h, 700 l/h, and 1000 l/h) top buffer pressure (10 mbar, 20 mbar, 35 mbar, and 50 mbar) and temperature (-36.5 °C, -36.2 °C, and -36.0 °C), and bottom buffer temperature (14 °C, 17 °C, 20 °C, and 23 °C). According to the previous prototypes, the targeted efficiency was 80%, with an upper bound isobutane concentration of 1000 ppm.

Contents

1 Introduction

The transition to a decarbonized energy system is fundamental for holding average temperature to "well below 2 degrees Celsius above pre-industrial levels and pursuing efforts to limit the temperature increase to 1.5 degrees Celsius above the pre-industrial levels", according to the COP21 Paris Agreement [1]. This transition requires a radical transformation on the modalities of energy generation, distribution, storage, and consumption, implying deep decarbonization of transport, building and industrial sector. CERN is also involved in the mission of reducing greenhouse gas emissions, in particular fluorinated gases, which perform well in specific particles detectors as the resistive plate chambers (RPCs). Considering their good spatial and time resolutions, RPCs are well suited for fast time-spacing particle tracking as required for the muon trigger at the LHC experiments, in particular at the CMS (Compact Muon Solenoid) experiment [2].

1.1 Fluorinated gases and global warming potential

A wide range of gas mixtures is used for the operation of different gaseous detectors for particle physics research and some of these gases are recognized as greenhouse gases (GHGs).

GHGs are classified according to their Global Warming potential (GWP) [3], defined as "the climatic warming potential of a greenhouse gas relative to that of carbon dioxide ('CO2'), calculated in terms of the 100-year warming potential of one kilogram of a greenhouse gas relative to one kilogram of CO2" [4].

Unlike many other greenhouse gases, fluorinated gases have no significant natural sources and come almost entirely from human-related activities. They are emitted through their use as substitutes for ozone-depleting substances (e.g., as refrigerants) and through a variety of industrial processes such as aluminium and semiconductor manufacturing. Despite their lower emissions compared to other GHGs (Figure 3) [5], many fluorinated gases have very high global warming potentials (GWPs) and, therefore, even small atmospheric concentrations can have disproportionately large effects on global temperatures. In addition, they can also have long atmospheric lifetimes, lasting thousands of years in some cases. Like other long-lived greenhouse gases, most fluorinated gases are well-mixed in the atmosphere, spreading around the world after they are emitted, and they are removed from the atmosphere only when they are destroyed by sunlight in the far upper atmosphere. Therefore, they represent the most potent and longest lasting type of greenhouse gases emitted by human activities.

Fluorinated gases can be classified in four main categories according to their chemical structure and composition: hydrofluorocarbons (HFCs), perfluorocarbons (PFCs), sulphur hexafluoride (SF_6), and nitrogen trifluoride (NF_3) [5]. In addition, they can be classified according to their source: substitution of the ozone depleting substances (e.g., refrigerant fluids), which represents the most evident source, industrial sector, transmission, and distribution of electricity (Figure 4).

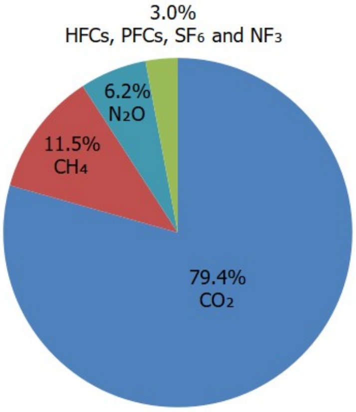

Figure 3: Total U.S. emissions in terms of carbon dioxide (CO_2), methane (CH_4), nitrous oxide (N_2O) and fluorinated gases, which represent the 3% of the overall emissions [6].

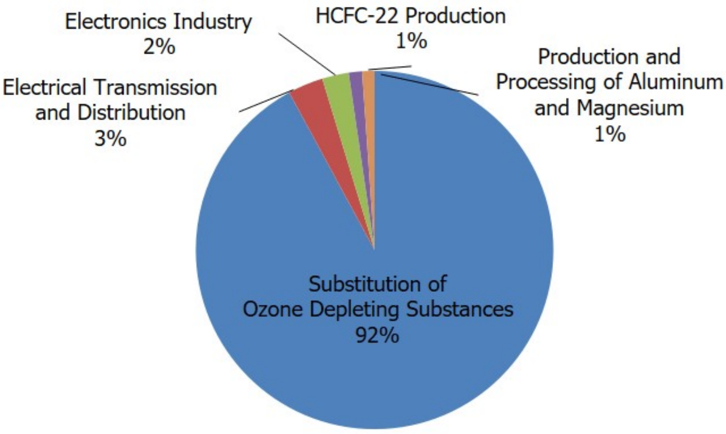

Figure 4: Total U.S. emissions estimation by source. The majority of fluorinated gas emission is the concequence of the substitution of the ozone depleting substances (92%), followed by electrical transmission and distribution (3%), electronics, aluminum and magnesium industrial sector, and HCFC-22 production (2%) [6].

The emission trend of fluorinated gases has increased since 1990, as shown in Figure 5. Considering that many fluorinated gases have a long atmospheric lifetime, it will take several years to see a noticeable reduction of their concentrations. Therefore, it is of fundamental importance the reduction of their emission, by adopting gas capture, recycling, and destruction processes, optimizing production to minimize emissions, and replacing these gases with alternative ones [5].
However, at the moment, particle detectors are forced to use fluorinated gases which allow to achieve specific performances that are absolutely needed for data taking at the LHC experiments (i.e., stability, long term performance, time resolution, rate capability, etc.). In particular, $C_2H_2F_4$ (R134a), CF_4 (R14), C_4F_{10} (R610) and SF_6,

which are combined in gas mixtures for the operation of particle detectors, have very high global warming potentials, ranging between 1430 and 23500.

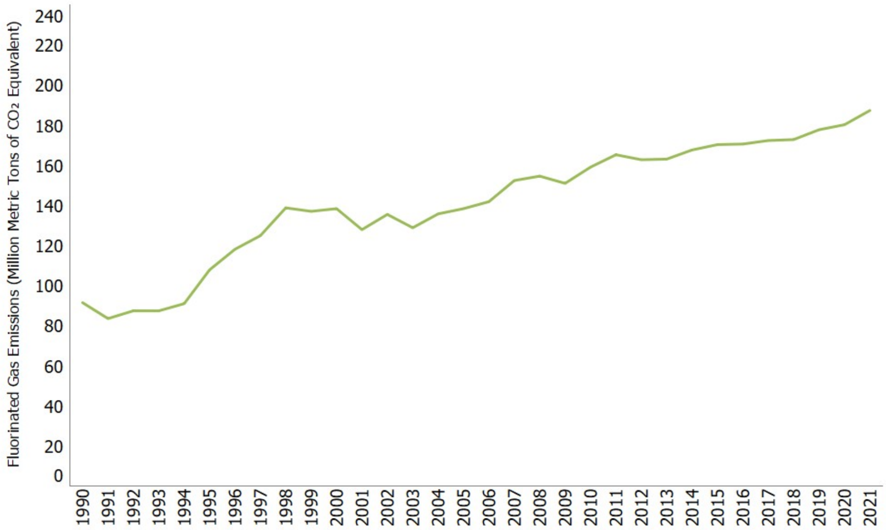

Figure 5: Fluorinated gas emissions trend from 1990 to 2021 in terms of million metric tons of CO_2 equivalent [6].

1.2 Greenhouse gas emissions at CERN

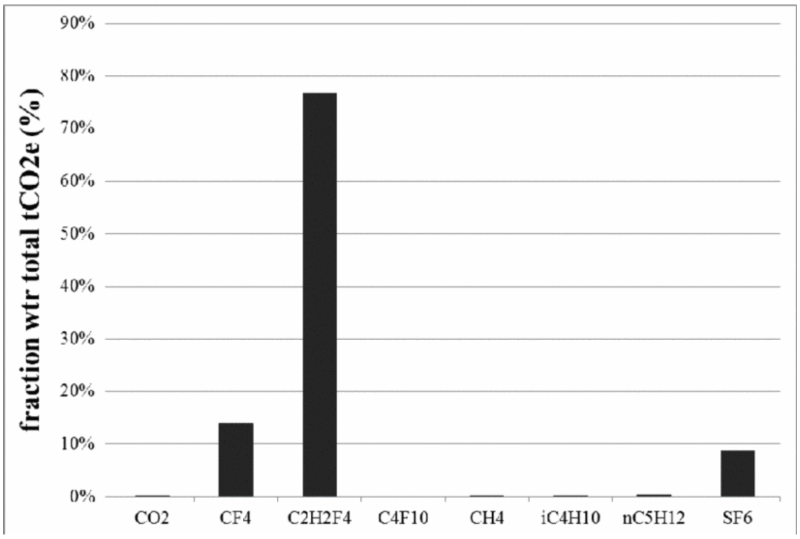

Figure 6: Contribution in percentage of different greenhouse gases to the overall emissions at CERN. The most relevant GHG is R134a ($C_2H_2F_4$), which contributes almost the 80%, followed by tetrafluoromethane (CF_4) and sulfur hexafluoride (SF_6) [7].

Greenhouse gas emission due to the detector activities at CERN contributes like a "large industrial city". In fact, the total emission at CERN is about 130000 tons of CO_2 equivalent with the main contribution coming from the R134a used by the ATLAS and CMS RPC systems (Figure 6). In order to reduce operational costs and emissions, most of the LHC gas systems were already designed to operate in recirculation mode, with an efficiency higher than 90%. [7]. However, due to the high circulation flow, the remaining 10% still contributes significantly to the overall emissions.

1.3 CERN strategies to minimize high GWP gas emissions

According to the European regulation on fluorinated greenhouse gases, CERN is involved in the reduction of GHG emissions [8]. Indeed, the gas mixture used in the RPCs contains R134a (1,1,1,2-tetrafluoroethane), C_4H_{10} (isobutane), and SF_6 (sulphur hexafluoride). R134a and SF_6 are two fluorinated gases, with global warming potentials of 1430 [9] and 23500 [10] respectively, while the isobutane, considering its low GWP (less than 5), is not controlled by the Ozone Protection and Synthetic Greenhouse Gas Management legislation [4]. Knowing that the highest percentage in the gas mixture used in the RPCs at CMS is represented by the R134a, a recuperation system of this gas or its subtitution with ”eco-gas” is needed to minimize or eliminate the GHG emission during operation.

The first strategy consists in the design of a system for the recuperation of high GWP gases (e.g., R134a used for the RPCs at CMS), by extracting, through a separation process, the greenhouse gas from the mixture used in the detectors circulation loop, allowing a further reuse and avoiding the release to the environment.

A second and a third strategy may consist of using green alternatives to the currently high GWP gases or using industrially developed plants for the disposal of greenhouse gases by decomposition in harmless compounds. However, even if this last strategy would avoid emissions to the atmosphere, it would not optimize the gas usage, without solving the economical issues related to the high specific cost of fluorinated gases [11].

2 The Large Hadron Collider

The Large Hadron Collider (LHC) is a two-ring-superconducting-hadron accelerator and collider installed in the existing 26.7 km tunnel that was constructed between 1984 and 1989 for the CERN LEP (Large Electron Positron collider) machine. The LEP tunnel lies between 45 m and 170 m below the surface, on a plane inclined at 1.4% sloping towards the Léman lake. The underground and surface structures at ATLAS and CMS are new, while those for ALICE and LHCb were originally built for LEP [12].

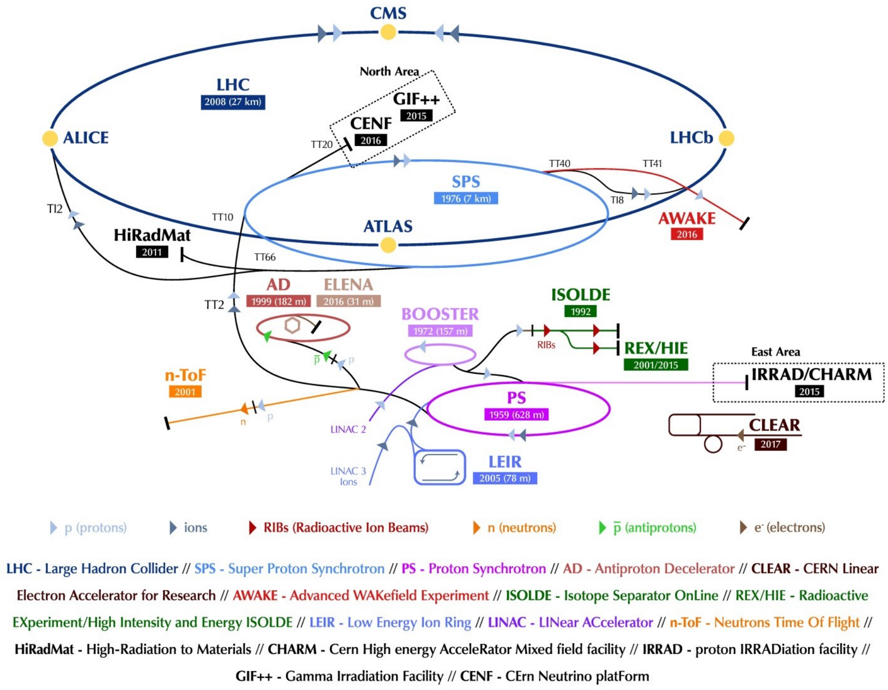

Figure 7: The CERN accelerator complex [13].

CERN accelerator system consists of different components. Linear accelerator 4 (Linac4) became the source of proton beams for the CERN accelerator complex in 2020. It accelerates negative hydrogen ions (H-, consisting of a hydrogen atom with an additional electron) to 160 MeV to prepare them to enter the Proton Synchrotron Booster (PSB). The ions are stripped of their two electrons during injection from Linac4 into the PSB, leaving only protons. These are accelerated to 2 GeV for the injection into the Proton Synchrotron (PS), which pushes the beam up to 26 GeV. Protons are then sent to the Super Proton Synchrotron (SPS), where they are accelerated up to 450 GeV (Figure 7).

The protons are finally transferred to the two beam pipes of the LHC. In one pipe the beam circulates clockwise while in the other circulates anticlockwise. It takes 4 minutes and 20 seconds to fill the LHC ring, and 20 minutes for the protons to reach their maximum energy of 6.8 TeV. Beams circulate for many hours inside the LHC beam pipes under normal operating conditions. The two beams are brought into collision inside four detectors – ALICE, ATLAS, CMS and LHCb – where the total energy at the collision point is equal to 13.6 TeV [14] [13].

2.1 CMS experiment

The Compact Muon Solenoid (CMS) experiment sits at one of the four collision points (Point 5), near Cessy (FR). It is a general-purpose detector, designed to observe any new physics phenomena that the LHC might reveal.

The Compact Muon Solenoid characteristics are its compactness, with its 15 meters high and 28.7 meters long, and dense structure (14000 tonnes). Moreover, it is devoted to detect particles as muons, using the high powerful solenoid which generates a magnetic field of 3.8 T. The solenoid is a cylindrical coil of superconducting fibres, cooled down to -268.5 °C, with an electrical current of 18.500 A used to generate the magnetic field, almost eliminating the electrical resistance.

CMS can detect up to 40 million particles collisions each second. Although most of the particles produced in the collisions are "unstable", they transform rapidly into stable particles that can be detected by CMS. By identifying almost all the stable particles produced in each collision, measuring their momenta and energies, and then piecing together the information of all these particles, the detector can recreate an "image" of the collision for further analysis.

The magnetic field deviates the charged particles generated during the high energy collisions in the LHC and, since a high particle momentum corresponds to a low path bending, a large magnetic field is desired to allow accurate measurement of the momentum of high energy particles. Indeed, the higher the magnetic field, the more effective is the path bending. However, bending particles with the magnetic field is not enough and a Silicon Tracker made of almost 75 million individual electronic sensors (pixels) arranged in concentric layers, is used to identify the path of the charged particles with high precision. As particles travel through the pixels and microstrips, they produce electric signals which are amplified and detected.

Finally, the energy of the charged particles produced in each collision is measured by two calorimeters: electromagnetic calorimeter (ECAL, measures the energy of electrons and photons, stopping them completely), and hadron calorimeter (HCAL, stops hadrons, which can go through the ECAL).

The final particle that CMS directly detects is the muon, a charged particle belonging to the same family of electrons and around 200 times heavier. However, muons are not stopped by the calorimeters, since they can penetrate several meters losing little energy; thus, sub-detectors must be used. The particle path is measured by tracking its position through the multiple active layers (four muon stations) which are located outside the magnetic coil and to increase the measuring precision, the acquired information is combined with the CMS silicon tracker measurements. Globally, there are 1400 muon chambers distributed over four layers: 250 drift tubes (DTs), 540 cathode strip chambers (CSCs), 610 resistive plate chambers (RPCs), and 72 gas electron multiplier chambers (GEMs) [15]. A CMS perspective view is shown in Figure 8.

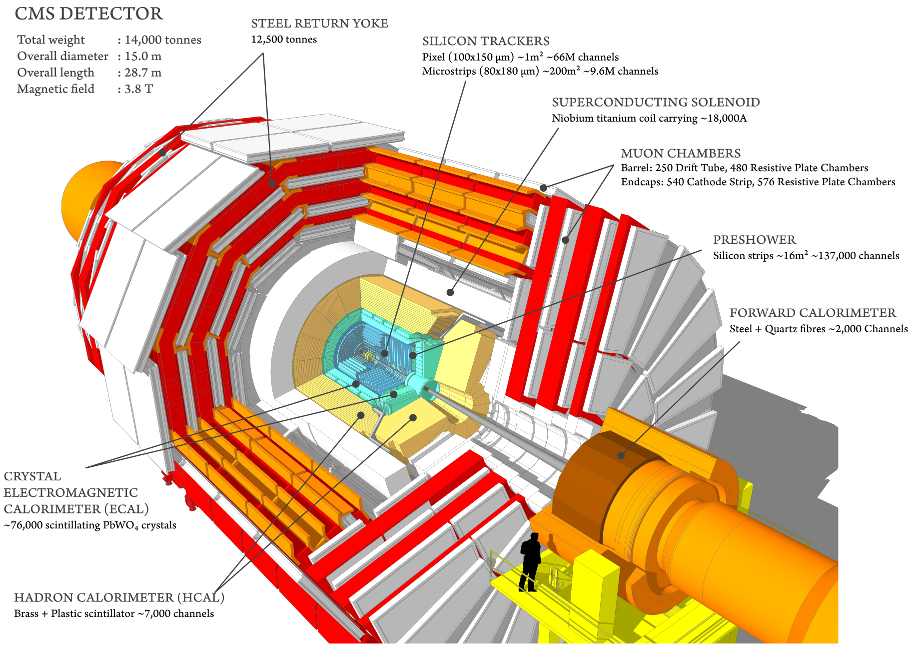

Figure 8: 3D view of the CMS detector [15].

2.1.1 The Resistive Plate Chambers

The Resistive Plate Chambers (RPCs) are fast gaseous detectors which provide a parallel trigger system to the DTs and CSCs. Combining good spatial and time resolutions, they are well suited for fast space-timing tracking as required for the muon trigger at the LHC [2].

The RPC consists of two parallel electrode plates, one positively charged (anode) and the other negatively charged (cathode), made by a high resistivity plastic phenolic resin (bakelite) and separated by a gas gap of few millimetres (2 mm) (Figure 9). The whole system is gas tight, with the two bakelite plates sealed by a polyvinyl chloride (PVC) [16]. An electric field is generated within the gas gap by coating the two bakelite plates with thin layers of conductive paintings, typically containing graphite, and connecting one to the HV (high voltage) and the other to the ground. The gap between the two electrodes is filled by a non-flammable mixture of $C_2H_2F_4/C_4H_{10}/SF_6$, 95.2/4.5/0.3 in relative proportion, operating in avalanche mode, with water vapour addition to keep the relative humidity at a value of around 45% [17]. Whenever a muon passes through the chamber, electrons are knocked out from the atoms of gas, hitting other atoms and causing an avalanche of electrons.

A well performant gas mixture must satisfy the following requirements [16]:

- High density of primary ion-electron clusters, to assure high detection efficiency
- Low photon emission/transmission to reduce photon feedback phenomena
- Being electronegative to reduce transversal side of the discharges and improve the localization
- Not dangerous for human health

- It should be characterised by negligible ozone depletion power (ODP) and low global warming potential (GWP)

Bakelite thickness	2 mm
Bakelite bulk resistivity	1-2·10^{10} Ω cm
Gap width	2 mm
Gas mixture	95.2% $C_2H_2F_4$, 4.5% C_4H_{10}, 0.3% SF_6
Operating high voltage	8.5 - 9.0 kV

Table 1: RPC basic construction and operating parameters [2].

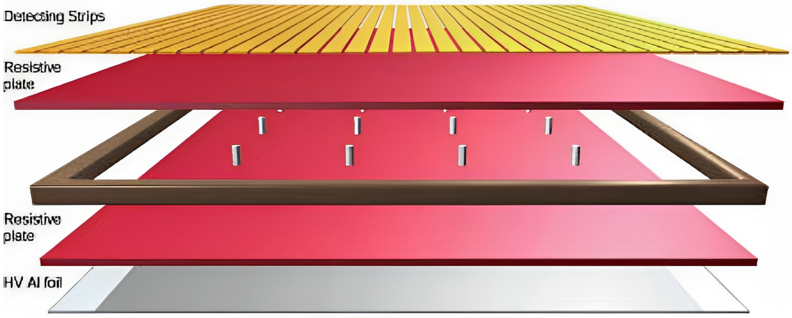

Figure 9: Resistive Plate Chamber exploded view. The two resistive plates (red), anode and cathode, are separated by a thin gas film sealed by polyvinyl chloride (light brown). The read-out is performed by means of aluminum strips (yellow), and the high voltage is applied on aluminum foil (grey) [2] [18].

3 RPC gas system

The main function of the gas system is to mix the three components, R134a, C_4H_{10}, and SF_6, with the corresponding percentages, 95.2%, 4.5%, and 0.3% respectively, and distribute the mixture through each chamber at a pressure between 1 and 3 mbar above the atmospheric pressure. Due to the large detector volume (18 m^3) and the expensive and pollutant gas mixture, a closed-loop circulation system was built and developed over three levels: the service gas room (SGX), the underground service room (USC), and the service cavern (UXC). The RPC gas system structure (Table 2) consists of the primary gas supply, the mixer, and the purifier in the surface gas room, the pre-distribution and circulation pumps in the underground service area, and the distribution system in the cavern (Figure 10). In addition, the new R134a recuperation plant was installed in the surface gas room.

Module	Situated in
Primary gas supply	*SGX Building*
Mixer	*SGX Building*
Chamber distribution system	*UXC55 Cavern*
Purifier and humidifier	*SGX Building*
Pump and return gas analysis	*USC55 Area*
R134a recovery system	*SGX Building*

Table 2: CMS Gas system structure for the RPCs. Number 55 refers to the CMS site [2].

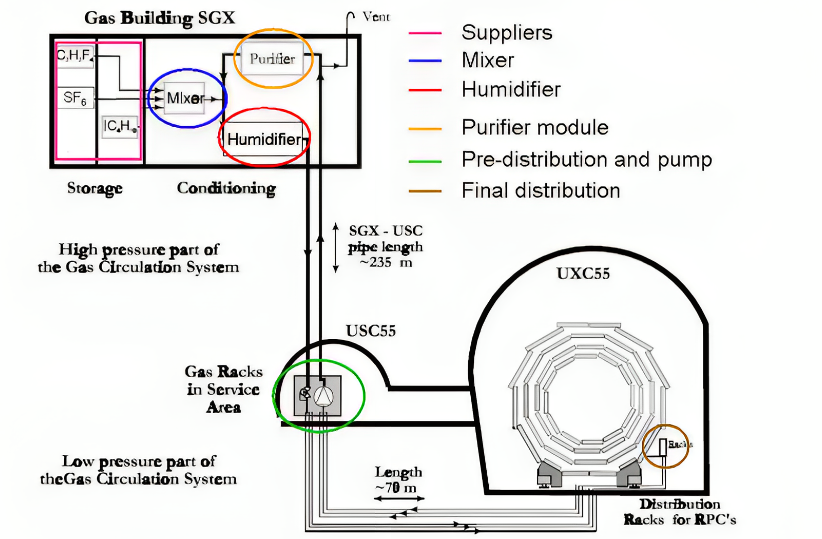

Figure 10: RPC gas system structure. The system develops over three levels, as listed in Table 2, with a closed loop distribution system [7].

3.1 Mixer

The mixer module has three input lines (Figure 11) and must provide the gas system and the particle detectors with the suitable gas mixture during the run phase. In addition, during specific phases it might also be needed to supply different gases (e.g., for purging the detector when the standard gas mixture needs to be evacuated, like at the beginning of a long shutdown period) or standard mixture at very high flow (e.g., when the detector is going to be restarted after a long shutdown, filling mode). The mixture injection is automatically tuned with mass flow controllers (with an absolute precision of 0.3% [2]) to guarantee the required replacement rate, to cope with detector's leak, or to compensate atmospheric pressure variations (in fact, a large fraction of detectors operate at constant relative pressure, therefore, the quantity of gas stored in the detector volume follows the atmospheric pressure changes) [7]. Moreover, the gas flow is stopped automatically if the C_4H_{10} concentration increases beyond the flammability limit [17] (at 20 °C and atmospheric pressure, the lower and upper flammable limits are 1.86% and 8.41% by volume of air, respectively [19]).

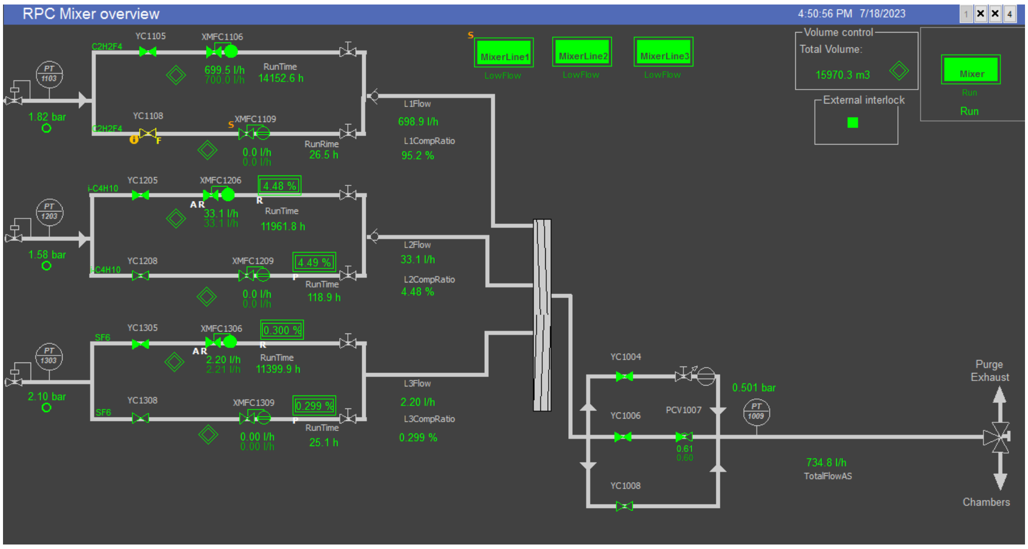

Figure 11: RPC gas mixer with the WinCC OA software layout. Starting from the top to the bottom input lines, the following gas are injected: R134a, isobutane, and SF_6.

3.2 Gas humidifier

RPCs are extremely sensitive to relative humidity, which influences the resistivity of the bakelite, with negative effects on the performances, due to the uncontrolled modification of the electric field inside the gas gaps. The desired relative humidity (RH) is typically 40% at the working temperature of the RPCs [20].

In the humidifier module (Figure 12), the gas is split in two flows to modulate the humidity: one gas line flows through a water volume, while the other is maintained dry. Downstream, the two lines are mixed together and a water content analyser measures the mixture humidity, using the measured value as a feedback signal for splitting the input flow into the wet and dry channels [21].

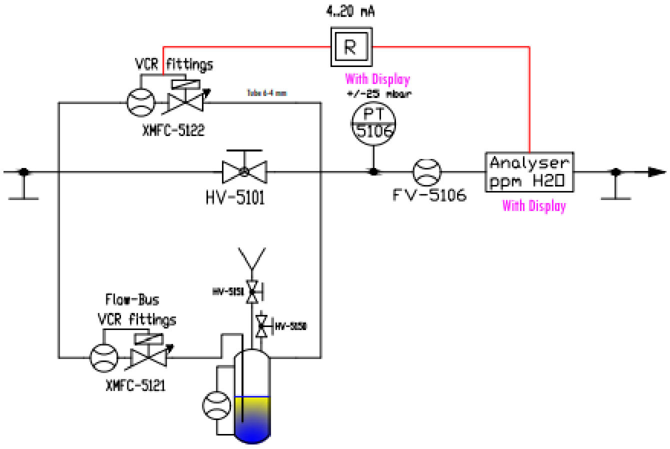

Figure 12: P&ID of the gas humidifier module [21].

3.3 Gas purifier

The impurities produced in the RPC chambers are high enough to influence the detector performances. Standard impurities that accumulate are O_2 and H_2O, while others might come from the breaking of the main gas mixture components under the combined action of electric field, charge multiplication and high radiation background. Therefore, to achieve a high recycling rate, the closed-loop circulation system is equipped with a purifier module.

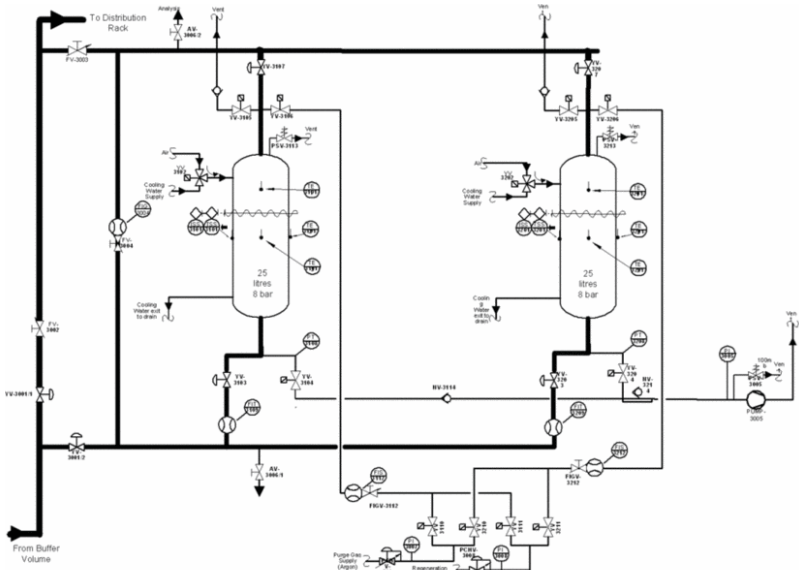

Figure 13: Typical purifier P&ID for a gas system [7].

The purifier unit (Figure 13) contains two cartridges of 24 liters, which are filled with the suitable purifier agent: in general, molecular sieves are used for water removal, metallic catalysts for oxygen absorption or other specific materials. During normal operation the gas mixture passes through one of the two columns, while the other is regenerated or it has just completed the regeneration cycle and it is ready to be used. In general, the regeneration procedures consist of vacuum and high temperature (about 200 °C) operations for molecular sieves, and high flows of Ar/H_2 mixtures at atmospheric pressure for metallic catalysts [7]. Concerning the RPC system, the main purity requirements are related to nitrogen ($< 1\%$) and oxygen ($< 1\%$). The amount of oxygen which must be removed depends on the leak rate of the chambers: the higher the rate, the higher the O_2 concentration injected from the external environment. On the other hand, nitrogen, as an inert gas, can be removed by a recuperation plant only, such as the R134a recovery system [2].

3.4 R134a recovery system prototypes

The current recovery system, installed in the CMS gas room, is the results of a previous prototype, which was firstly built at ATLAS experiment in December 2018 and then transferred at CMS in 2019. Since 2018, the old prototype has been tested in two configurations to find a simplified and optimized structure for the new recovery system.

3.4.1 Prototype - configuration I

The first prototype configuration under investigation is illustrated in Figure 14. The system consists in three main parts, which are represented by the three buffers: the vertical "cold" buffers, buffer1 and 2, and the horizontal "warm" buffer, buffer3. Each buffer has different heights, 20 cm for buffer1 and buffer3, and 10 cm for buffer2. A fourth, horizontal, buffer (Buffer 10 L) has the role of stabilizing the negative pressure before the compressor (-500 mbar).

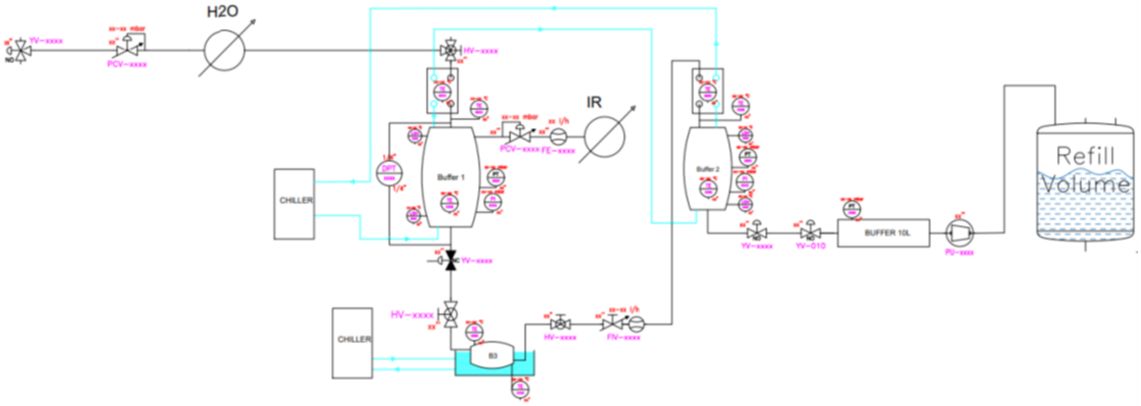

Figure 14: P&ID of the prototype first configuration [22], [23].

The system input mixture (95.2% R134a, 4.5% C_4H_{10}, and 0.3% SF_6 at 20 °C), coming from the purifier, passes through the Vaisala (for checking the H_2O concentration), before being liquefied in the first heat exchanger. Afterwards, the mixture starts filling buffer1, whose liquid level is controlled by a differential pressure transmitter. Comparing the boiling temperature of SF_6 (-67.6 °C at 1 bar [24]) with the buffer1 temperature (-35.5 °C), it is clear that SF_6 cannot condensate and leaves the system through the exhaust line. Moreover, a fraction of isobutane and R134a leaves the system in the form of azeotropic mixture, which represents the most volatile component, since its boiling point is lower than the pure R134a (-32.3 °C and -26.4 °C respectively, at 1 bar [25]). Then, the liquefied mixture flows down to buffer3, whose temperature is above 0 °C, and evaporates. The vapour phase is liquefied in the second heat exchanger, fills buffer2, whose temperature is higher than buffer1, and the remaining volatile components are removed. Finally, the pumping unit extracts the recovered mixture compressing it in the refill volume [23].

3.4.2 Prototype - configuration II

The second prototype configuration is shown in Figure 15. The main difference with the first is the elimination of the second heat exchanger and buffer2, in which the second liquefaction occurred. The working principle are the same as described in chapter 3.4.1 with the advantage that the modification avoids further phase change, reducing the energy demand for the liquefaction process and allows to work in continuous mode with variable flowrates [22].
The transition between prototypes configurations I and II was carried out after seeing that the presence of buffer2 did not influence the recovered gas quality. Indeed, comparing the gas analyses before and after disabling buffer2, similar results in terms of isobutane concentration were obtained, as shown in Figure 16.

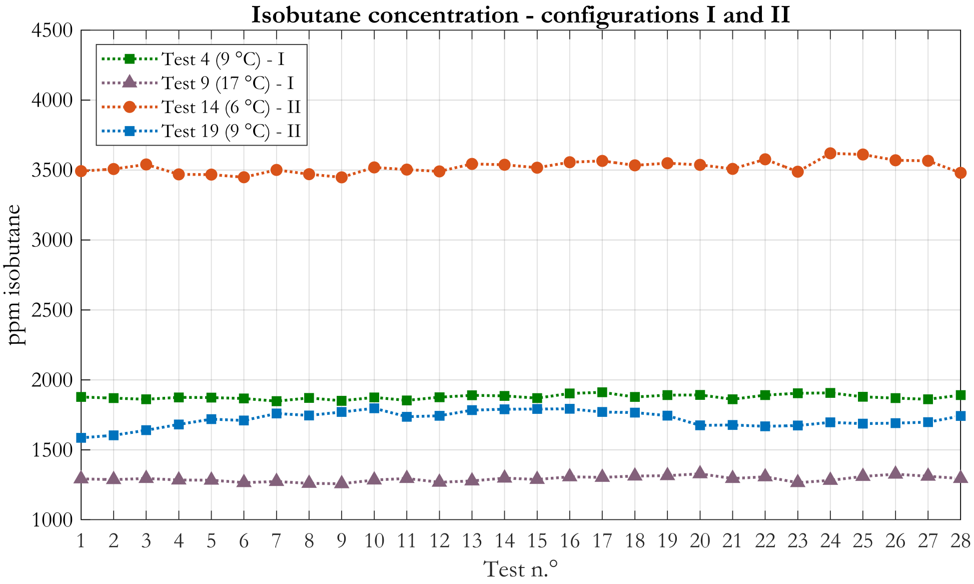

Figure 15: Isobutane concentration vs corresponding analysis number. Comparison between first (I) and second (II) prototype configurations. At 9 °C both configurations show a similar isobutane concentration (Tests 9 and 19), meaning that the prototype simplification did not influence the recovered gas quality [22].

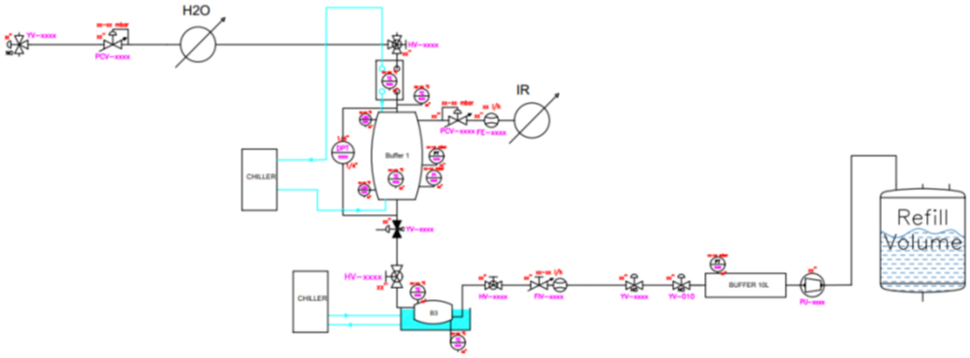

Figure 16: P&ID of the prototype second configuration [22], [23].

3.5 New R134a recovery system

The new recovery system was installed in the surface gas room and consists in four main units: the electric rack, the distillation unit, the pumping, and the storage units. The system P&ID is reported in Appendix A.

3.5.1 Electric rack

The electric rack (Figure 17) hosts, in an ATEX environment, all the electrical and electronic components for the system automation through the PLC (Programmable Logic Controller). Indeed, it can be monitored remotely using the WinCC Open Architecture, the Supervisory Control and Data Acquisition (SCADA) and Human-Machine Interface (HMI) system from Siemens [26] (Appendix B). The electric rack also contains the mass flow controller for regulating the input mixture flowrate and the Vaisala Dewpoint Transmitter to measure the dew point and avoid the presence of water in input, which would be dangerous for the system (generally the dew point temperature should not be higher than -40 °C). In addition, a three-way valve is installed upstream the Vaisala to shift the input flow from the mixture to the nitrogen line, which can be used, for instance, for the system purge.

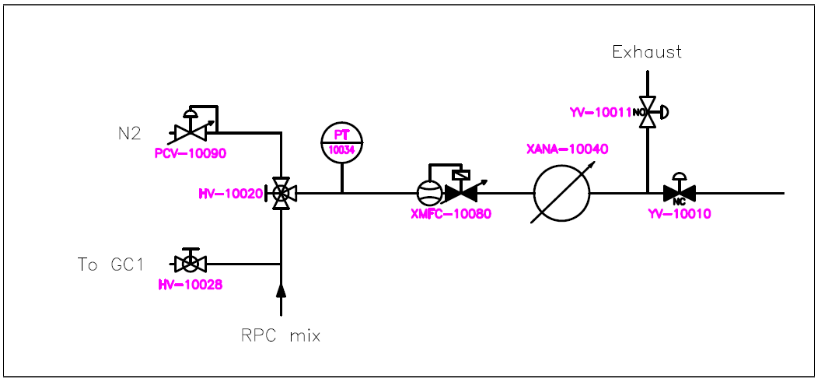

Figure 17: Electric rack P&ID.

Component	**Index**
N_2 pressure control valve	*PCV-10090*
Input mixture analysis valve	*HV-10028*
Three-way valve	*HV-10020*
Mass flow controller	*XMFC-10080*
Vaisala Dewpoint Transmitter	*XANA-10040*
Normally open pneumatic valve (exhaust)	*YV-10011*
Normally closed pneumatic valve (mixture)	*YV-10010*

Table 3: Electric rack. Components with the corresponding P&ID index.

3.5.2 Distillation unit

The distillation unit consists of two racks, closed in an ATEX environment, each one containing two columns for the separation process of the input mixture. Each column develops vertically with two buffers: the top and the bottom buffers. In addition, two refrigeration units are connected to the system: the LAUDA Integral XT 280 sets the temperature of the top buffer cooling circuit, while the Huber Ministat 125 controls the temperature of the bottom buffers circuit. Depending on the column, buffers have different dimensions. In particular, columns 1 and 2 have top buffers of 30 cm height and bottom buffers of 10 cm height. On the contrary, columns 3 and 4 have top and bottom buffers of 20 cm height. The internal and external diameters are the same for all buffers (designed as coaxial cylinders), 114.3 mm and 139.7 mm respectively (see Appendix C).

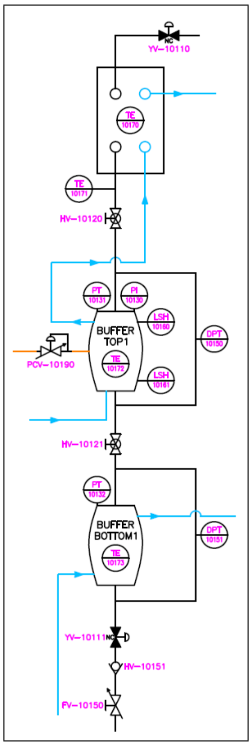

Figure 18: Column 1 P&ID. All columns have the same structure since they are designed in parallel.

The system works with four columns (Figure 18) in parallel, and each one is filled individually. During the filling phase the gas mixture is liquefied in the flat plate counter-current heat exchanger, before flowing in the top buffer where the separation process occurs. All the top buffers should be cooled down at a temperature ranging between the azeotropic and the R134a boiling temperatures, which are -32.3 °C and -26.4 °C, at 1 bar, respectively, in order to allow the distillation. Considering the SF_6 boiling point (-67.6 °C at 1 bar) and the Lauda setpoint temperature (between -36.5 °C and -36 °C), it is clear that it never liquefies and leaves the system through the exhaust line after exiting the heat exchanger. The filling phase ends whenever the top liquid sensor (LSH-10x60) turns on, and the liquid level is constantly monitored through the differential pressure transmitters (DPT-10x50). Moreover, the top buffer pressure can be regulated by the Zimmerli control valves (PCV-10x90), and represents a crucial parameter for the system performances (in particular for the system efficiency).

The liquid mixture flows down in a 10 mm tube, due to gravity, from the top to the bottom buffer which is maintained warm at a temperature between 14 °C and 23 °C (according to the fixed testing conditions). Due to the high temperature, compared to the boiling points, the mixture evaporates, almost instantaneously and, thanks to the buoyancy force, the vapour phase goes up and condensates in the top buffer. The release of the condensation heat determines a gradual temperature increase (ideally with infinitesimal steps), forcing the more volatile component (azeotropic mixture) to evaporate and flow out at the exhaust line.

As soon as the filling phase finishes, the emptying phase starts, after the opening of the pneumatic valve YV-10x11. The recovered mixture flows through a non-return and a needle valve to avoid backflows issues and to regulate the emptying flowrate.

Component	**Index**
Normally close pneumatic valve (column input)	*YV-10x10*
Normally close pneumatic valve (column output)	*YV-10x11*
Temperature sensor on the heat exchanger	*TE-10x70*
Temperature sensor at the heat exchanger output	*TE-10x71*
Temperature sensor on the top buffer	*TE-10x72*
Temperature sensor on the bottom buffer	*TE-10x73*
Pressure transmitter on the top buffer	*PT-10x31*
Pressure transmitter on the bottom buffer	*PT-10x32*
Pressure indicator on the top buffer	*PI-10x30*
Lower liquid level sensor	*LSH-10x61*
Upper liquid level sensor	*LSH-10x60*
Top buffer differential pressure transmitter (for monitoring liquid level)	*DPT-10x50*
Bottom buffer differential pressure transmitter (for monitoring liquid level)	*DPT-10x51*
Zimmerli at the exhaust line	*PCV-10x90*
Manual valve connecting top and bottom buffers	*HV-10x21*
Non-return valve (to avoid backflows)	*HV-10x51*
Needle valve (to regulate emptying flowrate)	*FV-10x50*

Table 4: Column 1. Components with the corresponding P&ID index.

3.5.3 Pumping and storage units

During the emptying phase, the compressor is activated to pump the recuperated mixture from the distillation to the storage unit. More than one column can be emptied simultaneously and the total extraction flowrate is controlled by a rotameter, downstream the two racks. The pumping unit (Figure 19) consists of the 7LG-TS-7 two-stage gas booster, whose main application is transferring and extracting liquefied gases such as R134a from their liquid or vapor phase with moderate vacuum at inlet [27]. In order to maintain the moderate vacuum at inlet, a 10 L buffer volume is provided upstream the compressor, and the air driving pressure is modulated to keep the buffer at a consntant value of -300 mbar.

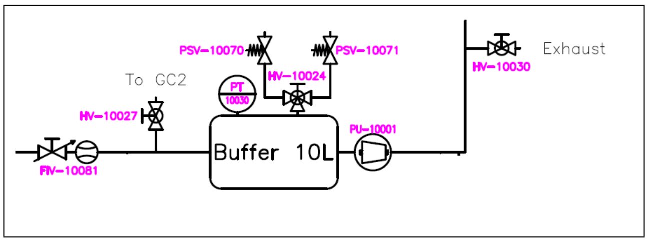

Figure 19: Pumping unit P&ID.

The storage unit (Figure 20) is a stainless-steel cylindrical tank with a capacity of 400 kg. To avoid liquid formation in the drum, pressure must not overcome the R134a saturation point (5.7 bara at 20 °C [24]). Finally, from the storage unit output, a selected flowrate of recovered gas is injected in the RPC mixer at a pressure of 1.8/2.0 barg.

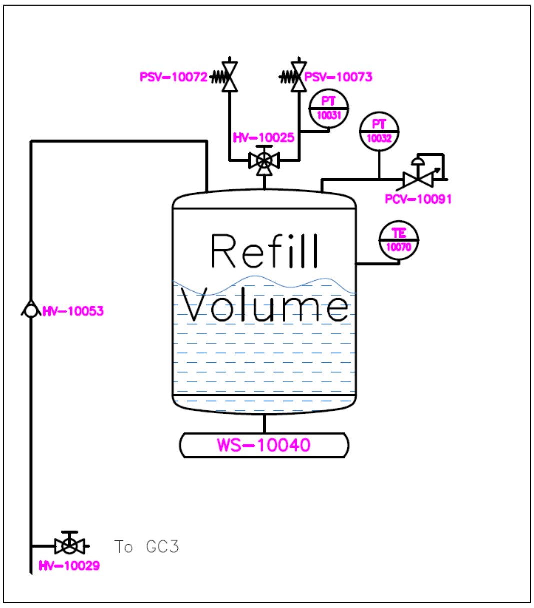

Figure 20: Storage unit P&ID.

Component	**Index**
Rotameter (column output)	*FIV-10081*
Manual valve (before pump GC analysis)	*HV-10027*
Manual valve (exhaust line after pump)	*HV-10030*
Manual valve (after pump GC analysis)	*HV-10029*
Pressure transmitter (Buffer 10 L)	*PT-10030*
Pressure transmitter (inside storage tank)	*PT-10031*
Pressure transmitter (output storage tank)	*PT-10032*
Pressure safety valves (Buffer 10 L)	*PSV-10070(1)*
Pressure safety valves (Storage tank)	*PSV-10072(3)*
Air driven gas booster	*PU-10001*
Non-return valve (avoid backflow to the compressor)	*HV-10053*
Pressure control valve (Tescom, storage tank output)	*PCV-10091*
Temperature sensor (monitoring the storage tank heating)	*TE-10070*
Weight scale	*TE-10040*

Table 5: Pumping and storage units. Components with the corresponding P&ID index.

4 Distillation overview

Distillation is a method of separating the components of a solution, which depends on the distribution of the substances between a liquid and a gaseous phase, applied in cases in which both components are present in both phases. Therefore, distillation is concerned with the separation of solution where all components have appreciable volatility [28].

4.1 Vapor-liquid equilibria

The actual mixture consists of three components, however, sulphur hexafluoride, at the operating temperatures (around -36 °C), never liquefies (its boiling temperature at 1 bar is -67.6 °C) and the remaining mixture is essentially composed of R134a and C_4H_{10}. Therefore, these two components form the binary mixture (or ordinary mixture) which represents the core part of the separation process.

4.1.1 Constant pressure equilibria

In a constant pressure equilibrium diagram (Figure 21), the upper curve (*dew curve*) represents the temperature-vapor composition relationship (T vs y^*), while the bottom curve (*bubble curve*) represents the temperature-liquid composition relationship (T vs x). In case of a binary mixture, it is not possible to consider a single boiling point since vaporization occurs over a temperature range (e.g., temperature range between H and M). The more the mixture vaporizes, the larger the amount of vapor is formed with respect to liquid, which can be quantified with Equation 1.

$$\frac{molD(liquid)}{molF(vapor)} = \frac{lineEF}{lineDE} \tag{1}$$

The vapor-liquid equilibrium composition can be displayed also on a distribution diagram, x vs y*, where x represents the molar fraction of the component A in the liquid, and y* the molar fraction of component A in the vapor phase (with A as a generic component) (Figure 22). The larger the distance between the equilibrium curve and the diagonal, the greater the difference in liquid and vapor compositions, and the easier is the distillation process [28].
The ease of distillation is quantified by the relative volatility α:

$$\alpha = \frac{y^*(1-x)}{x(1-y^*)} \tag{2}$$

The higher is the value of α above the unity, the easy is the distillation, while for $\alpha = 1$ no separation is possible.

4.1.2 Constant temperature equilibria

Similar to the constant pressure equilibrium diagram, a constant temperature equilibrium diagram is obtained at constant temperature, and the two curves extend from the vapor pressure of pure B to the vapor pressure of pure A (Figure 23).

A solution, in a closed container, at point W is entirely liquid, and reducing the pressure at constant temperature, the first bubble of vapor forms, at U, and complete vaporization occurs at S. Further pressure reduction generates superheated vapor in point R [28].

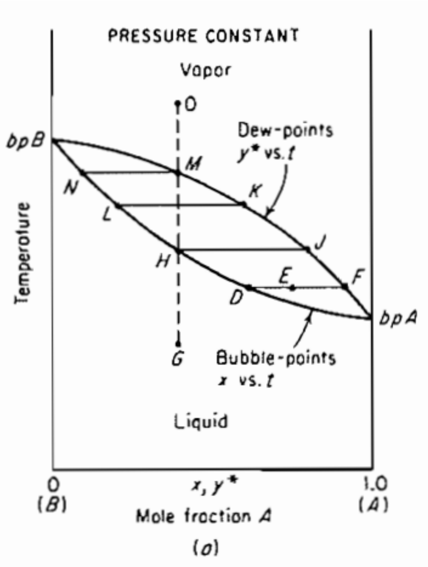

Figure 21: Vapour-liquid equilibrium diagram at constant pressure for a generic binary mixture of components A and B, with boiling points *bpA* and *bpB* respectively. The phase change between liquid and vapor occurs within a temperature range whose values depend on the mixture composition (mole fraction of A and B) [28].

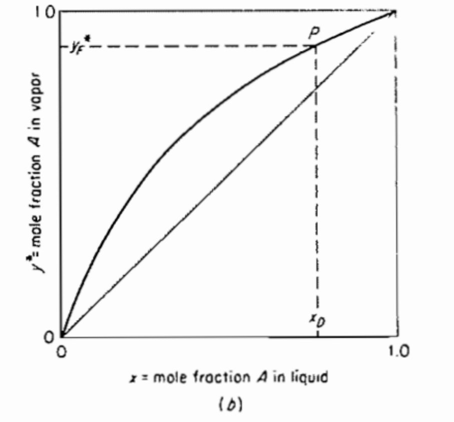

Figure 22: Vapor-liquid equilibrium distribution diagram. The equilibrium curve lies above the 45° line, meaning that the vapor is richer than liquid in the substance A. Point P represents the tie line DF in Figure 21 [28].

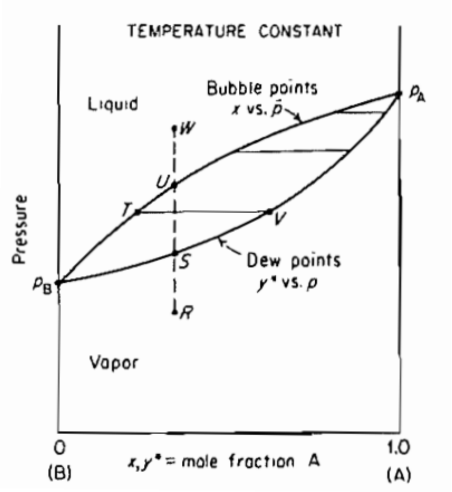

Figure 23: Vapour-liquid equilibrium diagram at constant temperature for a generic binary mixture of components A and B, with vapor pressures p_A and p_B respectively [28].

4.2 Raoult's law

Raoult's law is applicable only for mixture whose vapor and liquid phases are ideal. For an ideal solution, at a fixed temperature, the partial pressure p^* of a pure component is equal to the vapor pressure of the pure component (at the fixed temperature) multiplied by its molar fraction in the liquid [28].
Equations 3 and 4 define the partial pressures for component A and B respectively.

$$p_A^* = p_A x \tag{3}$$

$$p_B^* = p_B(1 - x) \tag{4}$$

Finally, combining Raoult's and Dalton's law, the total vapour pressure p_T of the binary mixture is obtained.

$$p_T = p_A^* + p_B^* = p_A x + p_B(1 - x) \tag{5}$$

4.3 Positive deviation from ideality and minimum boiling azeotrope

A positive deviation from ideality is reached when the total pressure of the mixture is higher than the one computed in an ideal condition with Raoult's law, with the partial pressure of each component grater than ideal.
When the deviation from ideality is large and the vapor pressures of the components are not significantly different, the total pressure curve at constant temperature (Figure 24a) may rise to form a peak or decrease to form a minimum (Figure 24b) in a constant pressure equilibrium diagram, at a specific concentration (concentration L in Figure 24b). This behaviour is typical of *azeotropic* (or *constant boiling*) *mixtures.* Binary mixtures with composition lower than L (left side of the diagram) are characterized by a vapor phase richer in the most volatile component than the liquid phase, while all mixtures with compositions higher than L (right side of the diagram) show

a vapor phase leaner in the most volatile component than the liquid phase.
Considering two solutions at concentrations D and H, boiling them in an open vessel, and letting the vapor phase to be released, the residual liquids, in both cases will move along the bubble curve away from the point L (D towards J and H towards K). However, an azeotropic solution cannot be completely separated by normal distillation since vapor and liquid phases have the same composition ($x = y^*$) and the phase change (liquid-vapor) occurs at constant temperature. Moreover, since the relative volatility α is unitary, a "classical" separation is not possible.
Azeotropic composition and boiling temperature change with pressure (see Table 7) and at a sufficient low pressure, the azeotropism disappears. In the case study under investigation, R134a and C_4H_{10} form a minimum boiling azeotrope.

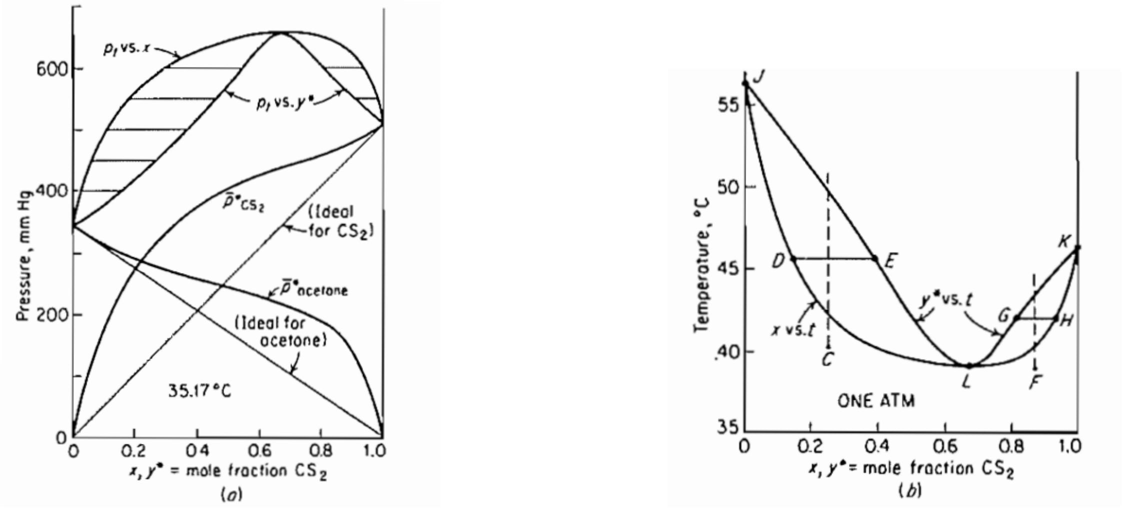

(a) Constant temperature equilibrium diagram with minimum boiling azeotrope [28].

(b) Constant pressure equilibrium diagram with minimum boiling azeotrope [28].

Figure 24: Minimum boiling azeotrope.

The existence of an azeotrope introduces limits on the capability to separate components through distillation, called distillation boundaries. Different feed stream compositions may lead to different products. In particular, if no azeotrope is present, the VLE (vapor liquid equilibrium) curve lies entirely above the 45° line in the x vs y^* diagram.
On the other hand, in presence of a minimum boiling azeotrope there is a distillation boundary at the azeotropic composition. If the feed is lower than the azeotropic composition (Figure 25a), the bottom product will be the heavy key component while the distillate will be slightly lower than the azeotrope. On the contrary, if the feed is higher than the azeotrope composition (Figure 25b), the bottom product will be the light key component and the distillate will be slightly higher than the azeotrope [29].

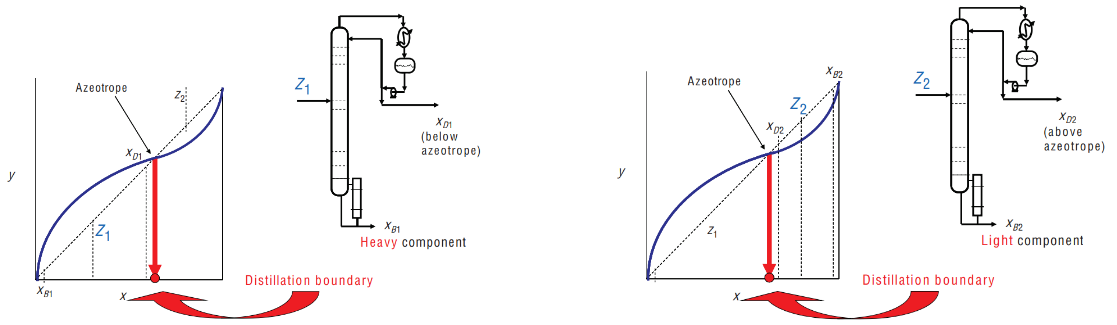

(a) x vs y diagram. Feed concentration lower than the azeotropic concentration.

(b) x vs y diagram. Feed concentration lower than the azeotropic concentration.

Figure 25: Effect of the azeotrope as distillation boundary [29].

4.4 Flash vaporization and differential distillation

Flash vaporization (or equilibrium distillation) process is a single step separation process where the liquid mixture is partially vaporized (Figure 26). During the distillation, vapor is enriched in the more volatile (*light key*) component, while the remaining liquid is rich in the less volatile component (*heavy key*).
The process is called "flash" since the vaporization is extremely rapid and it may be in batchwise or in continuous mode [28][30].

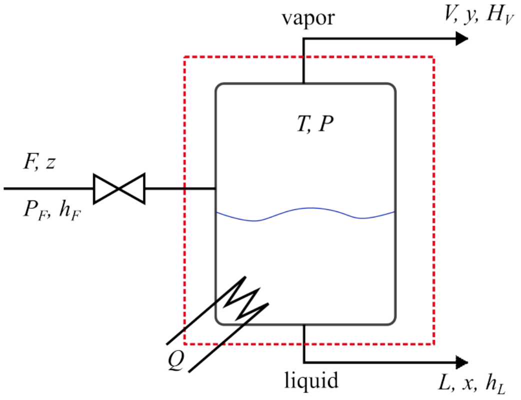

Figure 26: Flash distillation unit scheme with feed line (F), vapor (V) and liquid (L) outputs, and heating unit (Q) [30].

A flash distillation process can be represented on a T-xy diagram as shown in Figure 27. The feed, at temperature T_F and composition z enters the flash unit and increases its temperature to the setpoint value T. At this point the feed mixture is no more in equilibrium, and it is split in a vapor phase (rich in the more volatile component), with composition y and a liquid phase, with composition x [30].

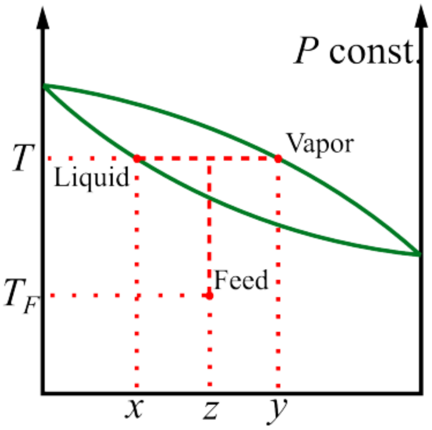

Figure 27: T-xy equilibrium diagram for a flash distillation process [30]

At the equilibrium, a set of three equations defines the mass and energy balance [30].

$$F = L + V \tag{6}$$

$$Fz = Lx + Vy \tag{7}$$

$$Fh_F + Q = Lh_L + Vh_V \tag{8}$$

Where F, L, and V are the feed, liquid, and vapor flowrates respectively. x, y, z are the liquid, vapor, and feed compositions (in the more volatile component) respectively. h_F, h_L, and h_V are the feed, liquid, and vapor enthalpies, and Q the heat provided to the flash unit.

More than one flash vaporization unit can be series connected to improve the separation process with respect to the single flash operation. By reducing the amount of vapor formed in each stage and increasing the total number of vaporization flashes (n), the process tends to a **differential** (or simple) **distillation** (Figure 28).

The mixture is boiled slowly to allow the vapor be in equilibrium with the liquid at each flash stage. Then, the vapor is sent to a condenser, as soon as it is formed, and liquefied to form the distillate. Moreover, the first portion of the distillate is rich in the most volatile components and during the distillation process the vapor product becomes leaner. Considering for instance a ternary mixture (A, B, C components with decreasing volatility), the first component to be vaporized will be the most volatile one (component A) while, as the distillation proceeds, the components with intermediate volatilities (B and C) will be vaporized.

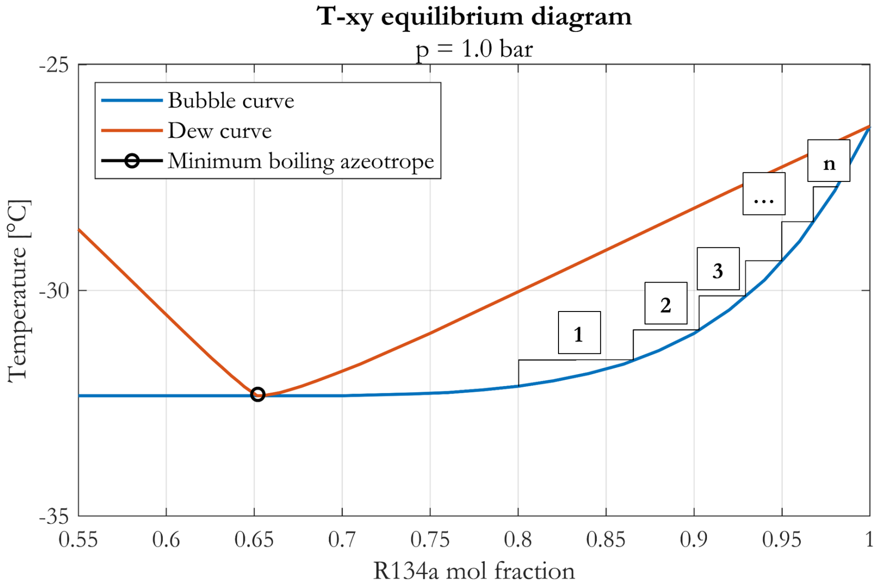

Figure 28: Constant pressure (1.0 bar) equilibrium diagram for multistage flash distillation. At each step the temperature increases, and the distilled mixture undergoes a new flash distillation. Ideally increasing the number of units (n) to infinite, a **differental distillation** is obtained.

5 Mixture characterization

The new recovery system operates with a mixture at the composition illustrated in Table 6.

Component	**Molar fraction**	**Mass fraction**
R134a	95.2%	96.9%
C_4H_{10}	4.5%	2.6%
SF_6	0.3%	0.5%

Table 6: RPCs gas mixture composition.

Each component has its own boiling temperature, whose values depend on the mixture pressure. Moreover, R134a and C_4H_{10} form an azeotrope, whose composition also depends on the mixture pressure, and which cannot be separated by standard distillation. Therefore, a distillation process should be carried out to separate the pure R134a with respect to the azeotrope and SF_6.

Temperature and pressure dependences of the azeotropic mixture have been simulated by using AspenPlus® simulation software [25]. Considering that the RPC mixture has a maximum pressure of 1.6 bara (600 mbarg), seven pressure levels were analysed from 1.0 bara to 1.6 bara. The simulation was performed exploiting the REFPROP (Reference Fluid Thermodynamic and Transport Properties Database) property method developed by the National Institute of Science and Technology (NIST). Depending on the mixture pressure, both composition and boiling temperature of the azeotrope change. In particular, the boiling temperature increases, while the composition is enriched in R134a, as pressure increases (Table 7). The equilibrium diagrams are available in Appendix D.

Pressure [bara]	**Boiling temperature [°C]**	**R134a**	**Isobutane**
1.0	-32.3	0.652	0.348
1.1	-30.2	0.655	0.345
1.2	-28.2	0.657	0.343
1.3	-26.4	0.659	0.341
1.4	-24.6	0.661	0.339
1.5	-22.9	0.663	0.337
1.6	-21.4	0.664	0.336

Table 7: Azeotropic boiling temperature and composition against pressure.

In addition, boiling temperatures of pure components increases with pressure, as reported in Table 8.

Pressure [bara]	T_{boil}^{R134a} **[°C]**	T_{boil}^{C4H10} **[°C]**	T_{boil}^{SF6} **[°C]**
1.0	-26.4	-12.1	-67.6
1.1	-24.3	-9.6	-65.8
1.2	-22.3	-7.3	-64.0
1.3	-20.5	-5.2	-62.4
1.4	-18.8	-3.2	-60.8
1.5	-17.1	-1.3	-59.4
1.6	-15.6	0.5	-58.0

Table 8: Boiling temperatures of R134a, C_4H_{10}, and SF_6 at different pressures.

Considering Table 8, at each pressure level the light key component is the sulphur hexafluoride, the heavy key is the isobutane, while R134a is in between the two. However, if only R134a and C_4H_{10} are considered, since they form a minimum boiling azeotrope, the light key component will be represented by the azeotrope itself (whose composition varies according to Table 7), while the heavy key[1] will be the R134a.

---

[1] The most volatile component is called the light key and the least volatile is called the heavy key. They are defined by their molecular weight and boiling points. The light key, by definition has a lower boiling point than the heavy key [31][32].

6 Gas chromatograph

The gas analyses were performed by using a gas chromatograph and considering five sampling points: input gas mixture, before and after compressor, storage tank and exhaust line.

Gas chromatography includes a group of analytical separation techniques to analyse volatile substances in the gas phase. The components of a sample are dissolved in a solvent and vaporized in order to separate the analytes through their interaction with a stationary phase. In a gas-solid chromatography (GSC) the stationary phase is a solid adsorbant, while in a gas-liquid chromatography (GLC) it is a liquid on an inert support [33]. In addition, carrier gases are required to move the sample through the GC, allowing the interaction with the stationary phase. Carrier gases must be chemical inert, such as nitrogen, helium, argon, and carbon dioxide.

The temperature of the sample port is usually 50 °C higher than the boiling point of the least volatile component. The sample injection should not be too large to avoid losing resolution and depends on the type of column: for packed columns it ranges between tenths of microliters to 20 microliters, while for capillary columns, which require less sample, it is commonly around a microliter. The components are detected by a thermal conductivity detector (TCD) and the output of the GC is a gas chromatogram, displayed as μV versus time. The different components are identified by their retention time, which is the time taken by the solute to pass through a chromatography column, depending on the interaction with the coating material and the time at which the peak appears in the chromatogram.

A generic functioning scheme and GC structure are reported in Figure 30 and Figure 29.

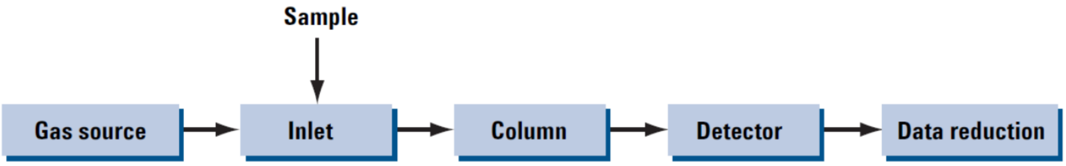

Figure 29: Functioning chart of the gas chromatograph. The gas source represents the carrier (Ar/He), which transports the sample through the column. The components are detected by the TCD and data are displayed on the chromatogram [34].

The GC used for the analyses is equipped with two analytical columns: PPU (Porous Layer Open Tubular, Figure 32) and MS (Molecular Sieve, Figure 33) 5 Å, which can separate heavy hydrocarbons (from C_4 to C_{12}), light hydrocarbons (from C_1 to C_4) plus H_2O, CO_2, CH_4, and light components plus noble gases respectively [35].

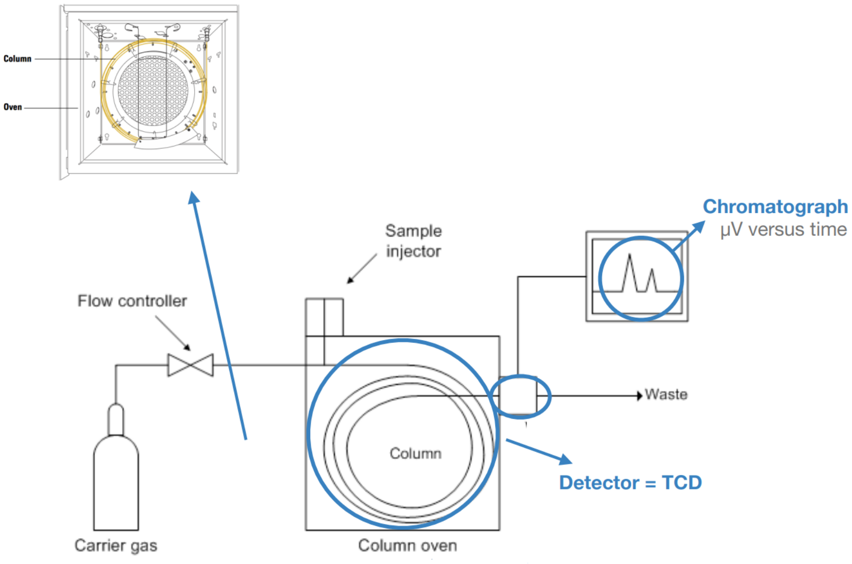

Figure 30: Scheme of the gas chromatogram. The carriers (Argon and Helium) are injected in the system and regulated by a mass flow controller; the sample, also regulated by a flow controller, is transported by the carriers, from the injector to the detector, through the columns heated in the oven at a temperature at least 50°C higher than the boiling point of the less volatile component (the detailed temperatures are shown in the GC method in Figure 31)). After the TCD, the sample is exhausted through a waste line [34].

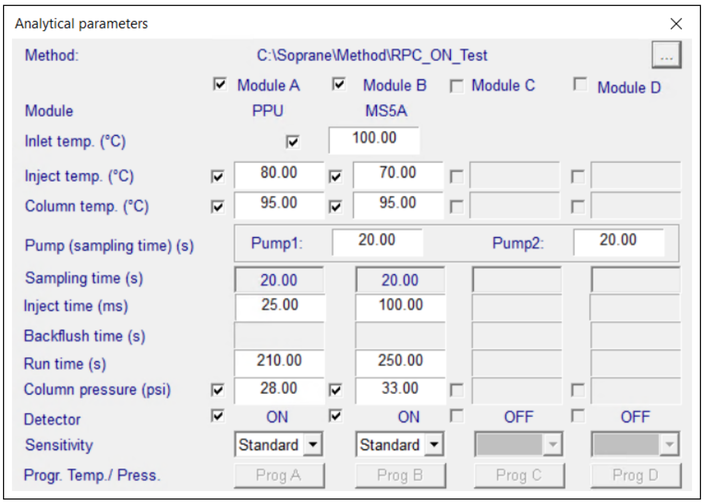
Analytical parameters

Method: C:\Soprane\Method\RPC_ON_Test

	☑ Module A	☑ Module B	☐ Module C	☐ Module D
Module	PPU	MS5A		
Inlet temp. (°C)	☑ 100.00			
Inject temp. (°C)	☑ 80.00	☑ 70.00	☐	☐
Column temp. (°C)	☑ 95.00	☑ 95.00	☐	☐
Pump (sampling time) (s)	Pump1: 20.00		Pump2: 20.00	
Sampling time (s)	20.00	20.00		
Inject time (ms)	25.00	100.00		
Backflush time (s)				
Run time (s)	210.00	250.00		
Column pressure (psi)	☑ 28.00	☑ 33.00	☐	☐
Detector	☑ ON	☑ ON	☐ OFF	☐ OFF
Sensitivity	Standard	Standard		
Progr. Temp./ Press.	Prog A	Prog B	Prog C	Prog D

Figure 31: GC method (*RPC-ON-Test*) for the analyses, with the corresponding analytical parameters. Each module is characterised by injecting and column temperatures, injection, sampling, run time, and pressure.

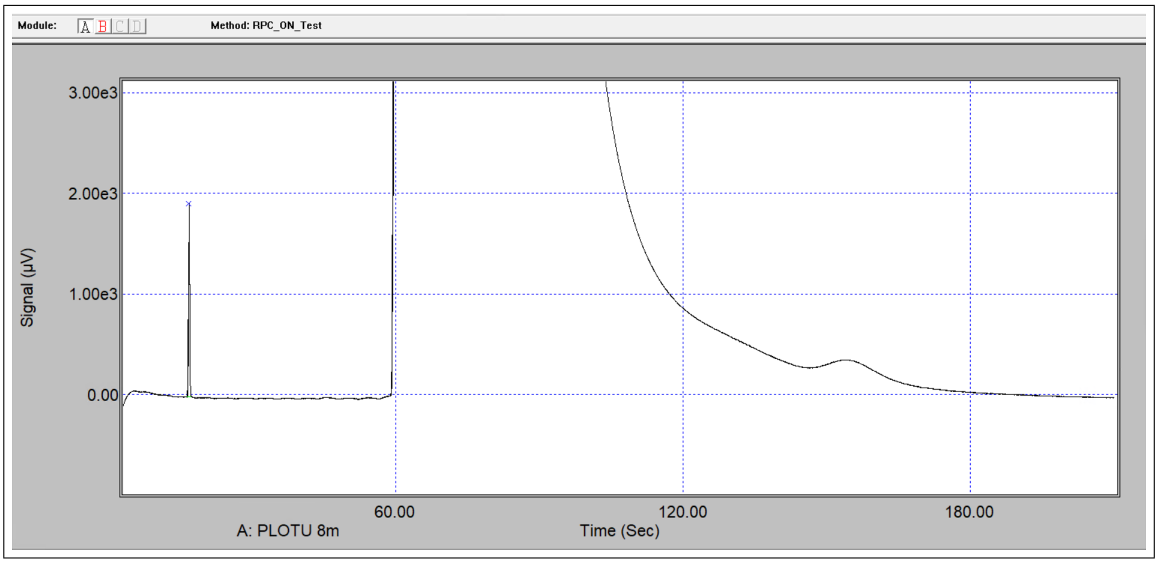

Figure 32: PPU chromatogram (after pump analysis) zoomed view. From left to right: air, R134a, and R134a isomer peaks are displayed.

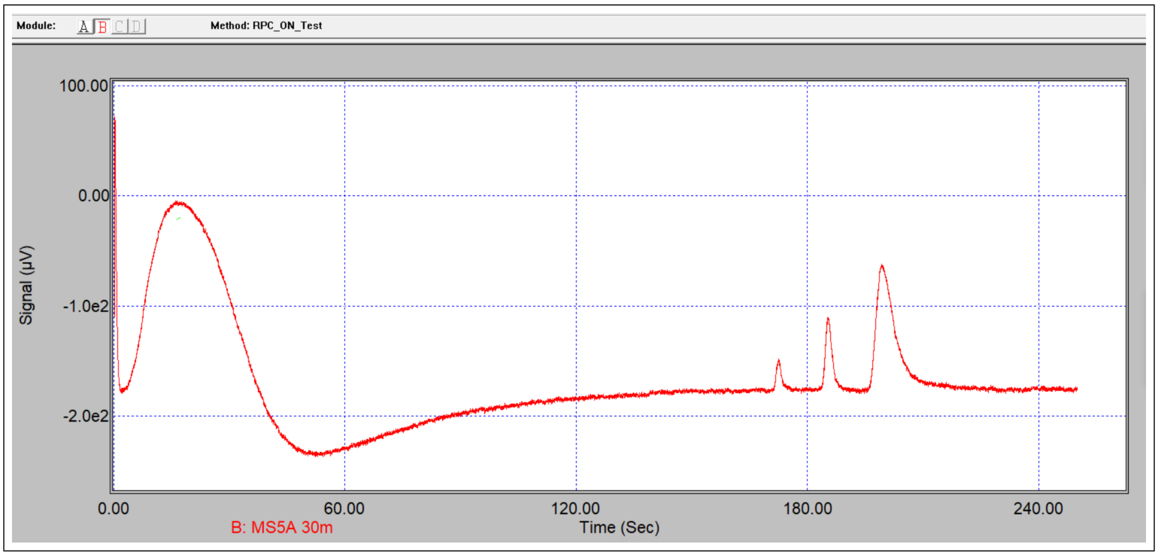

Figure 33: MS chromatogram (after pump analysis). From left to right: oxygen, nitrogen, and isobutane peaks are displayed.

6.1 GC calibration

In order to have accurate results, the gas chromatograph must be calibrated before starting the analyses. It is necessary to define the calibration factors and to extrapolate a calibration curve.
Four known isobutane concentrations were used to find the corresponding calibration factors: 0.5%, 1%, 2%, and 4.5%. By doing the analyses and integrating the areas of the gas chromatogram, the calibration factors (CF) were obtained, dividing the concentration by the area (Equation 9). Considering that, during the tests, the isobutane concentrations were derived from the Molecular Sieve, it follows that the relevant calibration factors (Table 9) and calibration curve (Figure 34) were calculated for the MS. Finally, the nitrogen and oxygen calibration factors, evaluated with known concentrations of 1000 ppm and 100 ppm respectively, are 1.730 ppm/μV and 1.295 ppm/μV respectively.

$$CF = \frac{concentration[ppm]}{area[\mu V]} \tag{9}$$

% C_4H_{10}	**Calibration factor [ppm/μV]**
0.5	1.341
1.0	1.388
2.0	1.457
4.5	1.520

Table 9: Calibration factors for the C_4H_{10} in the Molecular Sieve.

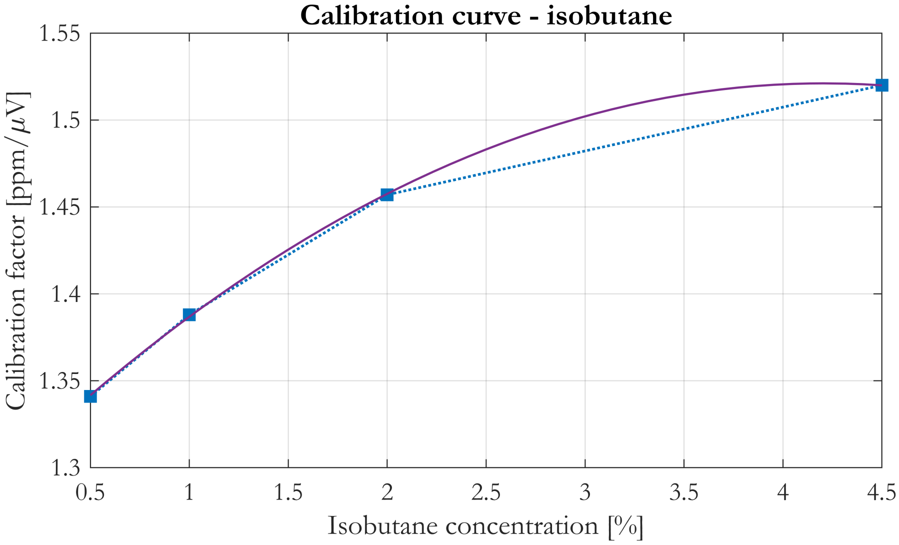

Figure 34: Calibration curve for the C_4H_{10} in the Molecular Sieve. The obtained calibration factors (blue squared points) show a quadratic trend (purple line) with the isobutane concentration.

7 Thermodynamic and process simulations

Thermodynamic and chemical process simulations were implemented to analyse the system performances and working principles, and find the optimal operating conditions. The thermodynamic simulation was obtained with the COMSOL Multiphysics® software while the chemical processes were simulated with the AspenPlus® simulation software [36][25].

7.1 AspenPlus® simulation

Multiple system configurations were analysed, with ASPEN Plus® simulation software, in order to understand the one which better simulates the recovery system.
The real system could be described as a multi flash vaporization process, with the cold top buffer slowly heated up by the vapour formed in the bottom warm buffer. Indeed, the latent heat of condensation is released by the vapour, and therefore, the top buffer temperature increases. Theoretically, the real process may be compared to an infinite series of vaporization stages, and therefore, to a simple distillation process (see chapter 4.4). Each stage represents an infinitesimal temperature increment at which an infinitesimal fraction of vapour, rich in C_4H_{10} (at the azeotropic concentration) flows out at the exhaust. On the contrary, the liquid, rich in R134a, is the bottom product of each flash unit and the feed of the successive stage. However, the recovery system is not designed with real multiple vaporization stages, since the liquid always remains in the top buffer, while it is heated up, and only during the emptying phase it is extracted.
The two analysed setups are the single and multi flash systems, and the results are shown in terms of gas quality and system efficiency. The gas quality is quantified by means of the isobutane concentration in the recovered mixture, while the efficiency is calculated with Equation 10.

$$\epsilon = \frac{m_{rec} \cdot x_{rec}}{m_{in} \cdot x_{in}} \tag{10}$$

Where m_{rec} and m_{in} are the recovered and injected mass, respectively, while x_{rec} and x_{in} are the mass fractions of R134a in the recuperated and injected mixtures. x_{rec} is usually assumed unitary (the required value is 99.9%), and x_{in} is fixed at 96.9% since the input mixture has a constant composition (see Table 6).

7.1.1 Single flash distillation

The single flash distillation unit is the simplest configuration for a separation process, formed by three streams and one *Flash2* separator as operating block (Figure 35). It performs rigorous 2 (vapor liquid) or 3 (vapor liquid liquid) phase equilibrium calculations, and produces one vapor outlet stream, one liquid outlet stream, and an optional water decant stream. It can be used to model flashes, evaporators, knock out drums, and any other single stage separators, with sufficient vapor disengagement space [37].
The flash unit simulates the top buffer only, and the influence of the bottom buffer is obtained by modifying the operating temperature.

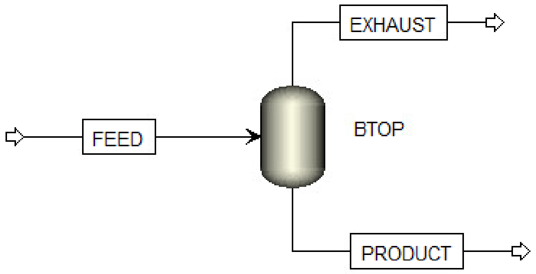

Figure 35: AspenPlus® design of a single flash distillation unit.

Stream	**Description**
FEED	Inlet liquid stream with composition 95.2% R134a, 4.5% C_4H_{10}, 0.3% SF_6
EXHAUST	Exhaust outlet stream (vapour)
PRODUCT	Outlet mixture, enriched in R134a (liquid)

Table 10: Single flash vaporization system. Stream description.

A sensitivity analysis was performed to show the correlation between gas quality and system efficiency with respect to the top buffer operating temperature (between -29.75°C and -27.25 °C with 0.25 °C step, Figure 36). Each temperature value represents a steady state condition of the simulated flash unit and, therefore, of the real top buffer.

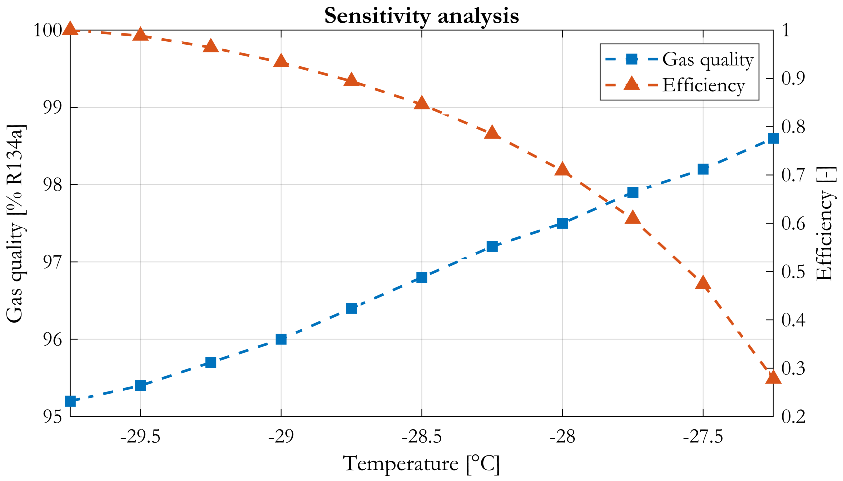

Figure 36: Sensitivity analysis on the flash unit. Gas quality (blue, left axis) and efficiency (red, right axis) trends against temperature. Increasing the temperature, the gas quality improves (higher R134a concentration in the *product stream*) and the efficiency decreases since a larger fraction of vapour leaves the system with the *exhaust stream*. The analysis shows an ideal unitary efficiency with a temperature of -29.75 °C, which is a non realistic condition for the recovery system.

7.1.2 Multi stage flash distillation

Increasing the number of stages, the distillation process fits better the bubble curve of the *T-xy equilibrium diagram* (see Figure 28), minimizing the vapour losses at the exhaust and maximizing the gas quality. The simulated system consists of five units of typology *flash2*, connected in series (the product stream of each flash is the feed stream of the following unit), with a common feeding stream and a unique exhaust obtained by mixing the exhaust lines of all units (Figure 37).

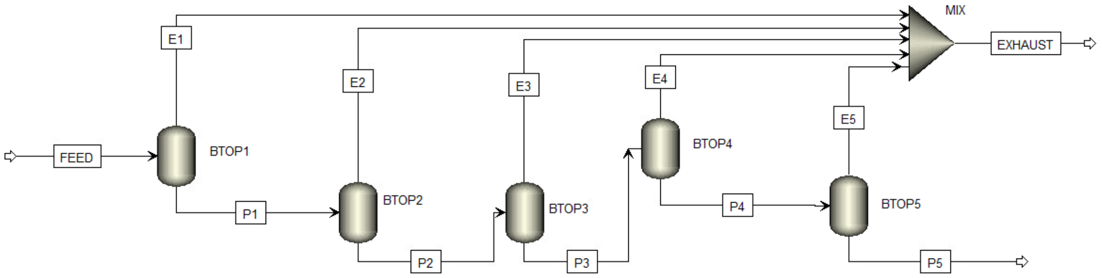

Figure 37: AspenPlus® design of a multi-flash distillation system, with five *flash2* units. Each unit represents a thermodynamic state of the top buffer: a fraction of mixture evaporates (E_i) while the remaining liquid (P_i) is heated in the following flash unit. The final product, P_5, simulates the mixture extracted from the recovery system.

A sensitivity analysis was performed to understand the effects of the number of stages on the efficiency and gas quality, knowing, from chapter 4.4, that, increasing the number of flashes, the separation process improves (Figure 38). In particular, at each stage, a temperature increment of 0.5 °C is applied to simulate the temperature increase in the top buffer (Table 11).

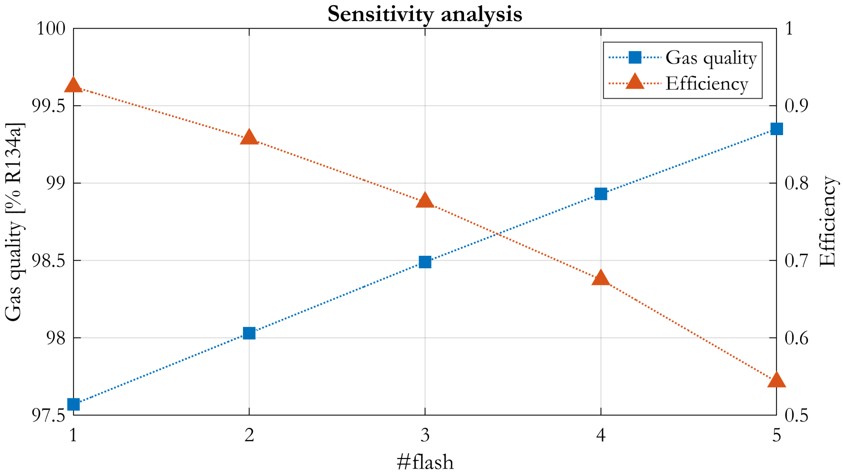

Figure 38: Sensitivity analysis on the multi-flash system. Increasing the number of stages the quality improves despite the efficiency decrement, from 0.92 down to 0.54.

#flash	T_{Btop} **[°C]**	**Quality [% R134a]**	**Efficiency**
1	-29.0	97.6	0.924
2	-28.5	98.0	0.857
3	-28.0	98.5	0.775
4	-27.5	98.9	0.675
5	-27.0	99.4	0.543

Table 11: Sensitivity analysis on the multi-flash system. Gas quality and efficiency values with the corresponding number of flash units.

7.2 COMSOL Multiphysics® simulation

The goal of the simulation was the understanding of the thermo-fluidodynamic behaviour of the new recovery system with two main scopes: define the state of matter present in the bottom buffer (liquid or vapor) and describe the liquid-vapour interaction between top and bottom buffers. The system is simulated during the distillation phase, when both filling and emptying flowrates are null.
A series of assumptions was defined to simplify the complexity of the case study (3D, two phases, transient process) and reduce the computing time:

- 2D geometry: the 2 buffers are schematized with a rectangular shape, in the xz plane. Both top and bottom buffers have the same dimensions.
- the filling transient phase is neglected, and only the distillation phase is simulated.
- laminar flow: both filling and emptying flowrates are null and the velocity field is driven by buoyancy forces only (due to the difference in vapor and liquid densities).
- the fluid properties assumed during the simulation are those of R134a. Indeed, considering that the 95.2% of the mixture is composed by R134a, the corresponding error could be neglected.

The thermodynamic analysis was performed implementing the *Laminar flow model* (chapter 7.2.3) to simulate the velocity field, the *Phase field model* (chapter 7.2.4) to simulate the liquid-vapor phase field, and the *Heat Transfer in Fluids* (chapter 7.2.5) for the heat transfer simulation. Firstly, the system was simulated with a *Steady-state study* and then with a *Time dependent study.*

7.2.1 Geometry

The dimensions of the 2D simplified geometry are reported in Table 12.

Parameter	Value
Buffer diameter	114.3 [mm]
Buffer height	232 [mm]
Pipe diameter	10 [mm]
Pipe height	50 [mm]

Table 12: 2D Geometry dimensions. The buffer height is measured from the top to the bottom points of the buffer, obtained by adding 32 mm to the distance between the two liquid sensor levels (200 mm).

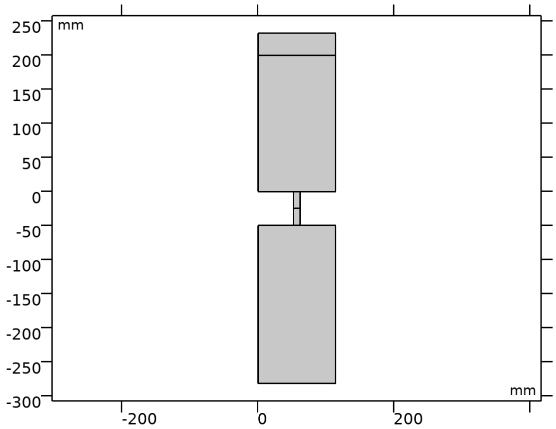

Figure 39: 2D geometry representation. The top buffer and the connecting pipe are divided in two parts to distinguish the vapor and the liquid phase (see chapter 7.2.2).

7.2.2 Material

The R134a is assumed as material for both vapor and liquid phases. From Figure 39 it can be seen that the top buffer and the connecting pipe geometries are split in two parts. Indeed, the vapour phase, in the initial conditions, is present in the top part of the top buffer, in the bottom buffer and in the bottom part of the connecting pipe. It follows that the liquid phase is in the remaining parts of the top buffer and connecting pipe.

The required thermodynamic properties for the simulation are the thermal conductivity (k), the heat capacity at constant pressure (C_P), the density (ρ), and the dynamic viscosity (η) (Figure 40).

7.2.3 Laminar Flow

As a first approximation the flow is assumed laminar. Continuity (22) and Navier-Stokes (12,13) equations are solved in the *Laminar Flow* method to find the 2D velocity field (*u(x,z)*, *w(x,z)*) in the *Steady-state study.*

$$\frac{\partial u}{\partial x} + \frac{\partial w}{\partial z} = 0 \tag{11}$$

$$\rho \left(u\frac{\partial u}{\partial x} + z\frac{\partial u}{\partial z} \right) = -\frac{\partial p}{\partial x} + \mu \left(\frac{\partial^2 u}{\partial x^2} + \frac{\partial^2 u}{\partial z^2} \right) + X \tag{12}$$

$$\rho \left(u\frac{\partial w}{\partial x} + z\frac{\partial w}{\partial z} \right), = -\frac{\partial p}{\partial z} + \mu \left(\frac{\partial^2 w}{\partial x^2} + \frac{\partial^2 w}{\partial z^2} \right) + Z \tag{13}$$

Where ρ is the fluid density, μ is the fluid dynamic viscosity, and p the pressure.

The terms on the right-hand side of the equation account for the net pressure force, the net viscous forces, and the body forces X, Z (in this study only the gravitational force is considered) [38].

A no slip boundary condition ($\mathbf{u}$=0) is applied on every wall except for the endcap of the top buffer, where an outlet boundary condition is applied. In addition, concerning the *Time dependent study*, the initial velocity is assumed as null.

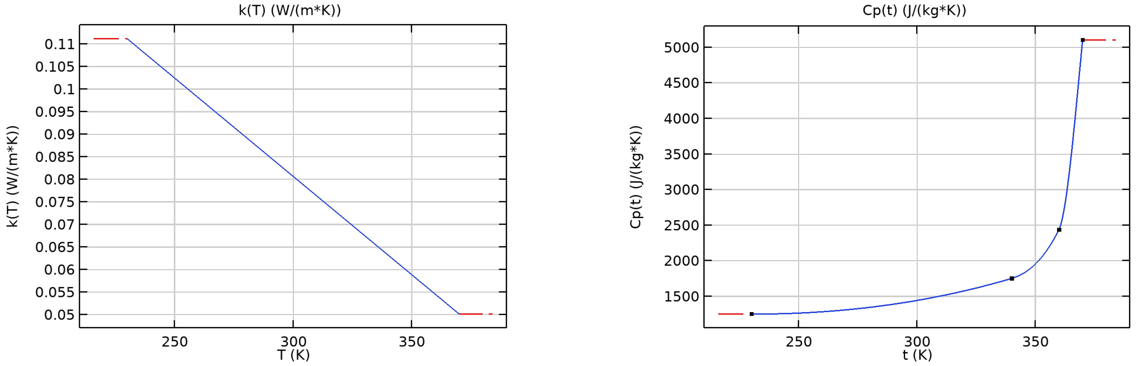

(a) Thermal conductivity. **(b)** Heat capacity at constant pressure.

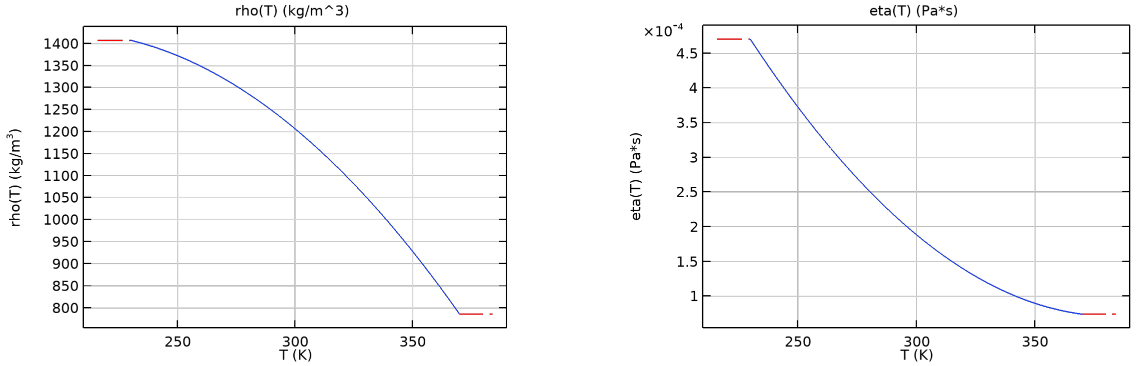

(c) Density. **(d)** Dynamic viscosity.

Figure 40: Temperature dependence of R134a thermodynamic properties.

7.2.4 Two-phase flow, Phase Field

COMSOL Multiphysics® software has four methods for modelling free liquid surfaces: level set, phase field, moving mesh, and stationary free surface [39].
The model which has been used for the simulation is the *Two-phase flow, Phase field*, already implemented in COMSOL Multiphysics. It belongs to the class of Interface Tracking Methods, useful for the multi-phase fluid visualization [40]. The main goal of these methods is to locate and determine the dynamics of the interface between fluids. These fluids may differ due to their chemical composition or due to the different physical state (in this case study, the two phases are represented by the liquid and vapor mixture). Phase field method is a field-based method in which the free fluid surface is represented as an isosurface of the phase field functions [39]. The free liquid surface corresponds to the phase boundary between the liquid and the gas and is represented on a fixed mesh. The phase field method introduces an additional scalar field (the phase field function) to the modelling domain, which varies smoothly between -1 and +1 everywhere and it is used to define the fluid viscosity and density in the governing Navier-Stokes equations [41]. In this study the vapor phase is represented by +1, while the liquid phase is labelled as -1, and, at the interface, the phase field function assumes a value of 0.
The governing equations are a type of convection–diffusion equation, with the ad-

vective velocity coming from the Navier–Stokes equations. However, such equations are quite numerically challenging to be solved due to the combination of the significant advective term, abrupt transition in the field, and strong coupling to the Navier–Stokes equations.
The phase field function Φ is the solution of Equation 14.

$$\frac{\partial \Phi}{\partial t} + u \cdot \nabla \Phi = F \tag{14}$$

Where F represents the term which minimizes the free energy of the system [39].

$$F = \nabla \cdot \frac{\gamma \lambda}{\epsilon_{pf}^2} \nabla \psi \tag{15}$$

$$\psi = -\nabla \cdot \epsilon_{pf}^2 \nabla \Phi + \left(\Phi^2 - 1\right) \Phi \tag{16}$$

$$\gamma = \frac{3 \epsilon_{pf} \sigma}{\sqrt{8}} \tag{17}$$

$$\lambda = \chi \epsilon_{pf}^2 \tag{18}$$

Where ϵ_{pf} is the interface thickness parameter set equal to 4e-4 (the optimal value should be the same value of the largest elements close to the surface) and χ is the mobility tuning parameter, which is correlated to the diffusivity of the phase field [39]. It should be large enough to guarantee the stability but small enough to obtain a sharp interface. It is proportional to the speed of the interface U and inversely proportional to the surface tension σ.

$$\chi = \frac{U h_{max}}{3\sqrt{2} \sigma \epsilon_{pf}} \tag{19}$$

Where h_{max} is the largest mesh size.

The wetted wall boundary condition is applied for every wall except for the top buffer endcap which is considered an outlet. Using the wetted wall condition, the fluid-fluid interface (in this case study liquid-vapor interface) can move along the wall and, in addition, the no-penetration condition ($u \cdot n_{wall}$=$\mathbf{0}$) is enforced [42].
Finally, the liquid and vapour initial conditions are applied as shown in Figure 41.

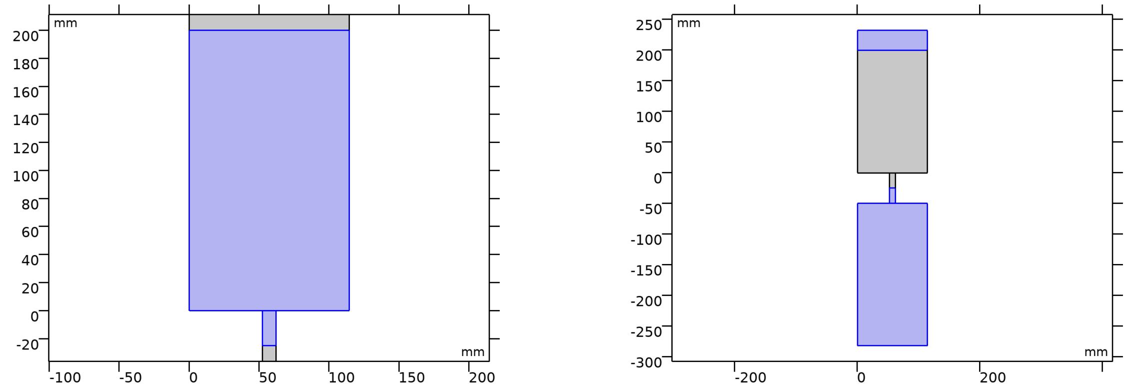

(a) Portions of top buffer and connecting pipe initially filled by mixture in liquid phase.

(b) Portions of top buffer, connecting pipe, and bottom buffer initially filled by mixture in vapour phase.

Figure 41: Phase field initial conditions.

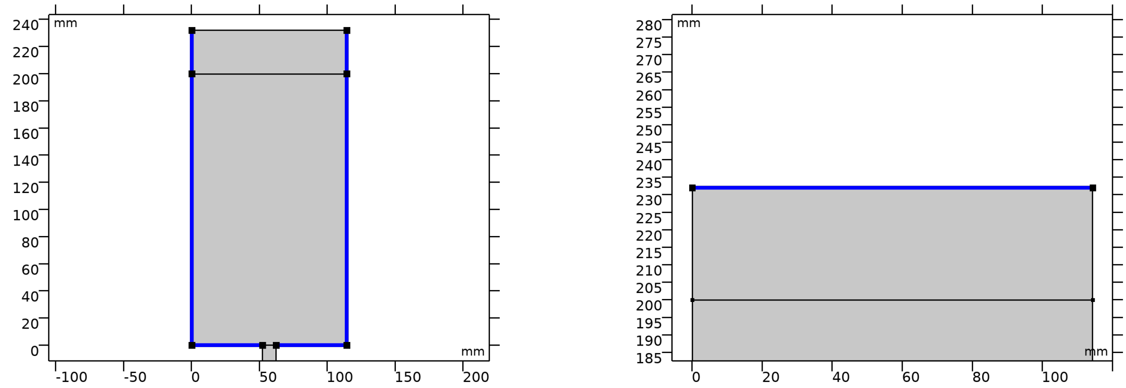

(a) Dirichlet boundary condition for the top buffer and top portion of the connecting tube, with **T = -35 °C**.

(b) Top buffer endcap is assumed as an outflow boundary.

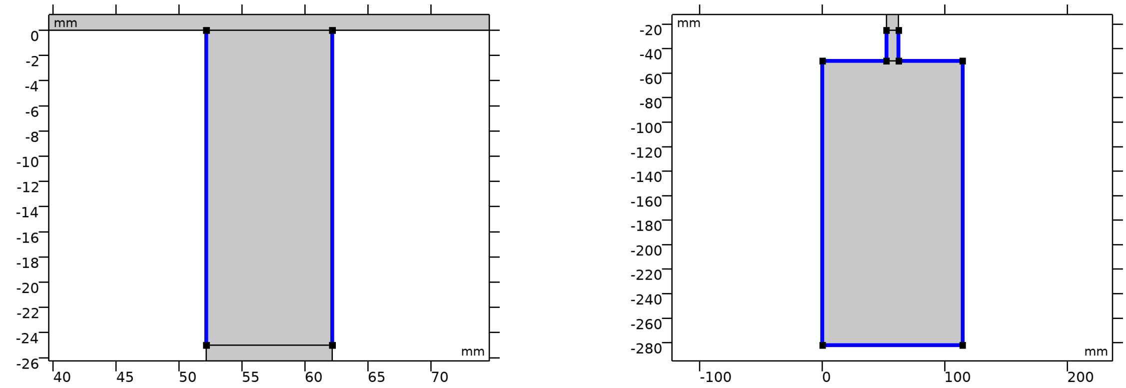

(c) Neumann homogeneous boundary condition on the top portion of the connecting tube simulating the thermal insulation ($-n \cdot q = 0$).

(d) Dirichlet boundary condition for the bottom buffer and bottom portion of the connecting tube, with **T = 10 °C**.

Figure 42: Thermal boundary conditions.

7.2.5 Heat Transfer in Fluids

The temperature field is the result of the energy conservation equation.

$$\rho c_P \left(u\frac{\partial T}{\partial x} + w\frac{\partial T}{\partial z} \right) = k \left(\frac{\partial^2 T}{\partial x^2} + \frac{\partial^2 T}{\partial z^2} \right) + \mu\Phi + \dot{q} \tag{20}$$

where T is the temperature, c_P is the specific heat at constant pressure, k is the thermal conductivity, $\dot{q}$ is the volumetric rate of thermal energy generation, and $\mu\Phi$ the *viscous dissipation.* The generation term $\dot{q}$, which characterizes the conversion from other forms of energy to thermal energy, is neglected since there are not thermal heat sources in the system. Viscous dissipation represents the net rate at which mechanical work is irreversibly converted to thermal energy due to viscous effects in the fluid [38].

The Dirichlet and Neumann boundary conditions are applied to every wall except to the top buffer endcap which is considered as an outflow (Figure 42). In addition, concerning the *Time dependent study* the entire system is assumed to be initially at an homogeneous temperature of -35.5 °C.

7.2.6 Results

Due to the high computational cost, the time dependent study has been performed for three seconds only, with a computational time of 8 h 47 min.
The **velocity** magnitude (Figure 43) at the time frame of three seconds, shows the eddies formation in the central part of the bottom buffer, with a magnitude higher than 0.6 m/s. This happens due to the liquid flowing down from the top buffer and the vapour formation in the bottom buffer. The density difference between the two phases generates the buoyancy forces which are responsible for the eddies formation that tend to homogenize the temperature in the bottom buffer (see Figure 47). Similarly, in the top buffer, the vapour encounters liquid and the buoyancy forces induce the mixture motion.

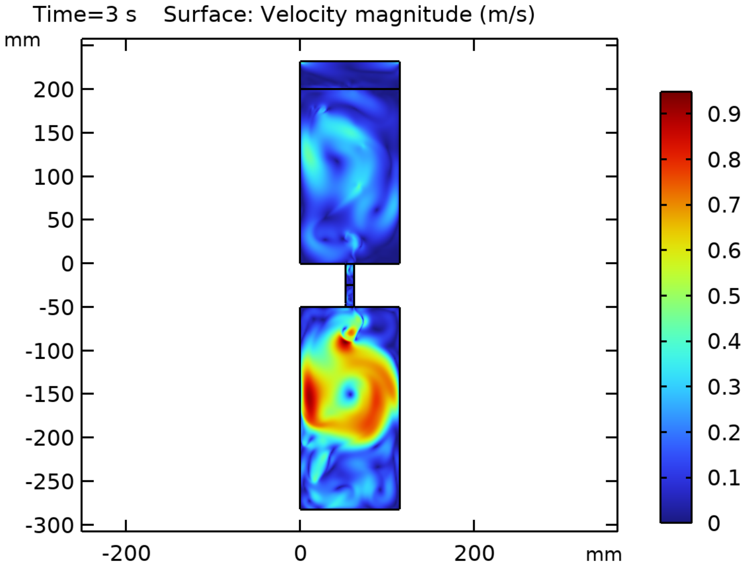

Figure 43: Time dependent study, velocity magnitude after 3 s.

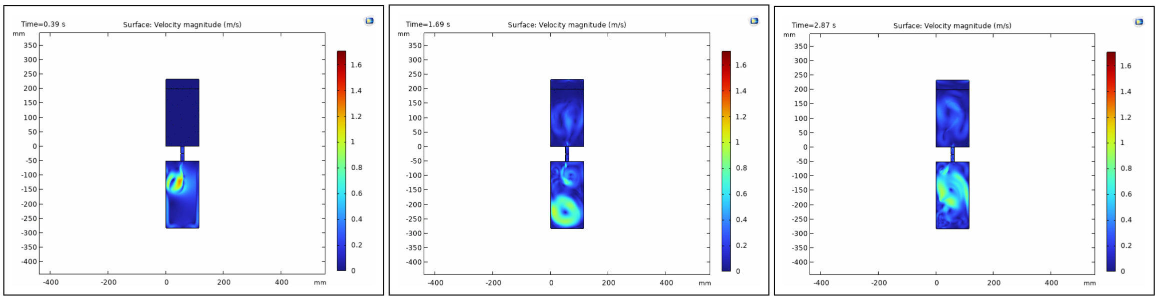

(a) Time = 0.39 s **(b)** Time = 1.69 s **(c)** Time = 2.87 s

Figure 44: Velocity field time dependent study, with three consecutive frames. The liquid accelerates exiting the connecting pipe and, after touching the walls, it evaporates and the density difference generates the eddies (more evident at 1.69 s). Similar behaviour in top buffer, with the vapour phase encountering liquid mixture and inducing velocity gradients (dark and light blue).

The **phase field** study illustrates the behaviour of the liquid-vapor mixture inside the system, allowing a better understanding of the separation process (Figure 46). The liquid phase flows through the connecting pipe from the top to the bottom buffer (Figure 46) and vaporizes, almost instantaneously, after touching the buffer walls. Afterwards, the gas bubbles flow up through the connecting pipe and start exchanging heat with the liquid mixture. Finally, vapour condensates in the top buffer, releasing heat to the liquid mixture which increases its temperature.

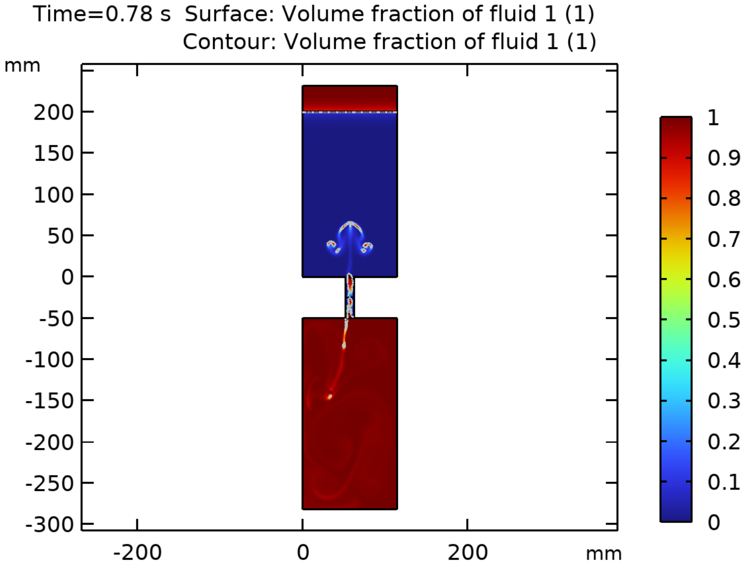

Figure 45: Phase field time dependent study of top and bottom buffers after 0.78 s. In blue the liquid and in red the vapour phase, with the colours in between representing the transition between the two phases.

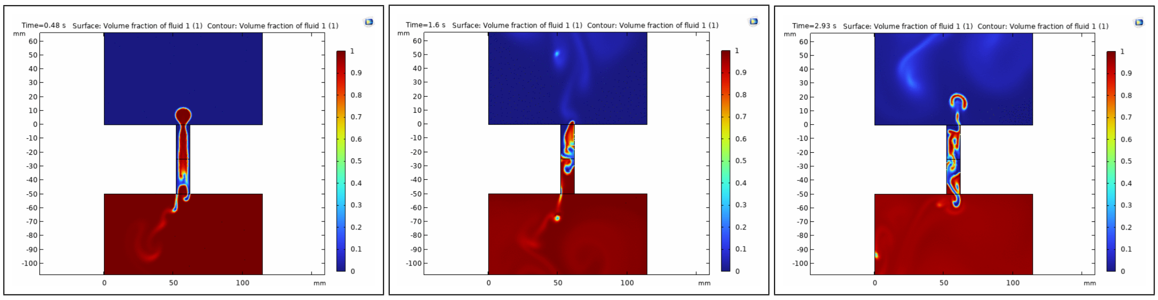

(a) Time = 0.48 s **(b)** Time = 1.60 s **(c)** Time = 2.93 s

Figure 46: Phase field time dependent study, with three consecutive frames of a zoomed view on the connecting pipe. In blue the liquid and in red the vapour phase, with the colours in between representing the transition between the two phases.

Finally, the **temperature** study shows that in the bottom buffer the entire mixture is in vapour phase due to the walls temperature of 10 °C and the R134a boiling point of -26.4 °C (at 1 bar). The bottom buffer temperature (T_{Bbot}) trend in time is shown in Figure 48. A series of three frames demonstrates that the liquid mixture in bottom buffer, after the evaporation, tends to a steady state and homogeneous temperature due to the liquid vapour mixing enhanced by the buoyancy forces (Figure 47).

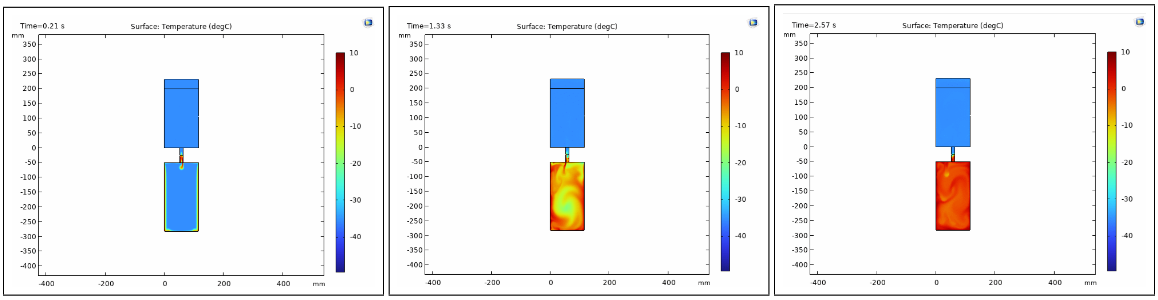

(a) Time = 0.21 s **(b)** Time = 1.33 s **(c)** Time = 2.57 s

Figure 47: Transient of the temperature field. Temperature tends to homogenize in the bottom buffer, after a transient mixing phase. In the top buffer, temperature remains steady to its initial value, since the vapour is not enough to increase it during three seconds of simulation. More time is needed to see a temperature variation.

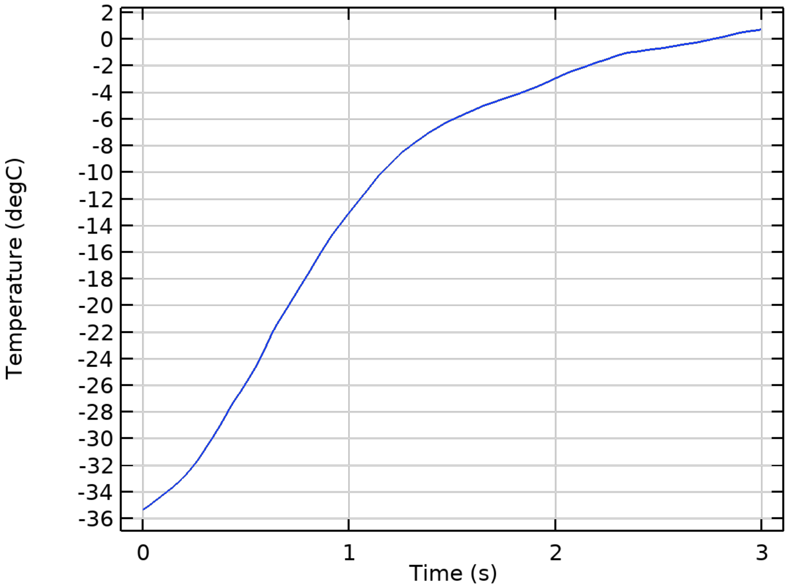

Figure 48: Average bottom buffer temperature trend in time. Starting from the initial value of -35.5 °C, T_{Bbot} increases, approaching the 0 °C after 3 seconds of simulation. More time is needed to let the temperature reach a steady state condition.

8 Test results

The recovery system was firstly tested in manual mode and then in auto mode. These tests are devoted to understanding the effects of the operating parameters on the isobutane concentrations of the recovered mixture and on the system efficiency (or recovery). In addition, the auto mode tests are focused on setting the system to let it run continuously (24 hours per day).
The main operating parameters which influence the isobutane concentration in the recovered mixture and the system recovery are the following:

- temperature of the top buffer (T_{Btop})
- pressure of the top buffer, regulated by the Zimmerli
- temperature of the bottom buffer (T_{Bbot})
- extraction flowrate, regulated by rotameter and needle valves
- distillation time

Top buffer temperature

Theoretically, increasing the temperature of the top buffer, the isobutane concentration should decrease. However, it is important to maintain this temperature within the range of -32.3 °C and -26.4 °C, which are the azeotrope and R134a boiling temperatures respectively, at 1 bar. Considering that the columns are cooled in series by the cooling loop, a temperature increment is present between each column. Therefore, it is necessary to guarantee the column 4 at a temperature lower than -26.4 °C (boiling temperature of R134a) and avoid the complete mixture evaporation. The temperature of the cooling circuit is controlled by the setpoint temperature of the cooling unit (Lauda Integral XT 280) and the system was tested under the following values: -36.5 °C, -36.2 °C, and -36.0 °C.

Top buffer pressure

Regulating the Zimmerli, it is possible to modify the pressure of the gas phase inside each column. In particular, the lower the pressure, the more is the gas flowrate leaving the buffer through the exhaust line. The Zimmerli can be manually regulated within a range of 0 and 500 mbar, and the system was tested under the following values: 10 mbar, 20 mbar, 35 mbar, and 50 mbar.

Bottom buffer temperature

The temperature regulation in the bottom buffer influences the top buffer temperature. In particular, the higher T_{Bbot} and the higher is the temperature of the vapour formed in the bottom buffer. The vapour releases its sensible and latent heat in the top buffer during condensation, increasing the temperature of the liquid mixture. The system has been tested under the following T_{Bbot} values: 14 °C, 17 °C, 20 °C, and 23 °C.

Extraction flowrate

The extraction (or emptying) flowrate is defined as the flowrate at which the recovered mixture is sent from the columns to the recuperation bottle, through the compressor and can be controlled by the rotameter (see chapter 5). According to previous studies, the extraction flowrate influences the gas quality of the recovered mixture and the higher the flowrate the higher is the concentration [23]. The recovery system has been tested with the following extraction flowrates: 500 l/h, 700 l/h, and 1000 l/h.

Distillation time

The distillation time is defined as the amount of time between the end of filling and the beginning of emptying. The longer the distillation the more should be the isobutane leaving the buffer to the exhaust. The recovery system has been tested under three different distillation times: 0 min, 30 min, and 60 min.

An additional parameter, the **filling flowrate**, does not influence the isobutane concentration of the recovered mixture, but it is fundamental for the system operation in continuous mode. Three values were tested: 200 l/h, 300 l/h, and 400 l/h.

Finally, it is worth to mention that, not only the isobutane concentration, but also the N_2 and O_2 concentrations must be minimized in the recovered mixture. Therefore, for each test, C_4H_{10}, N_2, and O_2 concentrations have been analysed with the gas chromatograph.

8.1 Filling rate

The filling rate is defined as the mixture flowrate feeding the recovery system. Instead of sending to the exhaust the mixture used in the RPCs, a fraction is recirculated as filling flowrate of the recovery system. Moreover, each column is filled one by one, at a constant flowrate. The influence of the filling rate on the efficiency and isobutane concentration is shown in test 42, 43 and 44, with filling rates of 400 l/h, 200 l/h, and 300 l/h respectively, involving columns 1 and 3 only (Table 13).

Filling rate [l/h]	C_4H_{10} **[ppm]**	N_2 **[ppm]**	O_2 **[ppm]**	**Efficiency [%]**
400	1000	170	20	73
300	950	250	30	74
200	1100	47	5	78

Table 13: Gas quality and efficiency values at different filling rates.

Theoretically, by reducing the filling rate $\dot{m}_m$, a temperature reduction at the heat exchanger outlet (mixture side) is expected. Considering the first thermodynamic law, the energy balance on the heat exchanger can be expressed as follow, if an ideal behaviour is assumed:

$$\dot{m}_m c_{p,m}(T_{IN,m} - T_{OUT,m}) = \dot{m}_c c_{p,c}(T_{OUT,c} - T_{IN,c}) = \dot{Q} \tag{21}$$

where $\dot{m}_m$ and $\dot{m}_c$ are the mixture and coolant mass flowrates, $c_{p,m}$ and $c_{p,c}$ are the mixture and coolant specific heat capacities, $T_{IN,m}$ ($T_{OUT,m}$) and $T_{IN,c}$ ($T_{OUT,c}$) are the mixture and coolant inlet (outlet) temperatures, $\dot{Q}$ the thermal power subtracted to the gas mixture for liquefying. Considering approximately constant $\dot{Q}$, $T_{IN,m}$ and $c_{p,m}$, a $\dot{m}_m$ reduction induces a $T_{OUT,m}$ reduction as shown in Table 14.

Filling rate [l/h]	$T_{OUT,m}$ [°C]	T_{Lauda} [°C]
400	-28.1	-36.2
300	-28.4	-36.2
200	-28.5	-36.2

Table 14: Filling rate effect on the heat exchanger outlet temperature, with a constant Lauda setpoint temperature.

The gas quality seems not affected by the filling rate, with an average isobutane of 1000 ppm, while the efficiency changes by 5% with a filling rate variation of 200 l/h (Table 13). Indeed, reducing the filling flowrate, the mixture temperature at the heat exchanger outlet ($T_{OUT,m}$) decreases and therefore a lower amount of gas is lost through the exhaust line (Figure 49).

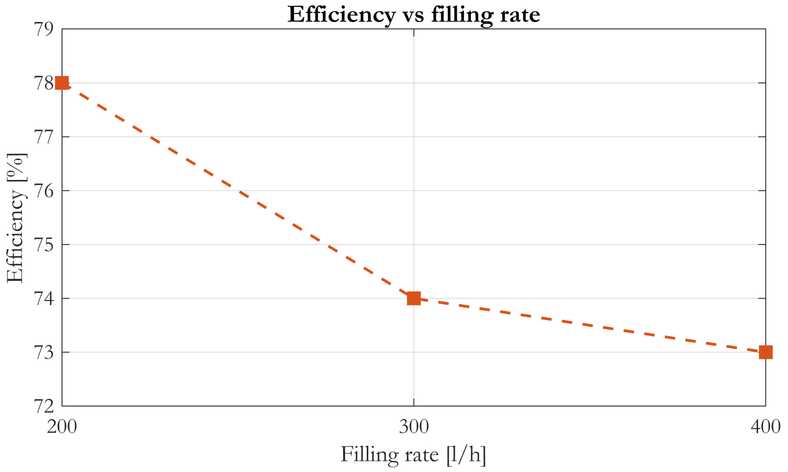

Figure 49: Efficiency versus filling rate. A non-linear trend is present, with an initial slope of 4% per 100l/h and then 1% per 100 l/h.

8.1.1 Theoretical normalised filling rate

A theoretical filling rate measured in mbar/h and normalized for a filling flowrate of 100 l/h for 1 hour operation, can be evaluated using the continuity equation and Stevin's law. The continuity equation is applied to the heat exchanger, where the input gas mass flowrate must be equal to the output liquid mass flowrate. Then, Stevin's law is applied to the top buffer to evaluate the pressure difference after 1 hour of mixture injection at 100 l/h. The calculations are done under the following assumptions:

- Constant input flowrate (100 l/h)
- No pressure drops across the heat exchanger
- Top buffer perfectly cylindrical (in the two hemispherical endcaps the liquid level does not increase uniformly due to the cross-section area variation)
- The mixture density is approximated to the R134a density, both for liquid and gas phase (acceptable approximation considering that the R134a represents the 95.2% of the mixture)
- The thermodynamic data are taken from the NIST (National Institute of Standards and Technology) database [24]

Parameter	**Value**	
ρ_g [kg/m^3]	4.28	Gas density at 20 °C and 1 bar
Q_g [l/h]	100	Inlet volumetric flowrate
ρ_l [kg/m^3]	1388	Liquid density at -35°C and 1 bar
D [m]	0.114	Top buffer diameter
A [m^2]	0.0102	Top buffer cross-section area

Table 15: Useful parameters for calculating the normalised filling rate.

From the continuity equation the expression of Δh[2] is obtained.

$$\rho_g Q_g = \rho_l Q_l \tag{22}$$

$$Q_l \cdot 1[h] = \frac{\rho_g Q_g}{\rho_l} \cdot 1[h] = \Delta h \cdot A \tag{23}$$

$$\Delta h = \frac{\rho_g Q_g \cdot 1[h]}{\rho_l A} \tag{24}$$

The corresponding pressure difference Δp is derived from the Stevin's law.

$$\Delta p = \rho_l g \Delta h = \rho_l g \cdot \frac{\rho_g Q_g \cdot 1[h]}{\rho_l A} = 4.2 mbar \tag{25}$$

In conclusion, when a column is filled for 1 hour at 100 l/h, the maximum Δp achievable is 4.2 mbar. Lower values are obtained if a fraction of gas mixture is lost at the exhaust during the filling time. The more the gas lost, the lower the normalized filling rate with respect to the theoretical one.
This theoretical behaviour is reflected in every test, and useful results are reported concerning test 42, 43, and 44 (Table 16).

---

[2] Δh is the liquid level reached in the top buffer after 1 hour of filling at 100 l/h.

Test n.°	**Filling flowrate**	**C1** [mbar/h @ 100 l/h]	**C3** [mbar/h @ 100 l/h]
42	400	4.35	2.65
44	300	3.26	1.57
43	200	2.16	1.07

Table 16: Columns 1 and 3 normalised filling rates at different filling flowrates. The values are obtained dividing by 4, 3, and 2, the filling rates obtained with 400, 300, and 200 l/h respectively.

It is worth to notice that column 3 has a lower normalized filling rate in all three tests. In particular, its value is almost one half of the corresponding column 1, meaning that a larger amount of gas during the filling phase is sent to the exhaust and the column requires more time to reach the full state mode. This behaviour may be explained by the temperature increment between C1 and C3, due to the presence of a cooling system connected in series with the four columns.

8.2 Extraction flowrate

The system was tested in manual mode, under three different conditions of extraction flowrate, to confirm the trend already obtained for the prototype [23][43]. The previous studies show an increasing gas quality (lower isobutane concentration in the recovered mixture) by reducing the extraction flowrate. It might be explained by the difference between the time required for heat exchange and the effective time of interaction of the liquid mixture and the bottom buffer. Indeed, a well performant heat exchange allows a better gas separation. Therefore, the higher the flowrate, the higher is the C_4H_{10} concentration, due to the low interaction time between the mixture and the bottom buffer.

The tests were run for columns 1 and 4, at 500 l/h, 700 l/h, and 1000 l/h, in manual mode. Only these two columns were tested, since C2 and C3 have the same dimensions of C1 and C4 respectively. Considering that the rotameter reads air based flowrates, a conversion factor of 3.5 was considered to define the real extraction rate.

The influence of the extraction flowrate on the isobutane concentration and system efficiency is shown with the tests listed in Table 17.

Test n.°	**Column**	**Extraction rate (real flowrate) [l/h]**
12	1	500 (150)
13	1	700 (200)
17	1	1000 (290)
21	4	500 (150)
22	4	700 (200)
18	4	1000 (290)

Table 17: Test number and corresponding extraction flowrate.

All tests were performed under the operating conditions expresses in Table 18.

Parameter	**C1**	**C4**
$T_{mix,in}$ [°C]	-28.1	-27.8
T_{Btop} [°C]	-28.7	-28.9
T_{Bbot} [°C]	20.2	19.3
T_{Lauda} [°C]	-36.5	-36.5
p_{zim} [mbar]	20	20
Filling rate [l/h]	400	400
Distillation time [min]	0	0

Table 18: Operating conditions for tests listed in Table 17. $T_{mix,in}$ is the mixture top buffer inlet temperature (and heat exchanger outlet temperature), T_{Btop} the top buffer temperature, T_{Bbot} the bottom buffer temperature, T_{Lauda} the Lauda setpoint temperature, and p_{zim} the gas phase pressure in the top buffer, regulated by the Zimmerli.

8.2.1 Test 12

In *Test 12*, column 1 is run with an extraction rate of 500 l/h (real flowrate 150 l/h). The trends for nitrogen, oxygen and isobutane concentrations are shown in Figure 50.

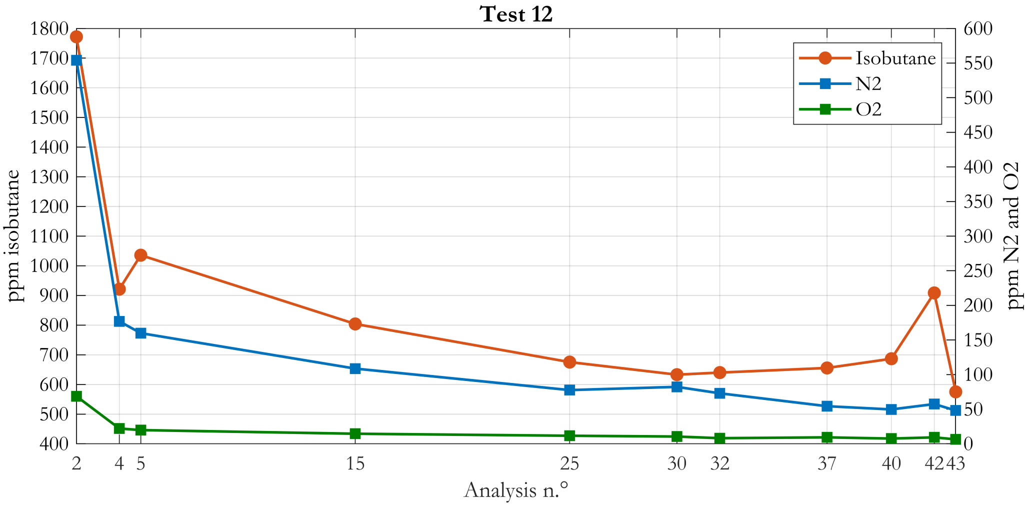

Figure 50: Test 12. Nitrogen, oxygen and isobutane after pump concentrations. The initial nitrogen and oxygen peaks are due to the presence of air in the gas chromatograph at the beginning of the analyses.

Despite the final peak, a decreasing trend in the isobutane concentration can be observed, meaning that the quality of the recovered mixture is not constant during the extraction phase, but it increases. This behaviour may be explained by the presence of a further distillation during the extraction time (180 min) which allows the isobutane to leave the column to the exhaust line and consequently to have a lower C_4H_{10} concentration in the last extraction steps, with an overall value of 840 ppm as shown in Table 19.

Component	Concentration
Average isobutane	840 ppm
Average nitrogen	130 ppm
Average oxygen	15 ppm

Table 19: Test 12. Isobutane, nitrogen, and oxygen average concentrations.

8.2.2 Test 13

In *Test 13*, column 1 is tested with an extraction rate of 700 l/h (real flowrate 200 l/h).

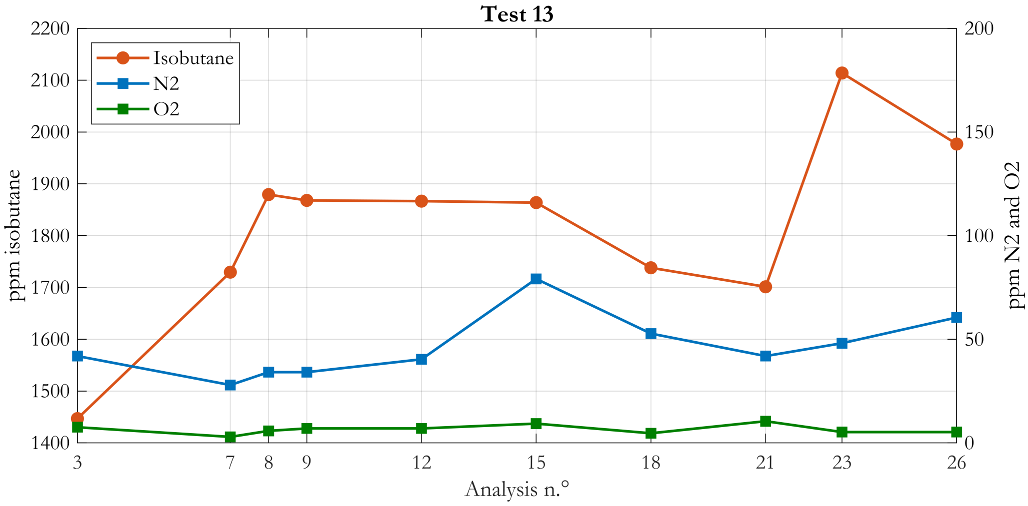

Figure 51: Test 13. Nitrogen, oxygen and isobutane after pump concentrations.

Component	Concentration
Average isobutane	1800 ppm
Average nitrogen	46 ppm
Average oxygen	7 ppm

Table 20: Test 13. Isobutane, nitrogen, and oxygen average concentrations.

From Figure 51 it can be seen that the air concentration, evaluated as the sum of N_2 and O_2 concentrations, is stable within a range of 50 and 60 ppm.
On the other hand, the isobutane concentration seems not constant with the analyses, with a stable trend only between analysis 7 and 15. The initial increase may be due to the transient phase for the gas chromatograph before reaching the steady

state analyses. Indeed, it was noticed for all tests, that at least 7/8 analyses are required to reach the steady state regime. Finally, the peak in analysis 23 may be correlated to the presence of a high isobutane concentrated "bubble" in the extracted mixture, since the following analysis shows a decreasing trend.

8.2.3 Test 17

In *Test 17*, column 1 is run with an extraction rate of 1000 l/h (real flowrate 290 l/h).

Table 21 shows an average air concentration of 2000 ppm, mainly correlated to the high nitrogen concentration in the first analyses (10 to 15), probably related to the presence of air in the gas chromatograph at the beginning of the analyses. In fact, a decreasing trend in O_2 and N_2 concentrations can be observed.

For what concerns the isobutane, it can be noticed an increasing trend in time, differently from test 12 and 13 (Figure 52). This trend might be explained considering that the high emptying rate does not allow a proper distillation, because the heat exchange between the liquid mixture, flowing through the bottom buffer, and the bottom buffer is not enough to sufficiently increase the temperature and separate the isobutane from the R134a. In addition, a second hypothesis on the increasing trend, may be the mixture stratification, with the C_4H_{10} mostly concentrated on the top layers, extracted at the end of the emptying phase. However, this trend can be only seen with an emptying rate of 1000 l/h.

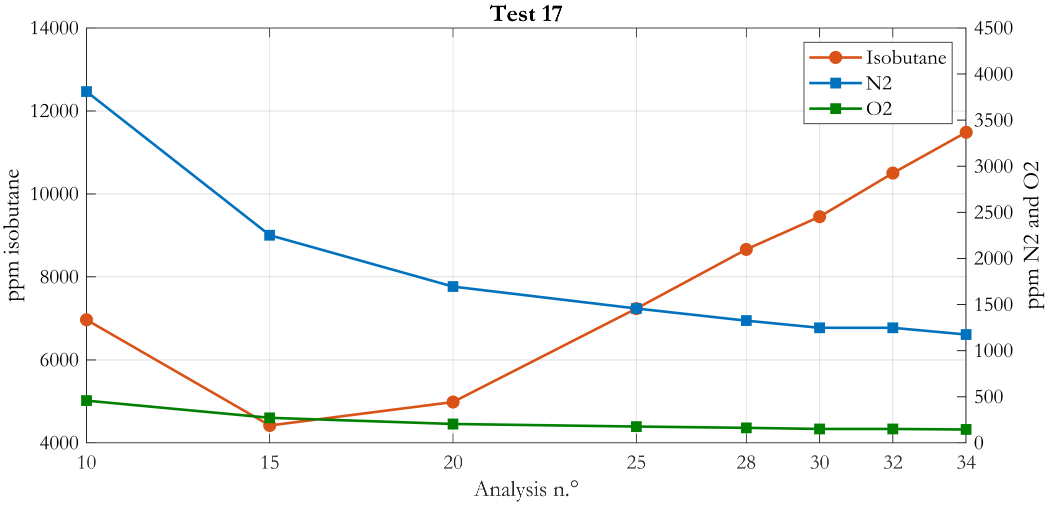

Figure 52: Test 17. Nitrogen, oxygen and isobutane after pump concentrations.

Component	Concentration
Average isobutane	8000 ppm
Average nitrogen	1800 ppm
Average oxygen	200 ppm

Table 21: Test 17. Isobutane, nitrogen, and oxygen average concentrations.

8.2.4 Test 21

In *Test 21*, the recovered mixture is extracted with a flowrate of 500 l/h (real flowrate 150 l/h). The nitrogen, oxygen, and isobutane concentration trends are shown in Figure 53.

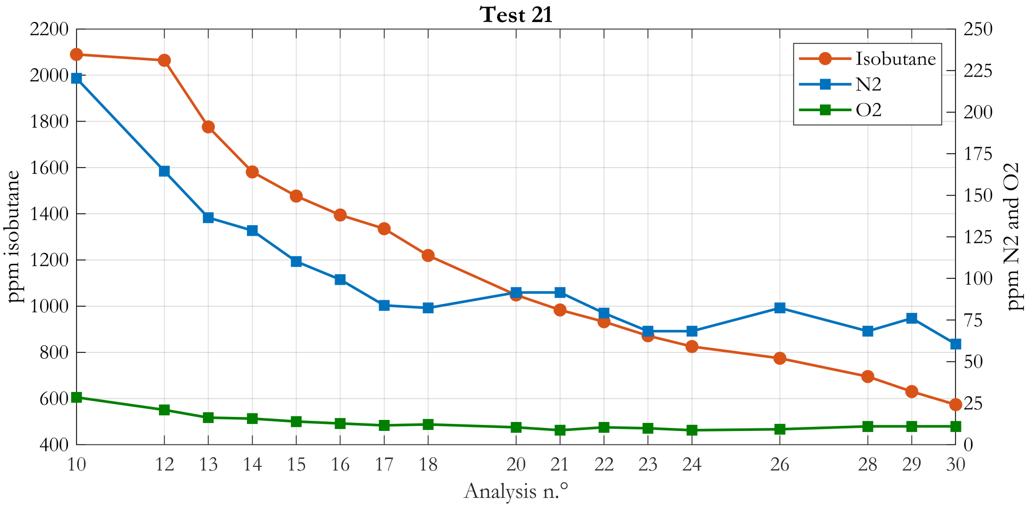

Figure 53: Test 21. Nitrogen, oxygen and isobutane after pump concentrations.

Component	**Concentration**
Average isobutane	980 ppm
Average nitrogen	82 ppm
Average oxygen	10 ppm

Table 22: Test 21. Isobutane, nitrogen, and oxygen average concentrations.

As for test 17, the first analyses show a high air concentration, with a decreasing trend and an average value between 80 ppm and 90 ppm.
Similarly, the isobutane concentration decreases in time, as for Test 12 (column 1), suggesting a mixture stratification, with lower C_4H_{10} concentration in the upper layers, or an improved distillation during the extraction phase thanks to the low flowrate (see chapter 8.2.1).

8.2.5 Test 22

In *Test 22*, the recovered mixture is extracted with a flowrate of 700 l/h (real flowrate of 200 l/h).
From Table 23 it can be seen that the average isobutane concentration is similar to the value obtained with an emptying rate of 500 l/h. However, this trend is specific for column 4 only, since for column 1 there is almost 1000 ppm difference between 500 l/h and 700 l/h. This behaviour may be a consequence of the higher temperature of C4 with respect to C1, which allows a better distillation (but lower efficiency) independently from the emptying rate.
As for Test 21, the isobutane decreases with the analyses and the air concentration, after the 9th analysis, stabilises at a value lower than 60 ppm (Figure 54).

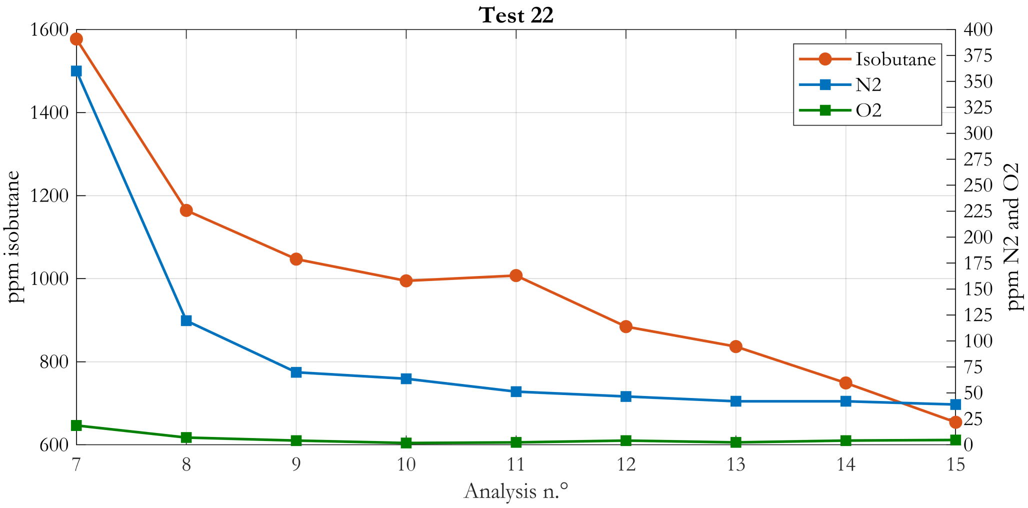

Figure 54: Test 22. Nitrogen, oxygen and isobutane after pump concentrations.

Component	Concentration
Average isobutane	990 ppm
Average nitrogen	90 ppm
Average oxygen	5 ppm

Table 23: Test 22. Isobutane, nitrogen, and oxygen average concentrations.

8.2.6 Test 18

During *Test 18*, the recovered mixture is extracted with a flowrate of 1000 l/h (real flowrate 290 l/h).
From Table 24 it can be noticed that, similar to *Test 17*, the air concentration is high, with an average of 1130 ppm. Considering that both tests (17 and 18) have been done consequently the same day, and that in the other tests the air concentration was much lower, it is possible to conclude that the high N_2 and O_2 concentrations are due to the air injection in the system after opening the lines (e.g., exhaust lines

were opened to connect the mass flowmeter for monitoring the exhaust flow for tests 17 and 18).

Finally, the high isobutane concentration, even with a decreasing trend, is related to the high extraction flowrate, as for Test 17 (see chapter 8.2.3).

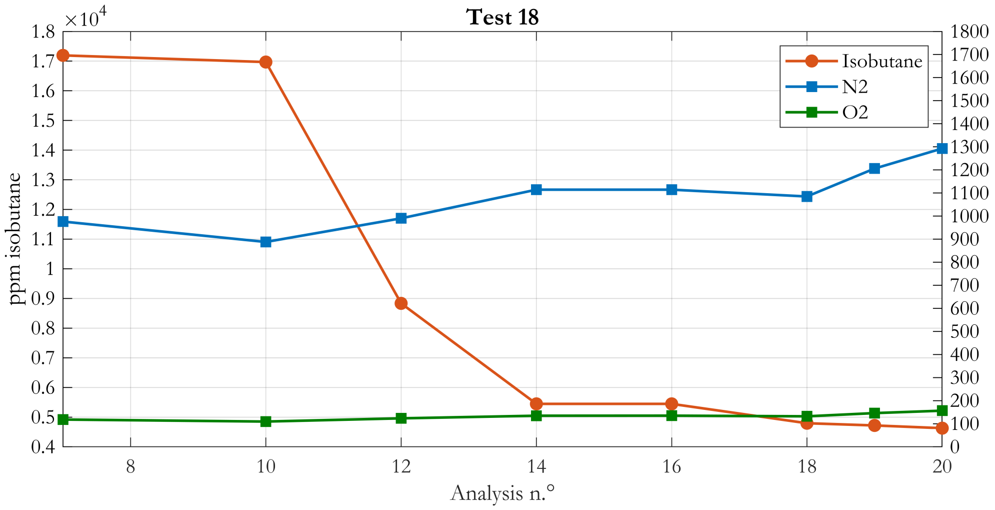

Figure 55: Test 18. Nitrogen, oxygen and isobutane after pump concentrations.

Component	**Concentration**
Average isobutane	8500 ppm
Average nitrogen	1000 ppm
Average oxygen	130 ppm

Table 24: Test 18. Isobutane, nitrogen, and oxygen average concentrations.

8.2.7 C1 and C4 comparison

The previous tests show a non-linear reduction of the isobutane concentration with respect to the emptying rate. For both columns, a larger reduction occurs decreasing the flowrate from 1000 l/h to 700 l/h, rather than decreasing between 700 l/h and 500 l/h. Column 1 and column 4 trends are reported in Figure 56 and Figure 57 respectively.

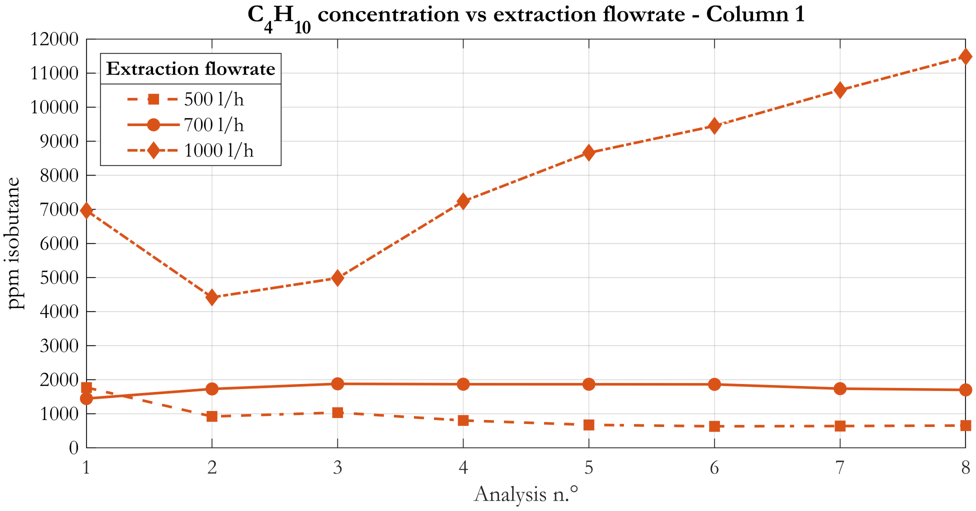

Figure 56: Isobutane concentration trends at 500 l/h, 700 l/h, and 1000 l/h for column 1. The trend at 1000 l/h is unique, since the C_4H_{10} increases during the emptying, maybe due to the low temperature of C1 and a mixture stratification in the top buffer.

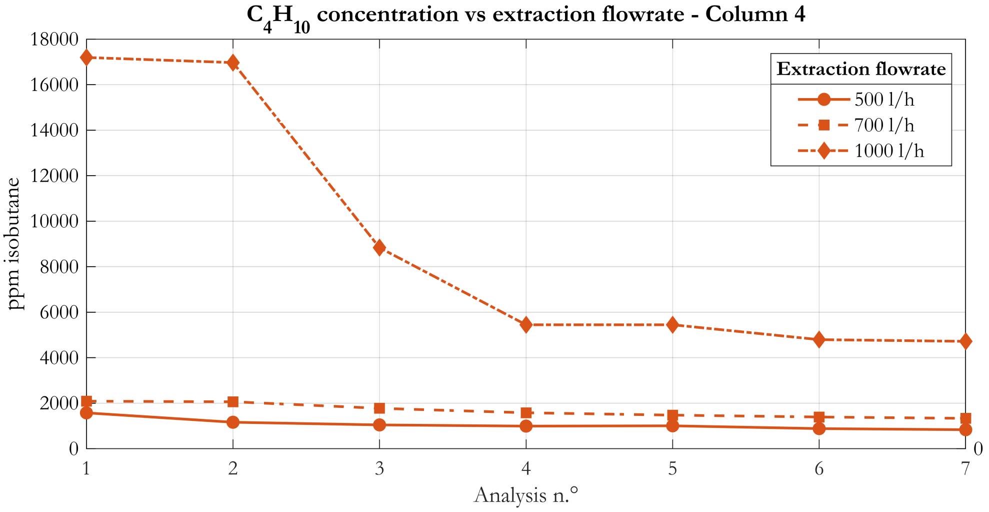

Figure 57: Isobutane concentration trends at 500 l/h, 700 l/h, and 1000 l/h for column 4. Different from C1, a slightly lower isobutane concentration can be observed at 700 l/h rather than at 500 l/h.

Test 12 and 21, performed with an extraction rate of 500 l/h, are the most performant in terms of isobutane concentration, and a compartison between the two

may be useful to find a correlation between C1 and C4, which differ in dimensions (see Appendix C) and temperature (C1 is at the beginning of the cooling circuit while C4 is at the end).
From Figure 58 it is clear that, an emptying rate of 500 l/h leads to similar results for both column 1 and 4, with an average isobutane concentration of 840 ppm and 980 ppm respectively. However, even if for C4 the average concentration is higher, a more evident decreasing trend is present. This behaviour may be related to the bottom buffer dimensions, which is higher in column 4 with respect to column 1. A higher buffer guarantees more time for the heat exchange when the liquid mixture flows down from the top buffer during the emptying phase, with a consequent better distillation, resulting in a lower isobutane concentrations. Finally, a second possible reasoning may be related to the better stratification occurring in C4 top buffers, with a consequent reduction of C_4H_{10} in time.

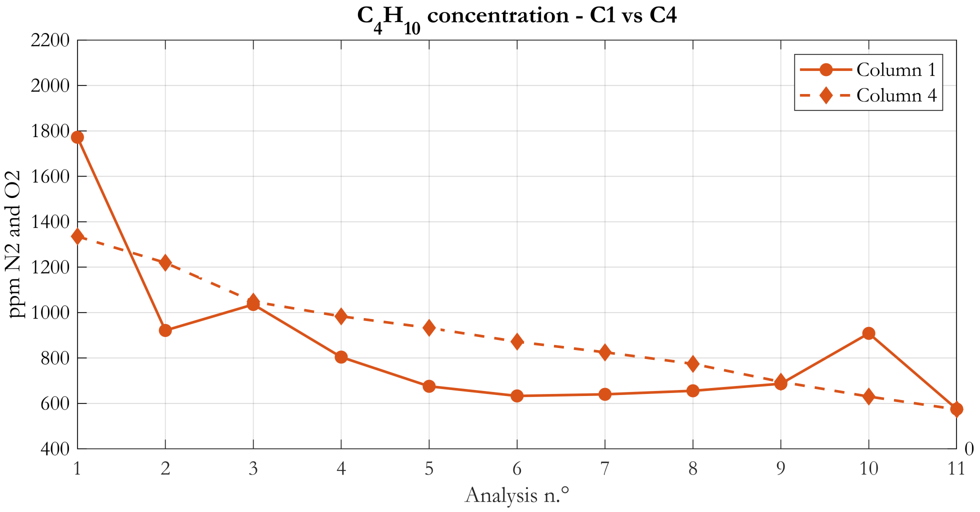

Figure 58: C1 and C4 isobutane trends at 500 l/h extraction rate.

8.2.8 Non return and needle valves

In Test 16, during the emptying phase of columns 1 and 2, some issues were encountered: the two columns were not emptied with the same extraction flowrate and a fraction of the extracted mixture flew from a column to the other one (backflow issue). These problems may be explained by the pressure difference between C1 and C2 bottom buffers. In fact, during the C1 emptying phase the bottom buffer pressure decreases, while the C2 bottom pressure increases during the filling phase (Figure 60). It is clear that C1 and C2 are fluidodynamically connected, since the bottom buffer pressures show the same trend when both pneumatic valves (YV-10111 and YV-10211) are open (both C1 and C2 in extraction). As soon as C2 starts the extraction, the two bottom pressures tend to equilibrate, with a fraction of the extracted flowrate from C2 (at higher pressure) flows to C1 (at lower pressure). In addition, the C1 top buffer DPT increases due to the flow injection. Finally, C2 tends to empty faster than C1, with an extraction time of 130 min instead of 200 min.
Thus, to avoid problems of backflows and undesired fast emptying rate (with con-

sequent increasing of isobutane concentration in the recovered mixture), a new system configuration has been adopted modifying the setup downstream the pneumatic valves (YV-10111, YV-10211, YV-10311, and YV-10411). For each column, a non-return valve to avoid backflow issues and a needle valve to regulate the emptying rate were added (Figure 59).

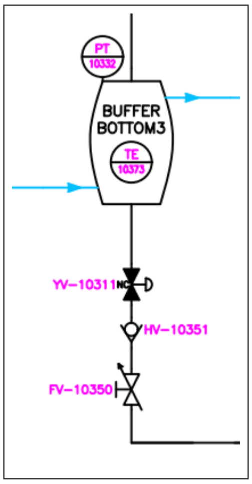

Figure 59: New column configruation with the addition of non-return and needle valves.

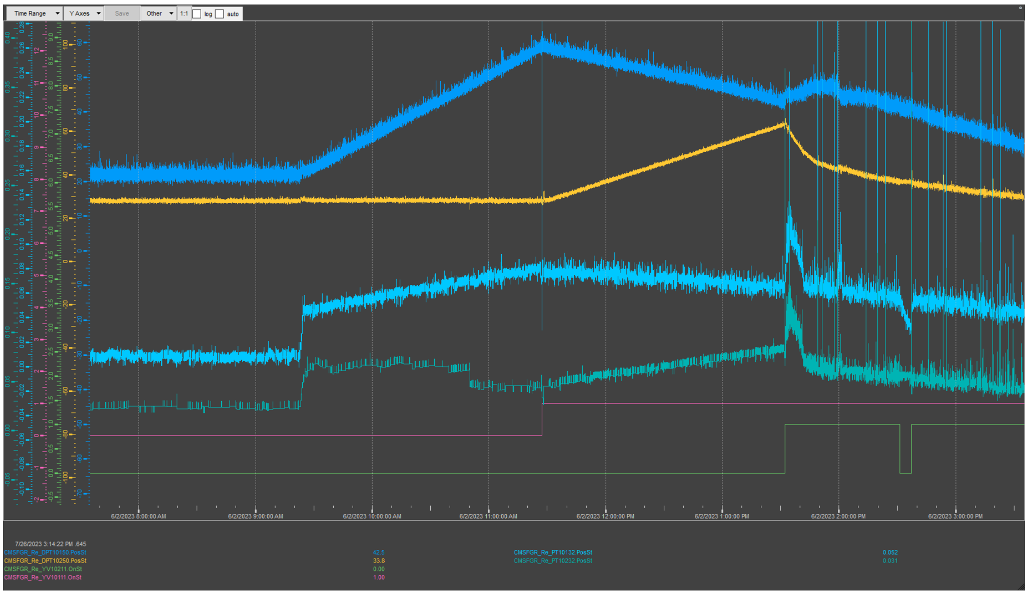

```
7/26/2023 3:14:22 PM .645
CMSFGR_Re_DPT10150.PosSt      42.5      CMSFGR_Re_PT10132.PosSt      0.052
CMSFGR_Re_DPT10250.PosSt      33.8      CMSFGR_Re_PT10232.PosSt      0.031
CMSFGR_Re_YV10211.OnSt        0.00
CMSFGR_Re_YV10111.OnSt        1.00
```

Figure 60: C1 and C2 pressure trends during the extraction phase in test 16. C1 top buffer differential pressure (dark blue), C2 top buffer differential pressure (yellow), C1 bottom buffer pressure (light blue), C2 bottom buffer pressure (aqua green), C1 pneumatic valve (purple), and C2 pneumatic valve (light green). When the C2 pneumatic valve turns on, the bottom buffer pressures show a peak and tend to equilibrate, while the yellow line steeply decreases and the dark blue increases.

8.3 Top buffer temperature

The third parameter which influences the system operation is the top buffer temperature, controlled by an external cooling unit (Lauda Integral XT 280) and a cooling circuit connected in series with the four columns. Three temperature values were set, -36.5 °C, -36.2 °C, and -36 °C, and the analyses were taken from tests 38, 41, and 42.

However, during test 38, performed the 10^{th} July, the cooling unit was not able to maintain the set point temperature of -36.5 °C, and an increment of 0.5 °C was observed, probably due the increasing of the external ambient temperature (close to 30 °C, see chapter 8.3.4). It is necessary to avoid undesired temperature increments because they influence the separation process, decreasing the isobutane concentration in the recovered mixture, but reducing (also significantly) the system efficiency. Finally, column 4 has been disabled due to its low efficiency (lower than 20%) as a consequence of its high temperature which causes the complete vaporisation of the input mixture during the filling state, without C_4H_{10} and R134a separation.

8.3.1 Test 38 (-36 °C)

Test 38 was run with the Lauda setpoint of -36.5 °C, but the output temperature was stable at -36 °C due to a non-efficient heat dissipation of the cooling unit (see chapter 8.3.4). The additional test conditions are reported in Table 25.

	C1	**C2**	**C3**
$T_{minx,IN}$ **[°C]**	-28.5	-28.1	-27.7
T_{Btop} **[°C]**	-30.3	-27.8	-27.3
T_{Bbot} **[°C]**	19.8	19.5	19.5
T_{Lauda} **[°C]**	-36.5	-36.5	-36.5
p_{zim} **[mbar]**	10	10	20
Filling flowrate [l/h]	400	400	400
Normalised filling rate [mbar/h]	3.95	3.96	2.25

Table 25: Test 38 operating conditions. The Lauda set point is -36.5 °C but the real output temperature was oscillating around -36 °C due to inefficient heat exchange with the environment.

From the isobutane curve (Figure 61), it is clear that a decreasing trend is present at the end of the emptying phase for each column. This behaviour may suggest a reduction of the isobutane concentration during the column emptying, due to the higher distillation time for the last fraction of liquid in the top buffer. Moreover, C2 shows a better gas quality than C1 thanks to its higher temperature. Finally, the air concentration decreases during the analyses (especially N_2 concentration) down to stable values of 25 ppm and 5 ppm respectively. The initial concentration is due to the undesired air injected in the GC when no columns were emptying and thus no mixture was sent to the gas chromatograph. Finally, from Table 25 it is evident that column 3 has a lower filling rate due to the higher gas flowrate at the exhaust. This may be caused by the higher temperature with respect to columns 1 and 2, and due to the different buffer dimensions (see Appendix C).

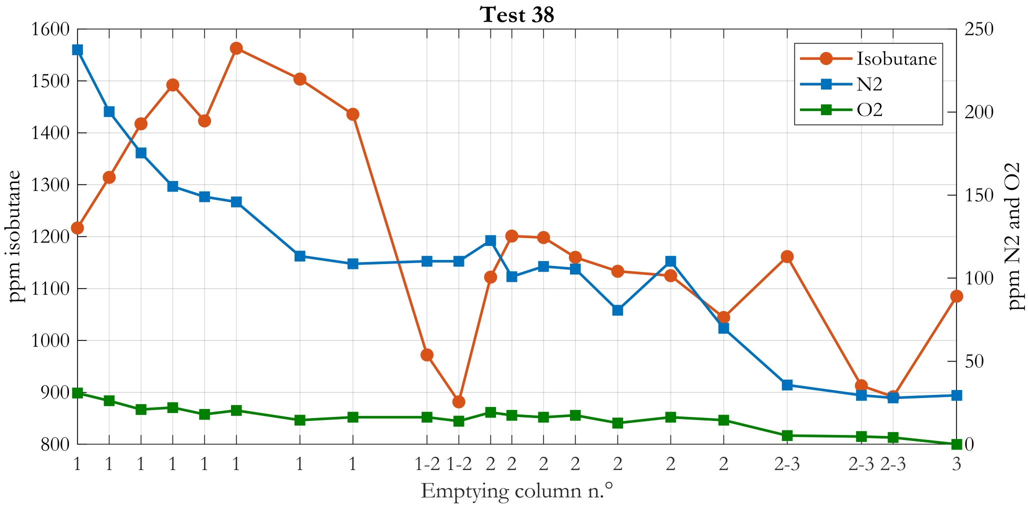

Figure 61: Test 38. Nitrogen, oxygen and isobutane after pump concentrations in time.

Component	Value
Average isobutane	1000 ppm
Average nitrogen	110 ppm
Average oxygen	15 ppm
Efficiency	70%

Table 26: Test 38. Isobutane, nitrogen, oxygen average concentrations and efficiency.

8.3.2 Test 41 (-36.5 °C)

After fixing the issue related to the high room temperature, *Test 41* was done with a stable Lauda setpoint temperature of -36.5 °C. In addition, the top buffer pressure was regulated at 50 mbar for column 3, to reduce the gas flowrate at the exhaust and thus, increase the efficiency. All the test conditions are listed in Table 27.
Table 28 shows an air concentration almost null and an average isobutane concentration of 1440 ppm, higher than test 38. Indeed, a lower cooling setpoint temperature (even a 0.5 °C difference) may induce a reduction in the recovered gas quality, increasing the efficiency. Similar to test 38, a decreasing trend in the isobutane concentration can be seen during the emptying phase of each column (Figure 62).

Considering the low efficiency of test 38 (below the desired value of 80%), an additional parameter has been regulated during test 41, the top buffer pressure. In particular, the Zimmerli of column 3 was set to 50 mbar, from 20 mbar of test 38, in order to increase the pressure at which the gas flows through the exhaust line, reducing the exhaust flowrate and thus improving the efficiency. The other columns are maintained at 10 mbar, considering their lower temperature with respect to C3. Under this condition, an efficiency of 76% was achieved, and therefore the same top pressure value has been maintained for the following tests.

	C1	**C2**	**C3**
$T_{minx,IN}$ [°C]	-29.0	-28.5	-27.6
T_{Btop} [°C]	-30.5	-28.3	-27.8
T_{Bbot} [°C]	19.5	19.5	19.5
T_{Lauda} [°C]	-36.5	-36.5	-36.5
p_{zim} [mbar]	10	10	50
Filling flowrate [l/h]	400	400	400
Normalised filling rate [mbar/h]	4.28	4.13	2.48

Table 27: Test 41 operating conditions.

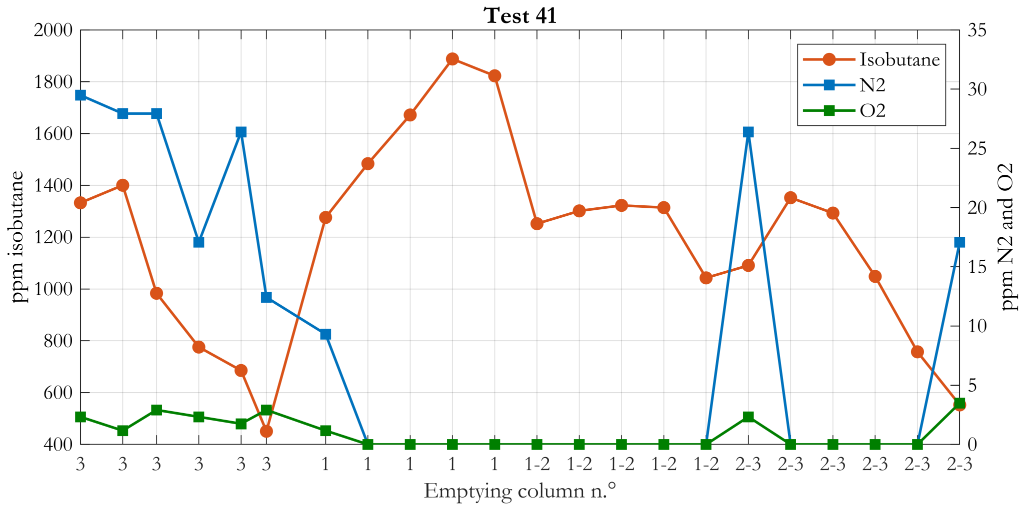

Figure 62: Test 41. Nitrogen, oxygen and isobutane after pump concentrations in time.

Component	**Value**
Average isobutane	1440 ppm
Average nitrogen	9 ppm
Average oxygen	1 ppm
Efficiency	76%

Table 28: Test 41. Isobutane, nitrogen, oxygen average concentrations and efficiency.

8.3.3 Test 42 (-36.2 °C)

Considering the results obtained for tests 38 and 41, an intermediate setpoint temperature of -36.2 °C was set for *Test 42*, in order to optimize the gas quality and recovery.

	C1	**C2**	**C3**
$T_{minx,IN}$ **[°C]**	-28.8	-28.2	-27.8
T_{Btop} **[°C]**	-29.1	-28.0	-27.6
T_{Bbot} **[°C]**	19.5	19.5	19.3
T_{Lauda} **[°C]**	-36.2	-36.2	-36.2
p_{zim} **[mbar]**	10	10	50
Filling flowrate [l/h]	400	400	400
Normalised filling rate [mbar/h]	4.25	4.06	2.37

Table 29: Test 42 operating conditions.

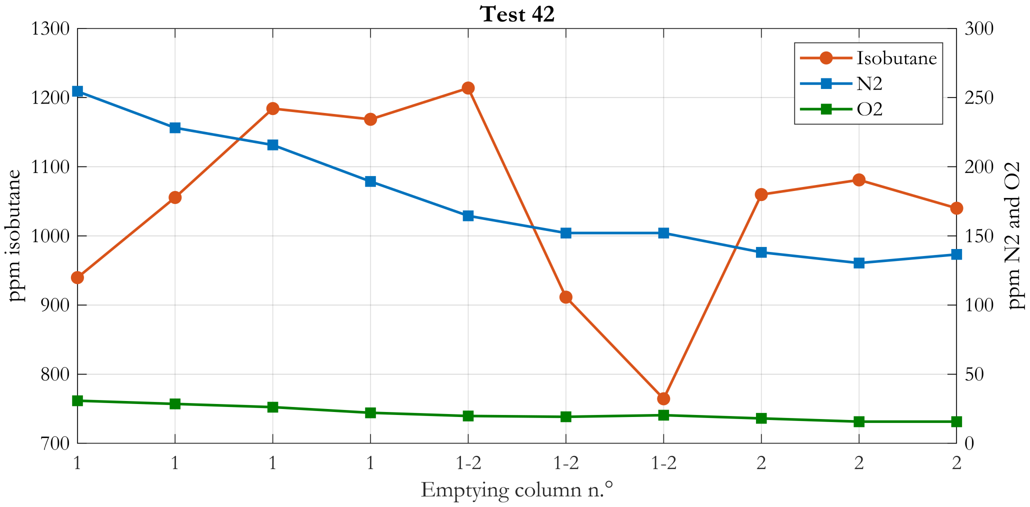

Figure 63: Test 42. Nitrogen, oxygen and isobutane after pump concentrations in time.

Component	**Value**
Average isobutane	1100 ppm
Average nitrogen	157 ppm
Average oxygen	22 ppm
Efficiency	73%

Table 30: Test 42. Isobutane, nitrogen, oxygen average concentrations and efficiency. The average quality is calculated on columns 1 and 2 only. Therefore, the comparison with the other tests (38 and 41) is done only with respect to these two columns.

The high N_2 and O_2 concentrations is a consequence of the undesired air injection to the GC, indeed, a decreasing trend can be observed in Figure 63. Moreover, column 2 guarantees a lower isobutane concentration, and, as for tests 38 and 41, a decreasing trend in C_4H_{10} concentration can be seen during the emptying phase of each column.

8.3.4 Results discussion

The obtained results for tests 38, 41, and 42 lead to define specific trends and issues of the recovery system, in terms of efficiency, gas quality, filling rate and temperature dependence between the four columns.

Efficiency

The efficiency of the recovery system shows an inverse proportionality with the top buffer temperature (Figure 64), and small temperature variations strongly modify the system efficiency. The trend seems to be linear, with a slope of 12 %/°C.

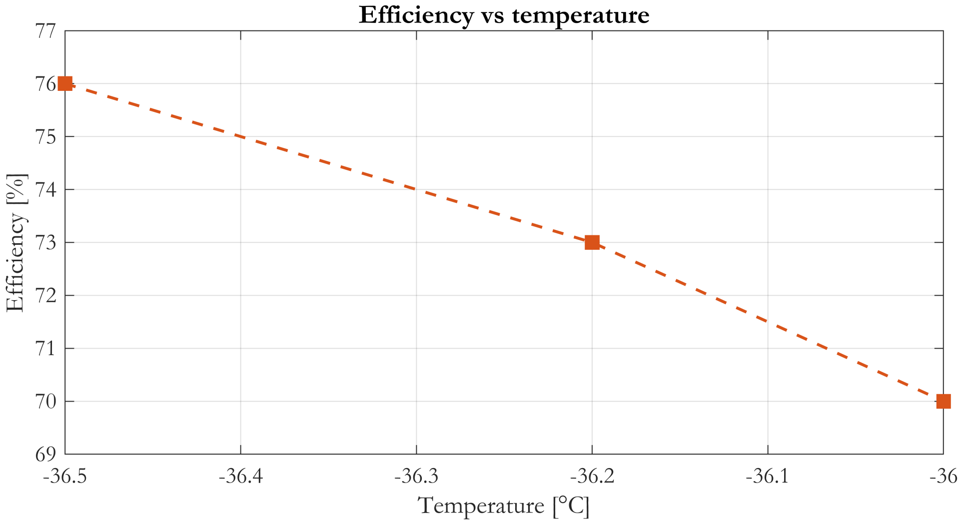

Figure 64: Efficiency trend with top buffer temperature.

Temperature	Efficiency
-36.5 °C	76%
-36.2 °C	73%
-36.0 °C	70%

Table 31: Efficiency values at different T_{Btop}.

At -36 °C also column 3 is negatively affected by the high temperature, with an efficiency lower than 40%. Therefore, under this condition, C3 should be disabled from the system to avoid losing large quantities of gas at the exhaust. However, considering that C4 was already excluded during the tests (due to the extremely low efficiency), with a further exclusion of C3, the system would not be able to run in continuous. Indeed, with two columns only and a filling rate of 400 l/h, C2 would be filled before the complete emptying of C1. If no columns are available for filling the system is automatically stopped. Therefore, considering the low efficiency and the impossibility to run the system with two columns only, an intermediate temperature, between -36.5 °C and -36 °C, was selected as optimal value (-36.2 °C), also considering the gas quality requirements.

Gas quality

Conversely to the efficiency, the gas quality improves with temperature. Indeed, the isobutane concentration of the recovered gas decreases when the Lauda setpoint value is increased from -36.5 °C to -36 °C (Figure 65). The trend seems to be linear, with a slope of 880 ppm/°C, in the tested temperature range with a minimum value at -36 °C. However, considering the low efficiency at -36 °C, a lower temperature value was chosen as optimum (-36.2 °C).

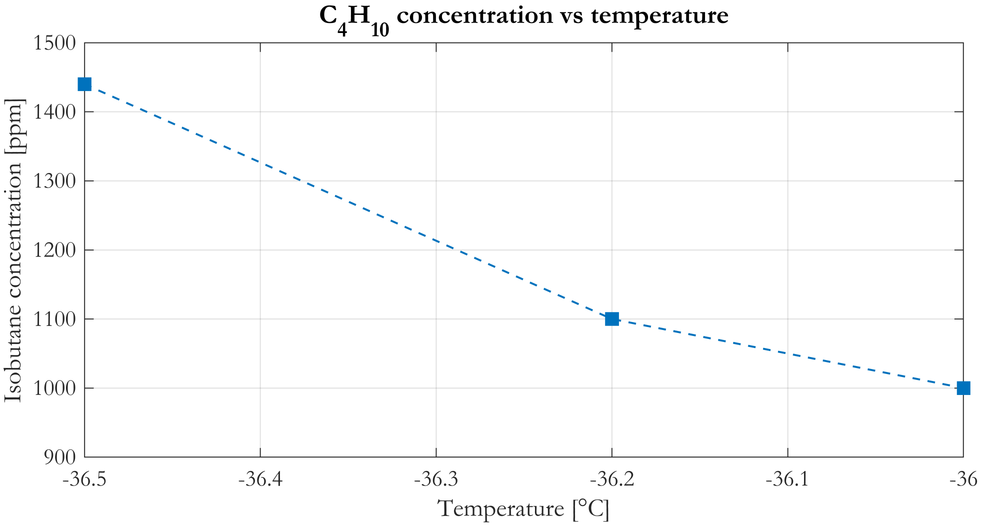

Figure 65: Efficiency trend with top buffer temperature.

Temperature	Isobutane concentration
-36.5 °C	1440 ppm
-36.2 °C	1100 ppm
-36.0 °C	1000 ppm

Table 32: C_4H_{10} at different T_{Btop}.

Filling rate

The last parameter affected by the top buffer temperature is the normalised filling rate, whose theoretical value is derived in chapter 8.1.1. From Figure 66, it decreases by increasing the Lauda setpoint temperature. Moreover, C3 has a lower filling rate than C1 and C2 mainly due to its higher temperature and different dimensions. Indeed, C1 and C2 have a top and bottom buffer heights of 30 mm and 10 mm respectively (3:1 ratio), while C3 has top and bottom buffer heights of 20 mm both (1:1 ratio). Higher temperatures enhance the evaporation, and thus more time is required to completely fill the top buffer. In addition, a 1:1 ratio between buffers (as for C3) means that the bottom buffer has a higher influence on top buffer, with a consequent better heat exchange and higher temperature in B_{top}.

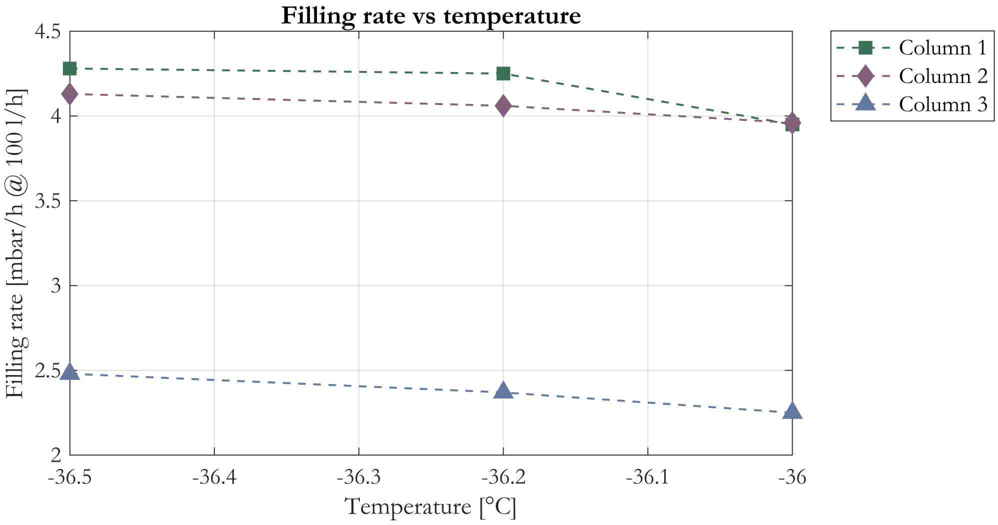

Figure 66: Normalised filling rates for columns 1 (green), 2 (purple), and 3 (blue). A decreasing trend with respect to temperature is present in all three columns, and C3 has lower filling rate (almost a half) than C1 and C2.

Temperature	C1 [mbar/h]	C2 [mbar/h]	C3 [mbar/h]
-36.5 °C	4.28	4.12	2.48
-36.2 °C	4.25	4.06	2.37
-36.0 °C	3.95	3.96	2.25

Table 33: Normalised filling rates for C1, C2, and C3, at different T_{Btop}. All the values are expressed in mbar/h, normalised with a filling rate of 100 l/h.

Temperature interdependence

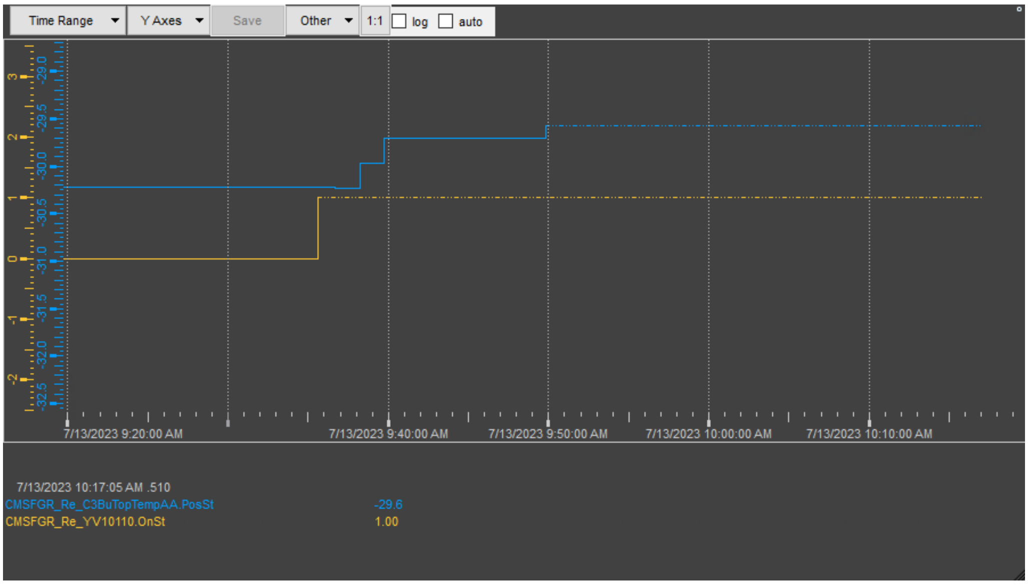

7/13/2023 10:17:05 AM .510
CMSFGR_Re_C3BuTopTempAA.PosSt -29.6
CMSFGR_Re_YV10110.OnSt 1.00

Figure 67: Column 3 top buffer temperature increment (blue) when column 1 starts the filling phase (yellow).

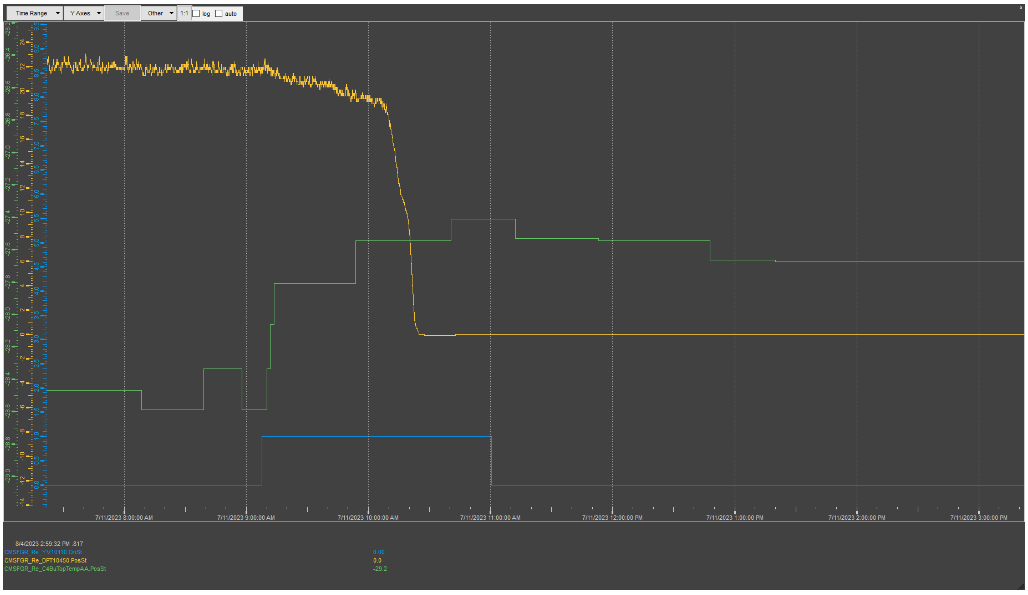

8/4/2023 2:59:32 PM .817
CMSFGR_Re_YV10110.OnSt 0.00
CMSFGR_Re_DPT10450.PosSt 0.0
CMSFGR_Re_C4BuTopTempAA.PosSt -29.2

Figure 68: Test 38. During the filling phase of C1 (blue curve ON), the temperature of C4 (green) increases by almost 1.5 °C, inducing a reduction of DPT (yellow) down to zero. Top buffer temperature is too high (close to the R134a boiling temperature) and all the mixture evaporates.

Tests on C1, C2, and C3 highlight an interdependence between the top buffer temperatures of the three columns, since the cooling circuit is connected in series and not in parallel. Therefore, while C1 is filling (yellow line in mode ON), a temperature increment (blue line) can be observed in the other columns, especially for C3 (Figure 67). Indeed, the thermal fluid (Kryo65) absorbs heat in the C1 heat exchanger during the filling phase, increasing its temperature and therefore, C3 top buffer temperature rises. This trend represents an issue especially for C4, which is the last and warmest column in the cooling circuit. During the filling phases of the other three columns, the liquid mixture in the C4 top buffer completely evaporates due to the high temperature (close to the R134a boiling temperature, -26.4 °C) (Figure 68). Therefore, considering a Lauda setpoint of -36.2°C and a cooling circuit in series, column 4 should be deactivated to avoid losing gas and decreasing the overall system efficiency.

Non-efficient heat dissipation

The thermostat installed in the system is the Lauda Integral XT 280 (Figure 69a) with the specifications reported in Table 34.

Physical quantity	**Value**
Operating temperature range [°C]	-80/220
Minimum filling volume [L]*	5
Additional filling volume [L]**	6.7
Cooling refrigerant unit	air
Cooling air temperature without performance loss [°C]	10/20

Table 34: Lauda Integral XT 280 working parameters. *Minimum volume of Kryo 65 which must be poured in the expansion vessel to avoid low level alarm. **Volume of Kryo 65 added to the minimum value to increase the level indication. The cooling unit has 15 levels, and each level corresponds to 0.45 L of refrigerant [44].

(a) Lauda front view. **(b)** Huber front view.

Figure 69: Cooling units available for the recovery system.

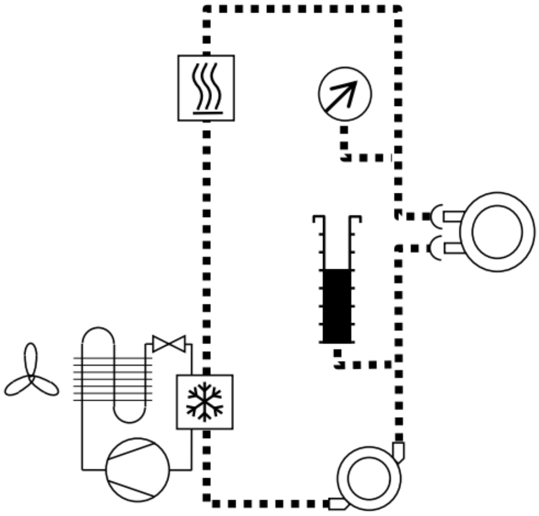

Figure 70: Lauda Integral XT 280 operating scheme. The cooling unit has an operating circuit (filled by Kryo 65) with an outflow and return connection for the external load, and a "cooling" circuit with R-404a and R-23 as refrigerants. The "cooling" circuit works with an inverse Rankine cycle: the evaporator absorbs heat from the Kryo 65, while the condenser releases heat to the external environment. Therefore, if the ambient temperature is too high (> 20 °C), the Lauda decreases its performances and cannot maintain the setpoint temperature.

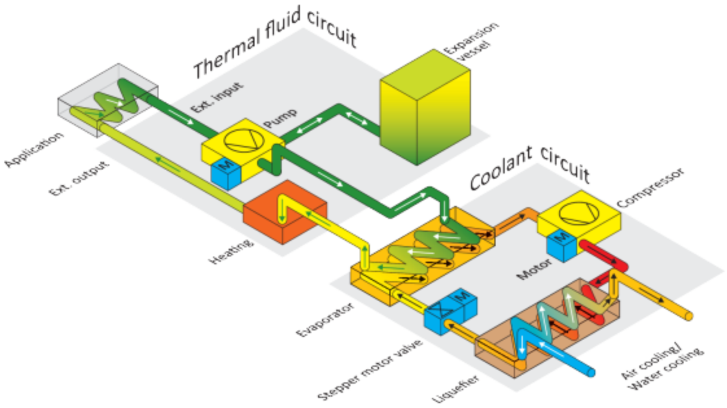

Figure 71: Huber Unistat 910w operational scheme. The thermal fluid circuit is filled by Kryo 65 (as for the Lauda Integral XT 280), with the output and input pipes connected to the external application. The cooling circuit is composed by an evaporator which absorbs heat from the thermal fluid circuit and a condenser/liquefier which releases heat to an external water-cooling circuit.

The air-cooled thermostat has a non-negligible issue in dissipating heat with the external environment. Indeed, the condenser (Figure 70) requires an air temperature between 10 °C and 20 °C, but these values are difficult to maintain in the gas room, especially during hot days (as the 10th July, when test 38 was performed).
The problem of the non-efficient heat dissipation may be solved by substituting the air-cooled thermostat with a water-cooled one, as the Huber Unistat 910w (Figure 69b). The operating scheme is similar to the Lauda Integral XT 280, with the

condenser dissipating heat to an external water circuit (Figure 71). Useful technical data are reported in Table 35.

Physical quantity	**Value**
Operating temperature range [°C]	-90/250
Cooling refrigerant unit	water
Cooling air temperature without performance loss [°C]	5/40

Table 35: Huber Unistat 910w working parameters [45].

Series and parallel cooling circuit

A second solution to face the problem of temperature increment between columns 1 and 4 (almost 1 °C step per column) might be a modification of the cooling circuit from a series to a parallel connection. Under this condition, each column would be independent from the others, minimising the temperature difference between the first and the last one. The new system configuration is shown in Appendix A.

8.4 Top buffer pressure

The top buffer pressure can be regulated manually by the Zimmerli reduction valve equipped on each column. The Zimmerli is a spring-loaded differential pressure regulator with reference to actual atmospheric pressure via a sensor hole. Under operating conditions, gas enters from the primary side and through a valve reaches the counter side of the diaphragm through a Venturi tube. As a result, the differential pressure is in balance with the force of the adjustable spring. The valve is closed as soon as the secondary pressure raises the setpoint, and it is open if the secondary pressure is below the set point (Figure 72) [46].

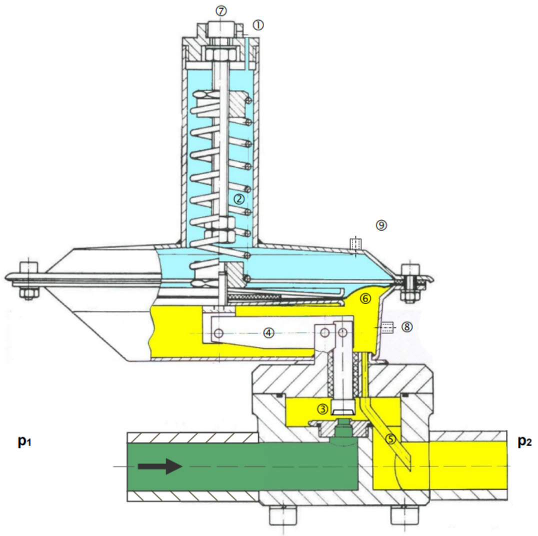

Figure 72: Zimmerli front section plane. p1 is the primary line, p2 the secondary side. The spring (2) is regulated through a screw (7) whose position defines the setpoint at which the valve (3) opens. The valve is connected to the spring through a lever (4). Venturi tube (5), atmospheric sensor hole (1), optional pulse line (8), and optional pilot line (9).

8.4.1 Column 3 analysis

Concerning the top buffer pressure of column 3 (column 4 was disabled due to its low efficiency), three operating conditions have been analysed: 20 mbar, 35 mbar, and 50 mbar, with the results reported in figures 73 and 74. Columns 1 and 2 top pressures were set at 10 mbar without further changes, in order to compensate for the low temperatures in the top buffers and enhance the separation process. Indeed, a lower pressure opposes less resistance to the gas exiting the top buffer through the exhaust, improving the distillation, but losing more gas.

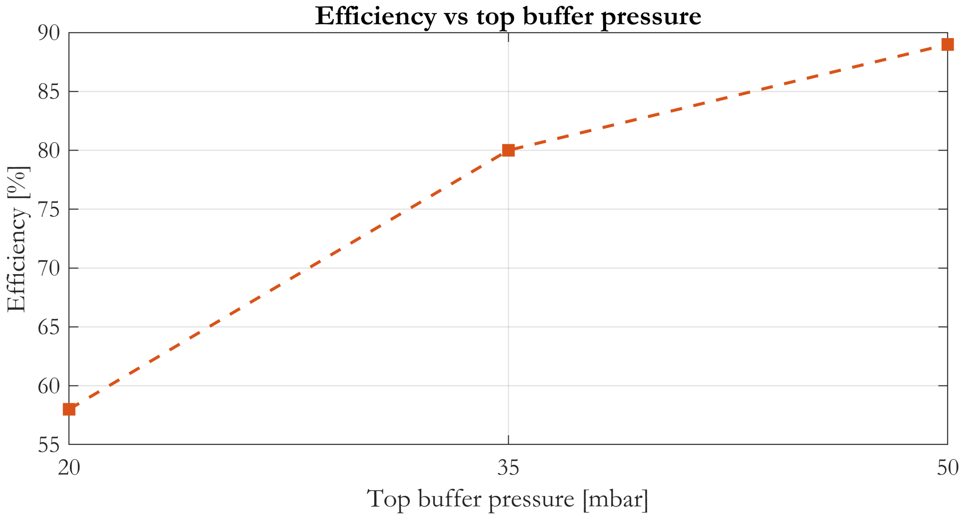

Figure 73: Efficiency trend with respect to top buffer pressure. The trend is not linear, but the efficiency increases with pressure, as expected. In fact, the higher the pressure of the Zimmerli the lower the gas quantity lost through the exhaust.

Top buffer pressure	**Efficiency**
20 mbar	58%
35 mbar	80%
50 mbar	89%

Table 36: Efficiency values at different p_{zim}.

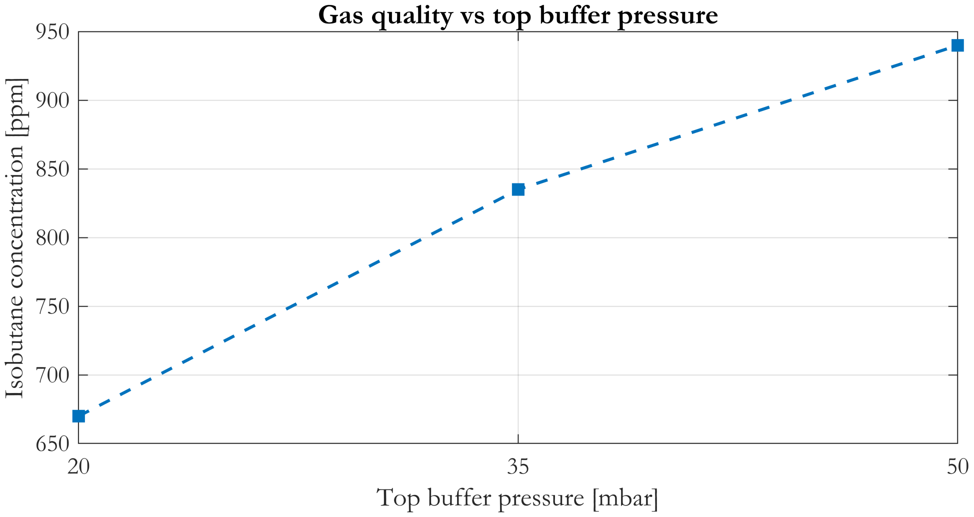

Figure 74: Isobutane concentration with respect to top buffer pressure. The trend seems to be linear, with an increasing C_4H_{10} with pressure. Indeed, with a higher pressure of the Zimmerli the separation process is less effective since a lower fraction of gas with impurities leaves the column.

Top buffer pressure	**Isobutane concentration**
20 mbar	670 ppm
35 mbar	835 ppm
50 mbar	940 ppm

Table 37: C_4H_{10} concentrations at different p_{zim}.

8.4.2 Pressure interdependence

Each column is characterised by three pressure values, measured by a top and bottom pressure transmitters (PT-10x31 and PT-10x32) and a differential pressure transmitter (DPT-10x50). Top and bottom pressures influence each other, and the top buffer liquid level, measured by the DPT-10x50, has an influence on the bottom pressure.

For instance, in Test 41, increasing the pressure of the Zimmerli (from 20 mbar of test 38 to 50 mbar), also the pressure of the bottom buffer increases, meaning that the two are communicating. This pressure increment is not due to a temperature increase, but it is a consequence of the top buffer pressure increment (Figure 75).

Finally, it is worth to notice that the top buffer pressure represents a distillation indicator, since, as soon as gas is formed and its pressure reaches the Zimmerli set value, the distilled vapour phase leaves the system through the exhaust line. Therefore, whenever PT-10x31 indicates a pressure value equal to the setpoint, the separation process occurs, and it may happen both during the filling and emptying phases.

7/13/2023 9:14:35 AM .285
CMSFGR_Re_PT10331.PosSt 0.050
CMSFGR_Re_PT10332.PosSt 0.089

Figure 75: Pressure dependence between the two buffers. Setting the top buffer pressure (blue) to 50 mbar, the bottom buffer pressure (yellow) increases consequently, due to their communication with the connecting pipe.

8.4.3 Effect of the emptying phase on P_{top} and P_{bot}

During the emptying phase, top and bottom pressures show peculiar trends. Indeed, as soon as the compressor is activated, the system is perturbed and a transient phase can be seen with both P_{top} and P_{bot}[3] decreasing, almost down to zero, before increasing again. P_{top} reaches its set value, meaning that distillation occurs, while P_{bot} follows the DPT trend, decreasing with the top buffer liquid level. These trends are similar for all columns, and C1 behaviour is shown in Figure 76.

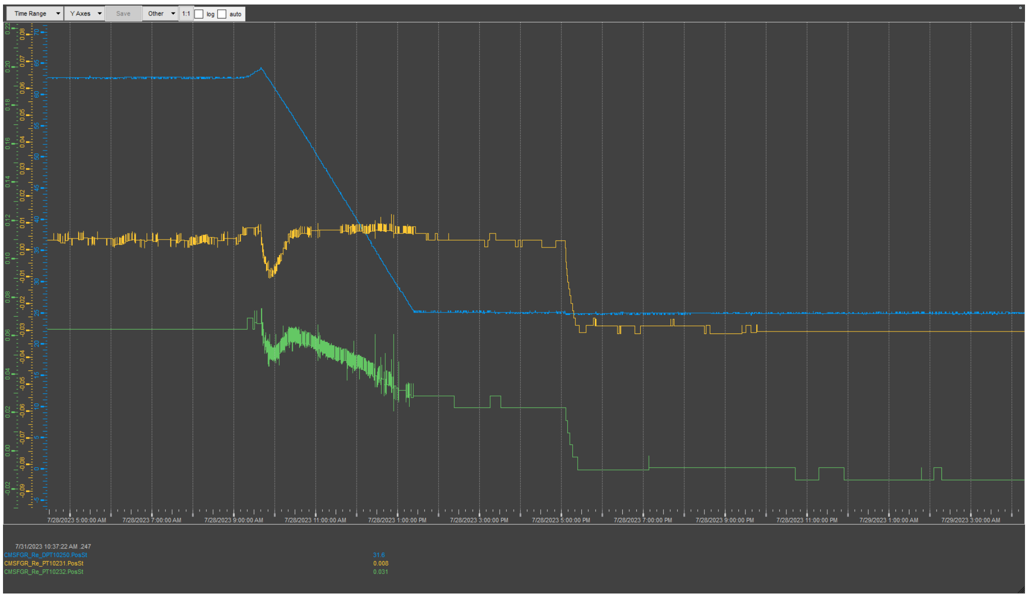

Figure 76: Column 1 pressure trends during the emptying phase. During the emptying phase, the liquid level (blue) starts decreasing, the yellow (P_{top}) and green (P_{bot}) curves have a minimum due to the perturbation for the compressor activation. After a transient phase, P_{top} reaches the Zimmerli setpoint and P_{bot} decreases with a similar trend of the DPT (blue).

---

[3] P_{top} is defined as the top buffer pressure, and P_{bot} as the bottom buffer pressure.

8.4.4 Differential pressure and liquid level evaluation

The differential pressure, measured by the DPT-10x50, is used for estimating the liquid level in the top buffers between the two liquid level sensors (LSH-10x60 and LSH-10x61). The differential pressure combined with the Stevin's law is used for the evaluation of the liquid level.

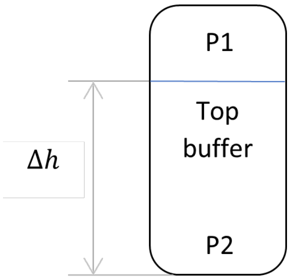

Figure 77: Top buffer scheme for the liquid level (Δh) evaluation.

Stevin's law is derived from Figure 77, as follows:

$$p_2 = p_1 + \rho g \Delta h \tag{26}$$

$$\Delta h = \frac{p_2 - p_1}{\rho g} = \frac{DPT}{\rho g} \tag{27}$$

Where ρ is the density of the liquid mixture injected in the top buffer, approximated to the R134a density, considering that the mixture is composed by 95.2% of R134a, and g the gravitational acceleration.

Each column has a correspondent DPT value for the empty and full states. The empty state is defined when the liquid level is equal to the LSH-10x61, while the full state is achieved with the activation of the LSH-10x60. Table 38 shows the empty and full states DPT values for each column.

	C1	**C2**	**C3**	**C4**
Empty state DPT [mbar]	20	25	18	20
Full state DPT [mbar]	59	63	44	44

Table 38: Empty and full states DPT values for each column.

8.5 Bottom buffer temperature

The second temperature variable affecting the system performances is the bottom buffer temperature, controlled by the Huber Ministat 125. The system was tested in automatic mode, under four different temperature values: 14, 17, 20, and 23 °C. As for the previous tests, column 4 was disabled due to its low efficiency and the filling rate was set to 150 l/h due to the off status of the RPCs (during the run, the flowrate may rise to 400 l/h).
In addition, the aim of tests 53 to 61 was the understating of the system behaviour in continuous mode, 24 hours per day.

8.5.1 Tests 53 and 58 (23 °C)

Columns 1, 2, and 3 have been tested with a setpoint temperature of 23 °C under the conditions listed in Table 39.

	C1	**C2**	**C3**
$T_{minx,IN}$ [°C]	-28.8	-28.2	-27.8
T_{Btop} [°C]	-28.9	-28.5	-27.6
T_{Bbot} [°C]	22.6	22.2	22.7
T_{Lauda} [°C]	-36.2	-36.2	-36.2
p_{zim} [mbar]	10	10	35
Filling flowrate [l/h]	150	150	150
Normalised filling rate [mbar/h]	4.52	4.32	2.70

Table 39: Tests 53 and 58 operating conditions.

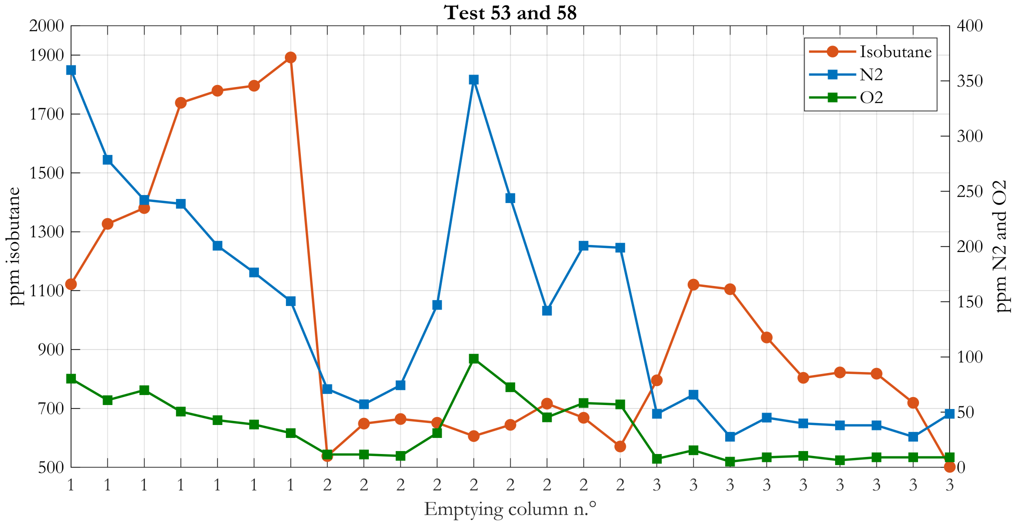

Figure 78: Tests 53 and 58. Nitrogen, oxygen and isobutane after pump concentrations in time.

Component	**Value**
Average isobutane	970 ppm
Average nitrogen	140 ppm
Average oxygen	34 ppm
Efficiency	83%

Table 40: Tests 53 and 58. Isobutane, nitrogen, oxygen average concentrations and efficiency.

According to Figure 78, the isobutane concentration in column 2 is lower with respect to columns 1 and 3 while theoretically it should be higher considering that it is colder than C3. The worst gas quality is obtained from column 1 due to its low temperature compared to C2 and C3, and the isobutane concentration increases during the C1 emptying. In addition, as seen from the previous tests, the C_4H_{10} concentration decreases at the end of the emptying phase. Finally, concerning the air concentration, despite a peak reached during C2 emptying, it shows a decreasing trend, with an average N_2 of 140 ppm and O_2 of 34 ppm.

8.5.2 Tests 55 and 56 (20 °C)

During Tests 55 and 56, the Huber setpoint temperature is maintained at 20 °C, under the conditions reported in Table 41.
The isobutane trend is similar to tests 53 and 58, with a minimum reached during the C2 emptying phase and a decreasing slope at the end of C3 emptying, for an average value of 715 ppm. This similarity may suggest that the system has reached a steady state mode, and independently from the conditions applied, it always shows the same trend. Indeed, from test 53 of 31st July, the system started operating in automatic mode in continuous for 24 hours per day.

	C1	**C2**	**C3**
$T_{minx,IN}$ [°C]	-28.8	-28.2	-27.8
T_{Btop} [°C]	-28.9	-28.5	-27.6
T_{Bbot} [°C]	19.4	19.4	19.0
T_{Lauda} [°C]	-36.2	-36.2	-36.2
p_{zim} [mbar]	10	10	35
Filling flowrate [l/h]	150	150	150
Normalised filling rate [mbar/h]	4.54	4.12	2.70

Table 41: Tests 55 and 56 operating conditions.

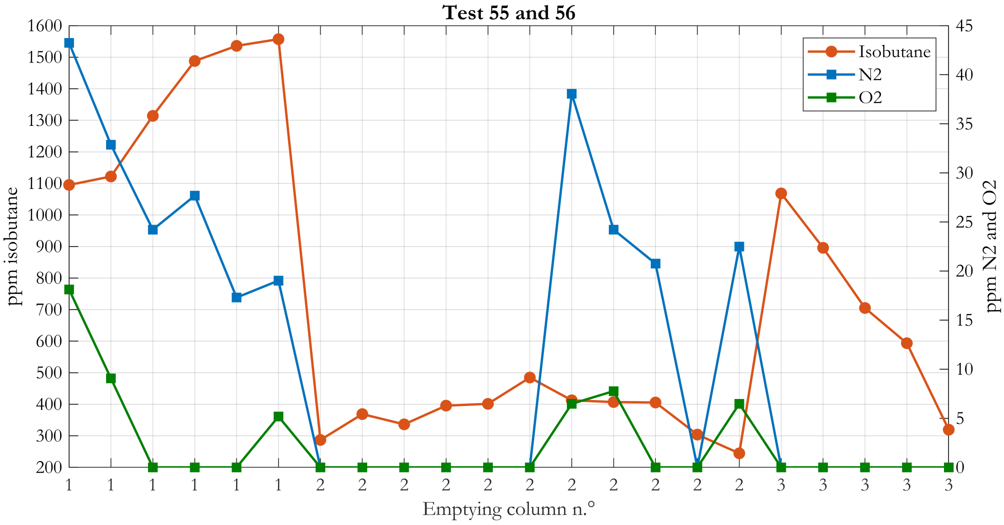

Figure 79: Tests 55 and 56. Nitrogen, oxygen and isobutane after pump concentrations in time.

Component	Value
Average isobutane	715 ppm
Average nitrogen	12 ppm
Average oxygen	2 ppm
Efficiency	87%

Table 42: Tests 55 and 56. Isobutane, nitrogen, oxygen average concentrations and efficiency.

8.5.3 Tests 54 and 57 (17 °C)

Tests 54 and 57 aim to describe the system performances with a Huber setpoint temperature of 17 °C. The tests conditions are reported in Table 43.
As already mentioned in chapter 8.5.2, the system has reached a steady state operational mode, thus, the isobutane concentration shows the same trend of the previous tests, with an average value of 652 ppm. Molecular oxygen and nitrogen concentrations show a significant increase during the C2 emptying, while for C1 and C3 are negligible. This unexpected behaviour may be associated with the presence of air in the gas chromatograph during the analyses of column 2. Moreover, the three columns were emptied in different days: C2 was analysed in test 57 (8^{th} August), while C1 and C3 in test 54 (1^{st} August).

	C1	C2	C3
$T_{minx,IN}$ [°C]	-28.8	-28.2	-27.8
T_{Btop} [°C]	-29.0	-28.5	-27.7
T_{Bbot} [°C]	16.5	16.4	16.6
T_{Lauda} [°C]	-36.2	-36.2	-36.2
p_{zim} [mbar]	10	10	35
Filling flowrate [l/h]	150	150	150
Normalised filling rate [mbar/h]	4.62	4.24	2.38

Table 43: Tests 54 and 57 operating conditions.

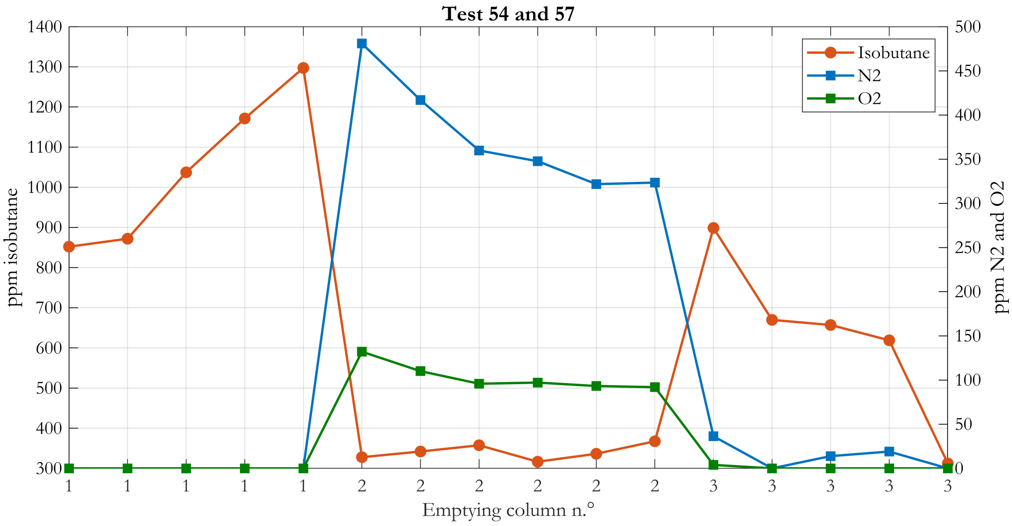

Figure 80: Tests 54 and 57. Nitrogen, oxygen and isobutane after pump concentrations in time.

Component	Value
Average isobutane	652 ppm
Average nitrogen	145 ppm
Average oxygen	39 ppm
Efficiency	83%

Table 44: Tests 54 and 57. Isobutane, nitrogen, oxygen average concentrations and efficiency.

8.5.4 Tests 59, 60, and 61 (14 °C)

During tests 59, 60, and 61, columns 1, 2, and 3 were analysed setting the Huber temperature at 14 °C. Tests conditions are reported in Table 45.
The isobutane concentration follows the same trend of the previous tests, with an average value of 1100 ppm. The most significant contribution is given by column 1, which reaches values close to 3500 ppm, increasing considerably the C_4H_{10} concentration (Figure 81).

	C1	**C2**	**C3**
$T_{minx,IN}$ **[°C]**	-28.8	-28.2	-27.5
T_{Btop} **[°C]**	-28.9	-28.6	-27.9
T_{Bbot} **[°C]**	14.0	13.6	13.8
T_{Lauda} **[°C]**	-36.2	-36.2	-36.2
p_{zim} **[mbar]**	10	10	35
Filling flowrate [l/h]	150	150	150
Normalised filling rate [mbar/h]	4.54	4.12	2.70

Table 45: Tests 59, 60 and 61 operating conditions.

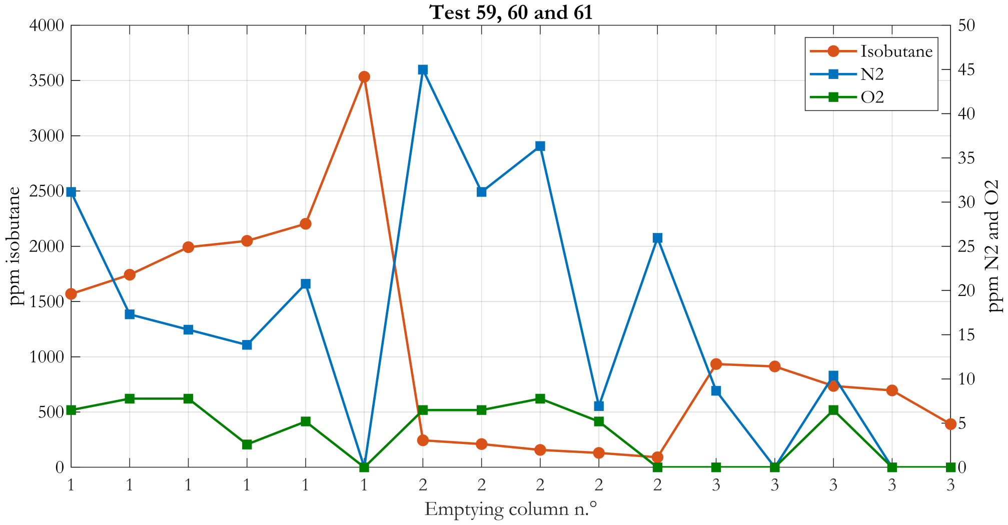

Figure 81: Tests 59, 60 and 61. Nitrogen, oxygen and isobutane after pump concentrations in time.

Component	Value
Average isobutane	1100 ppm
Average nitrogen	16 ppm
Average oxygen	4 ppm
Efficiency	81%

Table 46: Tests 59, 60 and 61. Isobutane, nitrogen, oxygen average concentrations and efficiency.

8.5.5 Results discussion - efficiency and gas quality in time

From tests 53 to 61 it can be noticed that the bottom buffer temperature influences both the recovered gas quality and the system efficiency.
Top and bottom buffers communicate through a 10 mm diameter pipe and the heat exchange occur in the top buffer between the vapour phase, rising from the bottom buffer and the liquid phase exiting the heat exchanger. Theoretically, the higher the bottom buffer temperature, the higher the temperature of the vapor phase, and the larger the heat transferred to the top buffer liquid, and thus, a larger amount of vapor exits the top buffer through the exhaust line. Therefore, a higher T_{Bbot} leads to better gas qualities but worse efficiencies.
The efficiency was evaluated on a daily basis, while the gas quality is the results of the after pump analysis with the gas chromatograph.

The **efficiency** (ϵ) was calculated over 24 hours between two following days, considering the mass gained in the recovery bottle (Δm), the total gas recovered from the system (ϵG_{in}), and the total gas injected to the RPC mixer (G_{mix}). Moreover, a fraction of gas is always lost through the exhaust line of the gas chromatograph during the analyses (G_{GC}). Equation 28 represents the mass balance on the recovery bottle for the efficiency evaluation.

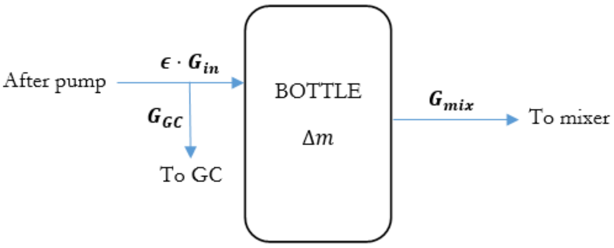

Figure 82: Mass balance on the recovery bottle.

$$\epsilon G_{in}\Delta t_{in} - G_{GC}\Delta t_{GC} - G_{mix}\Delta t_{mix} = \Delta m \tag{28}$$

$$\epsilon = \frac{\Delta m + G_{GC}\Delta t_{GC} + G_{mix}\Delta t_{mix}}{G_{in}\Delta t_{in}} \tag{29}$$

Where Δt_{in} is the time of gas injection in the recovery bottle (= 24 h), Δt_{GC} is the time required for the gas analyses (variable, it depends on the type of analyses), and Δt_{mix} is the amount of hours for the gas injection at the RPCs mixer (= 24 h).

Figure 83 and Figure 84 show the system behaviour in continuous mode in terms of efficiency and gas quality, which are plotted with respect to the operating days, from the 31st July and the 10th August. All the working conditions, except for the bottom buffer temperature, are unchanged during the entire period (Table 47).

	C1	**C2**	**C3**
T_{Lauda} **[°C]**	-36.2	-36.2	-36.2
p_{zim} **[mbar]**	10	10	35
Filling flowrate [l/h]	150	150	150

Table 47: Operating conditions between the 31st July and the 10th August.

Days	T_{Bbot}	**Efficiency [%]**	C_4H_{10} **[ppm]**	N_2 **[ppm]**	O_2 **[ppm]**
31/07-01/08	23	90	950	150	35
01/08-02/08	17	82	650	140	40
02/08-03/08	20	93	680	12	2
03/08-04/08	29	87	680	12	2
04/08-05/08	17	83	650	140	40
05/08-06/08	23	83	950	150	35
31/07-01/08	14	78	1100	16	4
31/07-01/08	14	81	1100	16	4

Table 48: Daily efficiency and gas quality values between the 31st July and the 10th August.

From Figure 83, it is clear that the system efficiency oscillates between 80% and 90%, with an average value of 84%. A peak of 93% is achieved between the 2nd and 3rd August, when the system was operating with a bottom setpoint temperature of 20 °C. On the other hand, a minimum of 78% is reached with a temperature of 14 °C between the 8th and 9th August. The real trend seems not consistent with the theoretical expected one, since the efficiency increases with the bottom temperature instead of decreasing. Moreover, the same value of 83% is obtained with temperatures of 17 °C and 23 °C, meaning that it is not possible to define a clear efficiency trend.

The daily efficiency depends on the columns that are emptied during the 24 hours. Indeed, each column has its own efficiency, which decreases from C1 to C3. On average, C1 has an efficiency of 90%, C2 of 85%, and C3 of 70% according to the temperature increase between the columns. The average efficiency over the three columns is 82%, which is close to the 84% achieved during the tests in continuous

mode, from the 31st July and 10th August.
In addition, the non-clear efficiency trend may suggest that the bottom buffers are not significantly influencing the system performances. Indeed, especially for columns 1 and 2, the bottom buffers are too small compared to the top ones (height ratio 3:1) and even if the T_{Bbot} is modified, the results obtained are not consistent with the expected values. A possible solution might be the substitution of the 10 cm buffers, of columns 1 and 2, with 20 cm buffers to obtain an height ratio of 3:2, knowing that C3 has a ratio of 1:1.

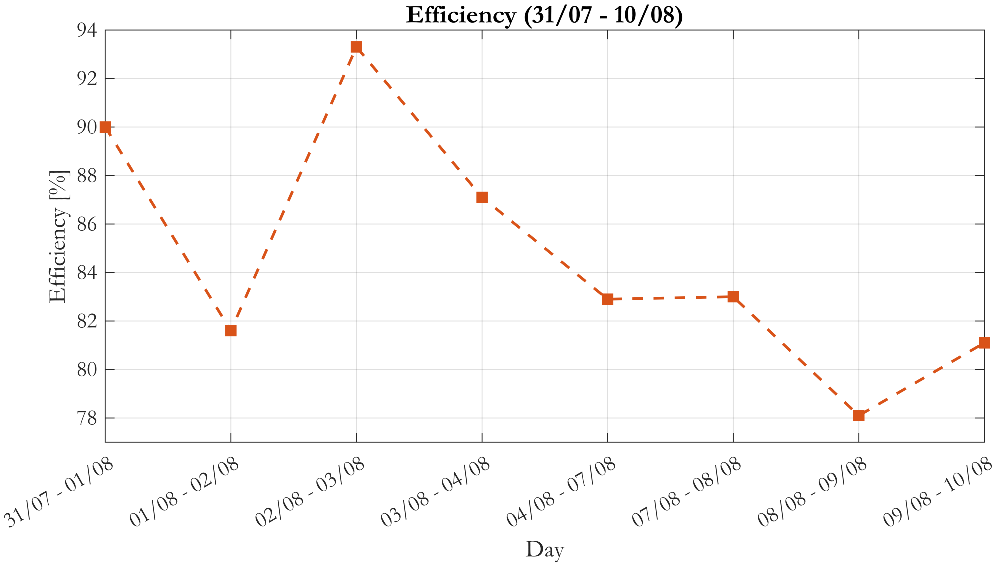

Figure 83: Daily efficiency trend between the 31st July and the 10th August.

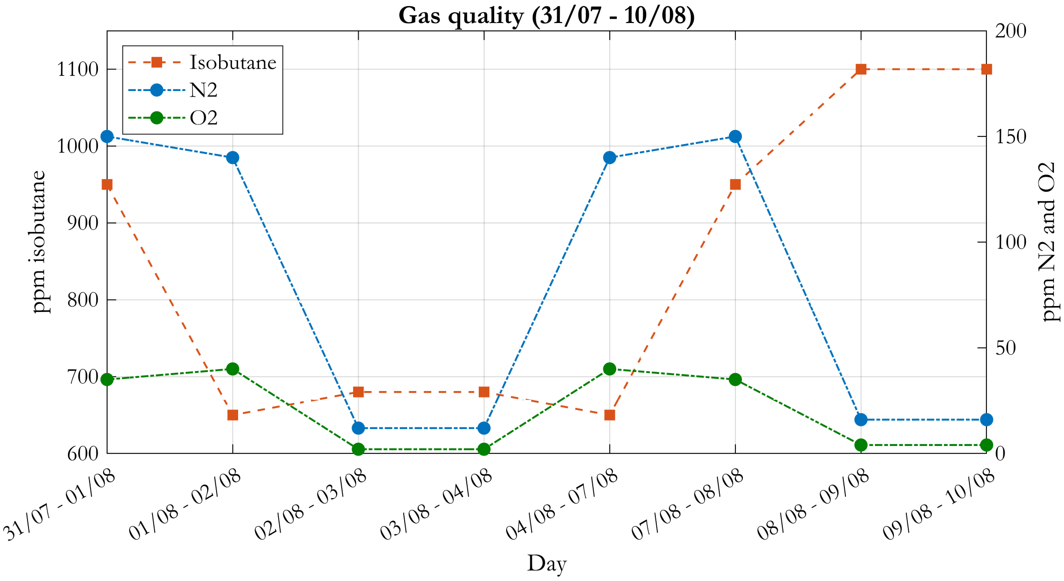

Figure 84: Gas quality trend between the 31st July and the 10th August.

Concerning the gas quality (Figure 84), the highest isobutane concentration (1100 ppm) was obtained with a bottom setpoint temperature of 14 °C as expected.

However, at higher temperatures, an unclear trend is present, with the lowest value achieved at 17 °C (650 ppm), a similar value (680 ppm) obtained at 20 °C, and a higher one (950 ppm) reached at 23 °C. This behaviour may be the result of the undersized bottom buffers, which do not influence significantly the recovered gas quality, whose values are mostly influenced by other parameter as extraction rate, top buffer temperature and pressure. The N_2 and O_2 concentrations are acceptable since they never increase above 150 ppm and 40 ppm respectively.

8.6 Distillation time

The last parameter tested for the system was the distillation time, which is defined as the period between the end of filling and the beginning of emptying phases. Three values were tested: no distillation (0 min), 30 min, and 60 min. Theoretically, under the optimal condition of bottom temperature, top temperature and pressure, extraction rate, the higher the distillation time, the better the gas quality. Tests 34, 35, and 36 involved all the four columns.

8.6.1 Test 34 (no distillation)

During *Test 34*, the mixture does not wait any time in the top buffer, and the extraction phase starts immediately after the filling ending. Test conditions are reported in Table 50

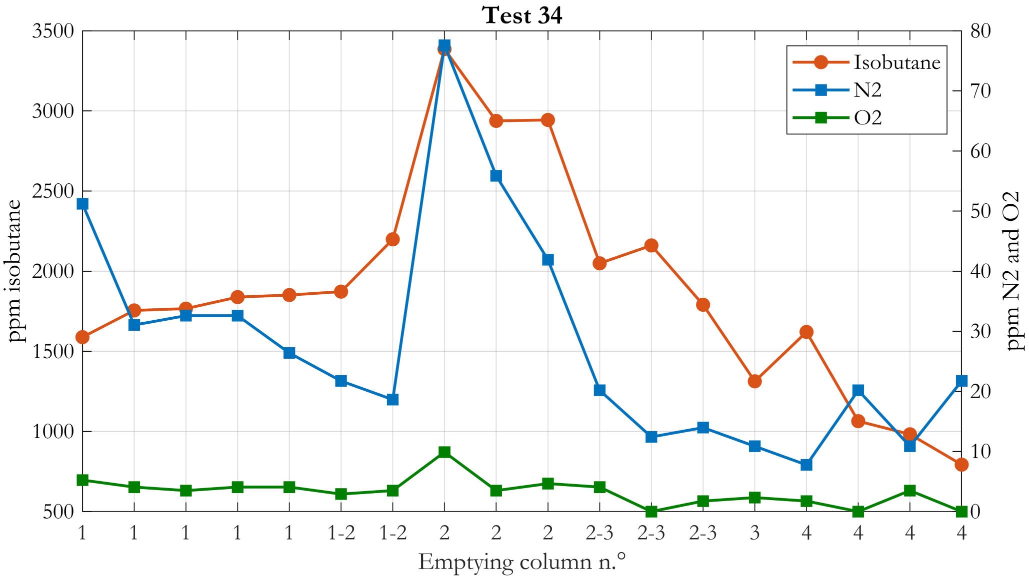

Figure 85: Test 34. Nitrogen, oxygen and isobutane after pump concentrations in time.

Component	Value
Average isobutane	1880 ppm
Average nitrogen	28 ppm
Average oxygen	3 ppm
Efficiency	72%

Table 49: Tests 34. Isobutane, nitrogen, oxygen average concentrations and efficiency.

From Figure 85 it can be seen that the largest contribution to the high isobutane concentration is given by column 2, which reaches almost 3400 ppm before decreasing with the introduction of C3. With C4 it reduces below 1000 ppm as a consequence of the higher column temperature.

	C1	**C2**	**C3**	**C4**
$T_{minx,IN}$ **[°C]**	-28.8	-28.2	-27.8	-27.1
T_{Btop} **[°C]**	-30.9	-29.1	-28.7	-28.2
T_{Bbot} **[°C]**	19.8	19.6	19.5	19.0
T_{Lauda} **[°C]**	-36.5	-36.5	-36.5	-36.5
p_{zim} **[mbar]**	10	10	20	20
Filling flowrate [l/h]	400	400	400	400
Normalised filling rate [mbar/h]	4.32	4.10	2.62	2.47
Extraction flowrate [l/h]	600	600	600	600

Table 50: Test 34 operating conditions.

8.6.2 Test 35 (30 minutes)

During *Test 35*, each column, after the filling phase, had 30 minutes for the distillation process, before starting the emptying phase.

	C1	**C2**	**C3**	**C4**
$T_{minx,IN}$ **[°C]**	-28.8	-28.2	-27.8	-27.1
T_{Btop} **[°C]**	-30.9	-29.0	-28.9	-28.2
T_{Bbot} **[°C]**	19.6	19.6	19.4	19.0
T_{Lauda} **[°C]**	-36.5	-36.5	-36.5	-36.5
p_{zim} **[mbar]**	10	10	20	20
Filling flowrate [l/h]	400	400	400	400
Normalised filling rate [mbar/h]	4.28	4.24	2.58	2.31
Extraction flowrate [l/h]	600	600	600	600

Table 51: Test 35 operating conditions.

Similar to test 34, the peak in the isobutane concentration is achieved during the C2 emptying, while a decrease is observed after the introduction of column 3 (Figure 86). Both nitrogen and oxygen concentration are acceptable with average values of 25 ppm and 2 ppm respectively. However, the system has an efficiency of 62%, lower than test 34 (with no distillation), due to the larger amount of gas leaving the columns during the distillation. Indeed, especially C4, which is the hottest column, lose too much gas mixture from the top buffer due to the high temperature (the gas output at the heat exchanger is at -27.1 °C, which is close to the pure R134a boiling temperature of -26.4 °C).

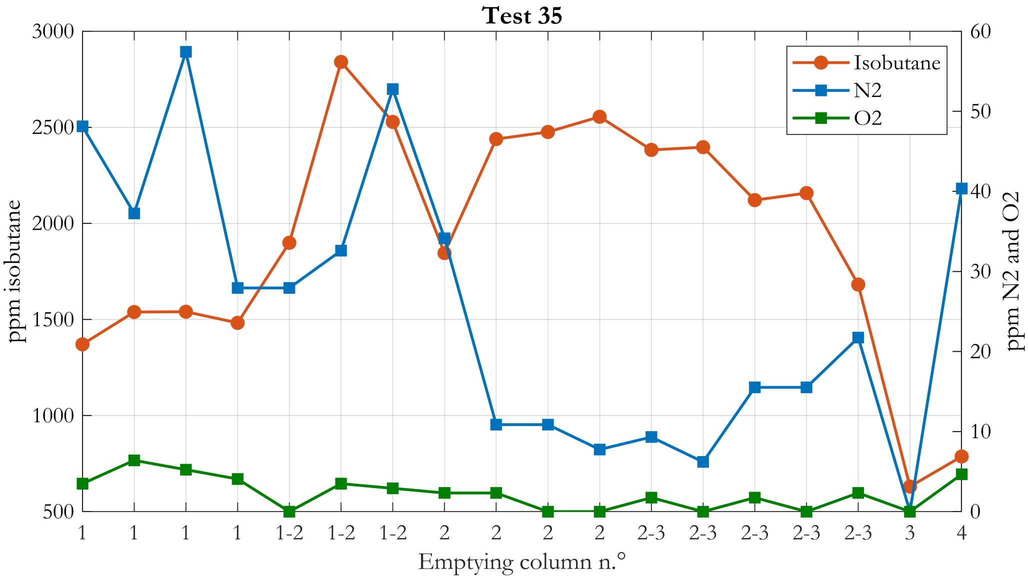

Figure 86: Test 35. Nitrogen, oxygen and isobutane after pump concentrations in time.

Component	Value
Average isobutane	1920 ppm
Average nitrogen	25 ppm
Average oxygen	2 ppm
Efficiency	62%

Table 52: Tests 35. Isobutane, nitrogen, oxygen average concentrations and efficiency.

8.6.3 Test 36 (60 minutes)

Test 36 is performed with a distillation time of 1 hour, under the operating conditions listed in Table 53.

As for tests 34 and 35, the isobutane concentration increases during the C2 emptying and decreases when C3 and C4 are in extraction mode (Figure 87), with an average value of 1250 ppm, while both nitrogen and oxygen have negligible concentrations. As explained in chapter 8.6.2, due to the 60 minutes distillation, the system has a low efficiency, of 55%, because a large amount of gas is lost at the exhaust, especially in column 4.

	C1	C2	C3	C4
$T_{minx,IN}$ [°C]	-28.8	-28.2	-27.8	-27.1
T_{Btop} [°C]	-30.7	-29.0	-28.7	-28.4
T_{Bbot} [°C]	19.8	19.6	19.4	19.0
T_{Lauda} [°C]	-36.5	-36.5	-36.5	-36.5
p_{zim} [mbar]	10	10	20	20
Filling flowrate [l/h]	400	400	400	400
Normalised filling rate [mbar/h]	4.31	4.20	2.60	2.17
Extraction flowrate [l/h]	600	600	600	600

Table 53: Test 36 operating conditions.

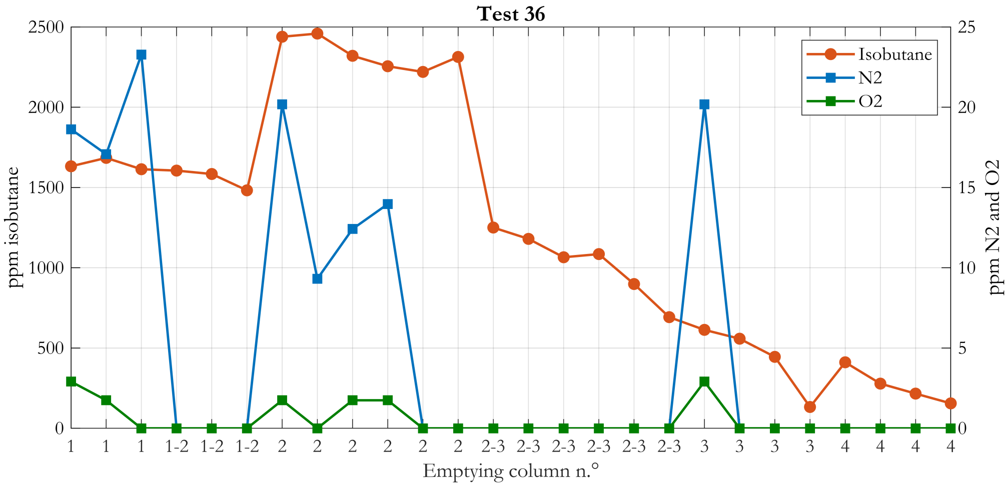

Figure 87: Test 36. Nitrogen, oxygen and isobutane after pump concentrations in time.

Component	Value
Average isobutane	1250 ppm
Average nitrogen	5 ppm
Average oxygen	1 ppm
Efficiency	55%

Table 54: Tests 36. Isobutane, nitrogen, oxygen average concentrations and efficiency.

8.6.4 Results discussion

The results from tests 34, 35, and 36 can be summarised in efficiency and gas quality trends, as reported in Figure 88 and Figure 89.

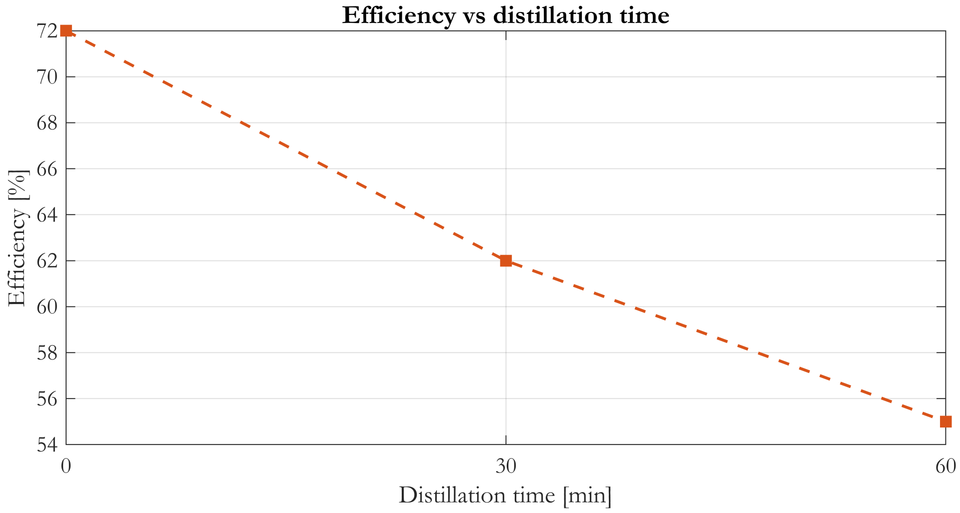

Figure 88: Efficiency trend with respect to distillation time.

Distillation time	Efficiency
0 min	72%
30 min	62%
60 min	55%

Table 55: Efficiency values at different distillation times.

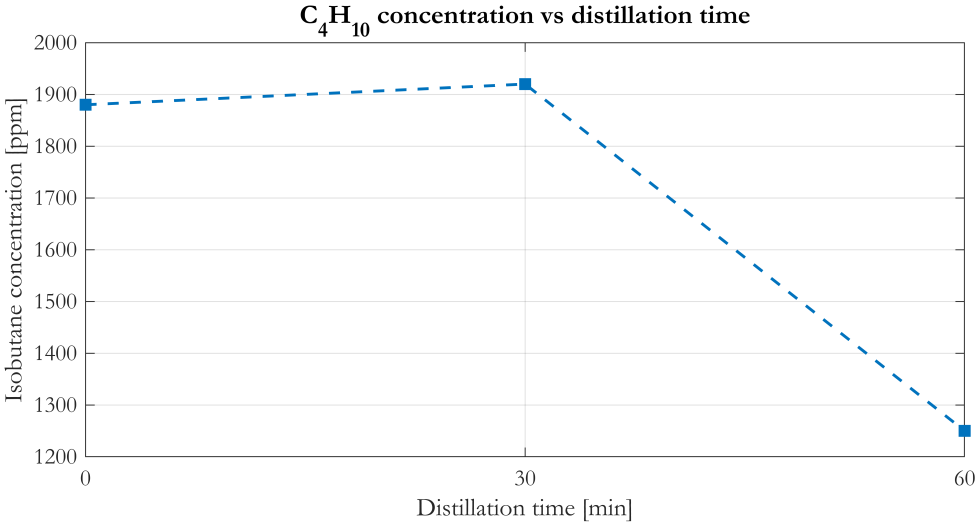

Figure 89: Gas quality trend with respect to distillation time.

Distillation time	**Isobutane concentration**
0 min	1880 ppm
30 min	1920 ppm
60 min	1250 ppm

Table 56: Isobutane concentrations at different distillation times.

From Figure 89 there is not an evident trend with respect to the distillation time. Indeed, the gas impurity is almost the same with 0 min and 30 min, while it decreases by 600 ppm between 30 min and 60 min distillation time. Therefore, it seems that 30 minutes are not enough to guarantee a gas quality improvement, while 60 minutes have a bigger influence on the isobutane concentration. In addition, distillation already occurs during the filling phase which lasts on average 2.5 hours with a filling rate of 400 l/h. Therefore, the addition of 30 minutes (20% of the filling time) is not significant to the distillation, while 60 minutes (40% of the filling time) have a larger impact on the overall distillation process. However, as illustrated in Figure 88, with 60 min distillation the system efficiency drops to 55%, which is too low for the required application.
In conclusion, considering that an efficiency of almost 80% is required and excluding the 30 minutes option, which does not guarantee a quality improvement than the case without distillation, the chosen optimal condition was the zero minutes distillation.

9 Optimal system configuration

The recovery system has achieved an optimal configuration in terms of filling and emptying flowrates, top buffer temperature and pressure, and bottom buffer temperature, knowing that the desired efficiency was 80% and the isobutane concentration upper limit was 1000 ppm, with negligible nitrogen and oxygen concentrations in the recovered mixture.
The optimal values, obtained during the testing phase, are reported in Table 57 with the average efficiency and gas quality in Table 58.

Parameter	**Value**
Filling rate	200 l/h
T_{Btop} **(Lauda setpoint)**	-36.2 °C
Lauda pump level	8
Top buffer pressure	10 mbar (C1&C2), 35 mbar (C3)
T_{Bbot} **(Huber setpoint)**	20 °C
Emptying rate	600 l/h
Distillation time	0 min
Operating columns	1,2,3

Table 57: Optimal values for the main working parameters of the R134a recovery system.

Component	**Value**
Average isobutane	715 ppm
Average nitrogen	12 ppm
Average oxygen	2 ppm
Efficiency	87%

Table 58: Average efficiency and concentrations with the optimal system configuration.

The recovery system is able to operate with three columns only due to the high C4 temperature. Indeed, the series connected cooling circuit is not enough to guarantee a uniform temperature for every columns, and each column has an influence on the ones downstream (see Figure 68).
An optimal filling rate of 200 l/h was chosen even if this parameter depends on the state of the RPCs. In particular, during the LHC running phase, the input flowrate may increase to 400 l/h. However, as mentioned in chapter 8.1, the filling rate does not influence the gas quality of the recovered mixture, and the efficiency may change by 5%.
The Lauda Integral XT 280 was set to -36.2 °C, at the maximum pump level (8) to minimise the temperature variations across the heat exchangers and guarantee a

temperature as uniform as possible in the cooling circuit. Even a small temperature variation (e.g., from -36.5 °C to -35.2 °C) strongly influences the efficiency and gas quality, since the system must work in a small temperature range, within -32.3 °C (T_{boil}^{Azeo}) and -26.4 °C (T_{boil}^{R134a}).

The second chiller unit, the Huber Ministat 125, was set to 20 °C in the optimal configuration, even if the bottom buffer temperature does not strongly influence the system efficiency and C_4H_{10} concentration (see chapter 8.5).

The Zimmerli were regulated at 10 mbar for the first two columns to face the problem related to their lower temperatures compared to C3 and C4, and improve the recoverd gas quality. On the contrary, C3 top pressure was set at 35 mbar to reduce the exhaust flowrate and improve the efficiency (see figures 73 and 74).

Finally, the needle valves were regulated to have and emptying rate of 600 l/h for each column, as explained in chapter 8.2.

10 Conclusions

A new gas recovery system for the R134a recuperation was installed and tested in the service gas room at the CMS experiment, with the aim of minimising the air pollution and purchasing cost. R134a, despite its high GWP (Global Warming Potential) represents the 95.2% of the mixture circulating in the RPCs (Resistive Plate Chambers) loop and must be separated from the other components, sulphur hexafluoride (SF_6) and isobutane (C_4H_{10}), which represents the 0.3% and 4.5% of the mixture, respectively. The tests aimed to find the optimal configuration to satisfy the requirements, derived from the previous two system prototypes, in terms of efficiency, at least 80% and gas quality, at most 1000 ppm of C_4H_{10}. In addition, different from the prototypes, the new recovery system was designed to work in continuous, 24 hours per day.
The system developed in four units: an electric rack, for the system automation, a distillation unit, made by a top and a bottom buffer for the separation process, a pumping and a storage units, for compressing and accumulate the recovered mixture. The main work was focused on the second unit, to understand and optimize the operating parameters such as the filling and emptying flowrates, the top buffer pressure and temperature, and the bottom buffer temperature.
Thermodynamic and chemical process simulations were performed, with COMSOL Multiphysics® software and AspenPlus® software, respectively. The first aimed to describe the velocity, the temperature and the phase fields in time, while the second software was used to simulate the real system as a differential distillation process and find the efficiency and gas quality trends modifying the main working parameters. Moreover, COMSOL Multiphysics® allowed to clarify the liquid/vapour behaviour inside each column: the liquid phase flows down from the top to the bottom buffer through a 10 mm diameter connecting pipe, evaporates and rises up in the top buffer, where condenses and releases heat to the liquid mixture, which increases its temperature. Then the light key component, the azeotropic mixture (T_{boil}^{Azeo}= - 32.3 °C), leaves the system through the exhaust, while the heavy key, the R134a, remains liquid (T_{boil}^{R134a}= - 26.4 °C).
The optimal configuration was achieved excluding column 4 due to its low efficiency ($<$ 20%), setting the Lauda Integral XT 280 at -36.2 °C, the Huber Ministat 125 at 20 °C, with an extraction flowrate of 600 l/h at the rotameter. Moreover, C1 and C2 worked with the Zimmerli set to 10 mbar, while C3 with 35 mbar. In addition, it was found out that the filling rate did not influence the gas quality, and thus, the system could operate at different input mixture flowrate. Under these conditions an efficiency of 87% and a isobutane concentration of 715 ppm were achieved.

Further studies may be focused on the cooling system, to modify the loop from a series to a parallel connection. This change would minimise the temperature interdependence between the four columns, reduce the temperature increment from C1 to C4, allowing to use also column 4. Moreover, the system performances could increase with the substitution of the "air cooled" Lauda Integral XT 280 with the "water cooled" Huber Unistat 910w, to minimise the influence of room temperature

on the cooling unit.
In addition, C1 and C2 bottom buffers, of 10 cm height, might be replaced by new ones, with the same dimensions of C3 and C4 (20 cm height) to maximise the effect of the warm buffer (bottom) on the cold buffer (top). Finally, the addition of a second compressor in the pumping unit, in parallel with the current one, would guarantee a system redundancy, fundamental for the continuity in the operations.

A Recovery system P&ID

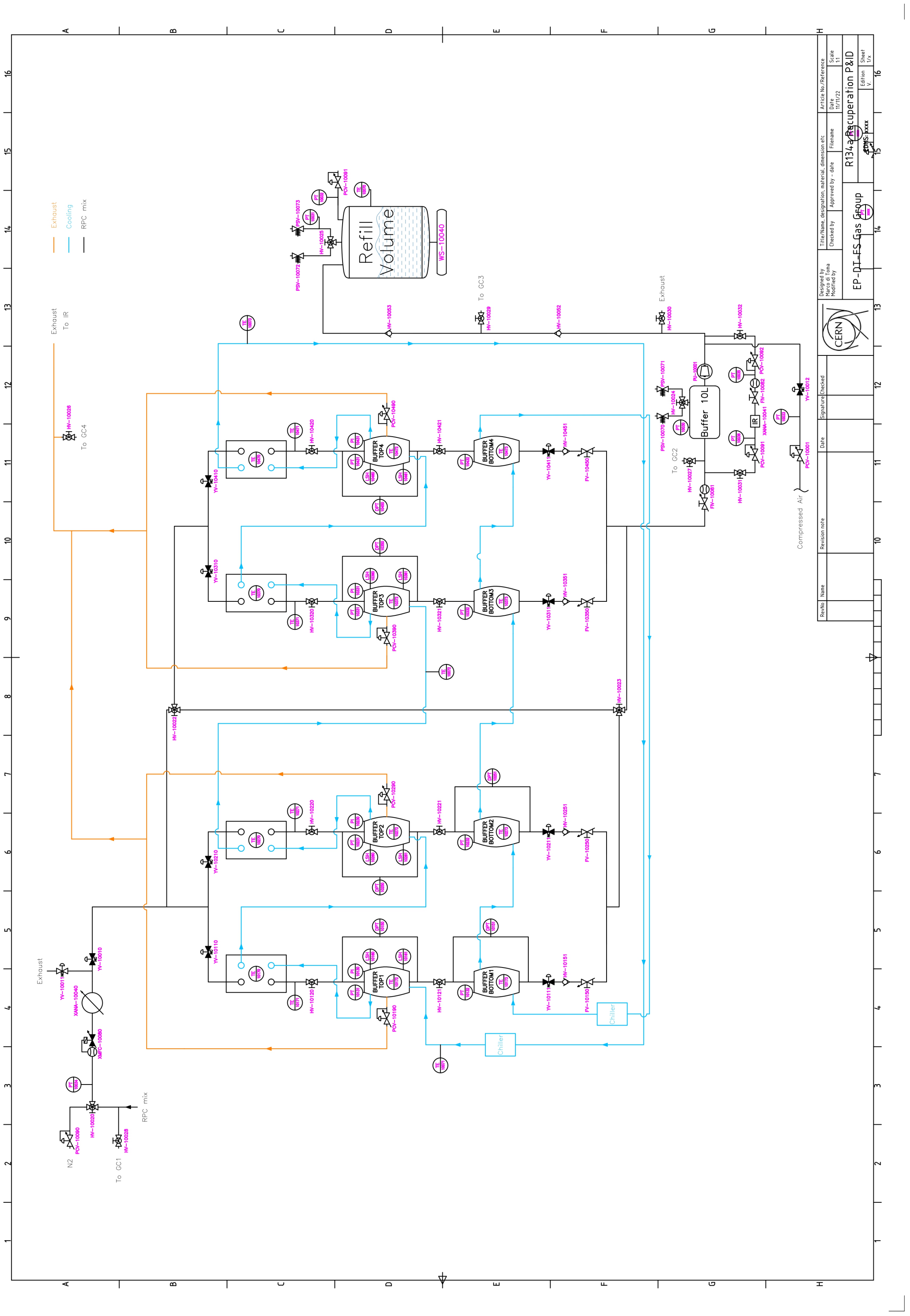

Figure 90: R134a recuperation system P&ID.

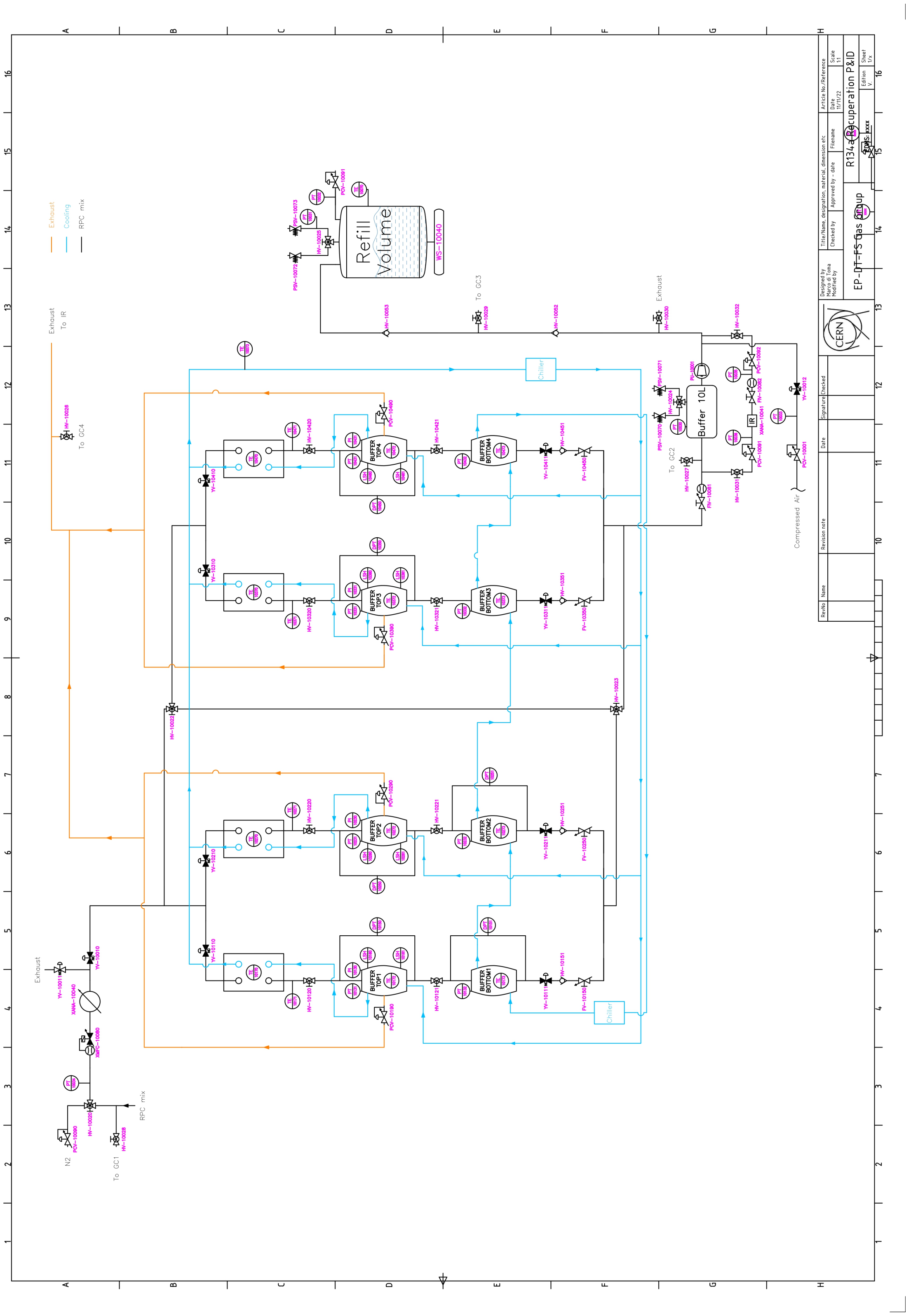

Figure 91: R134a recuperation system P&ID with cooling system in parallel.

B WinCC OA software interface

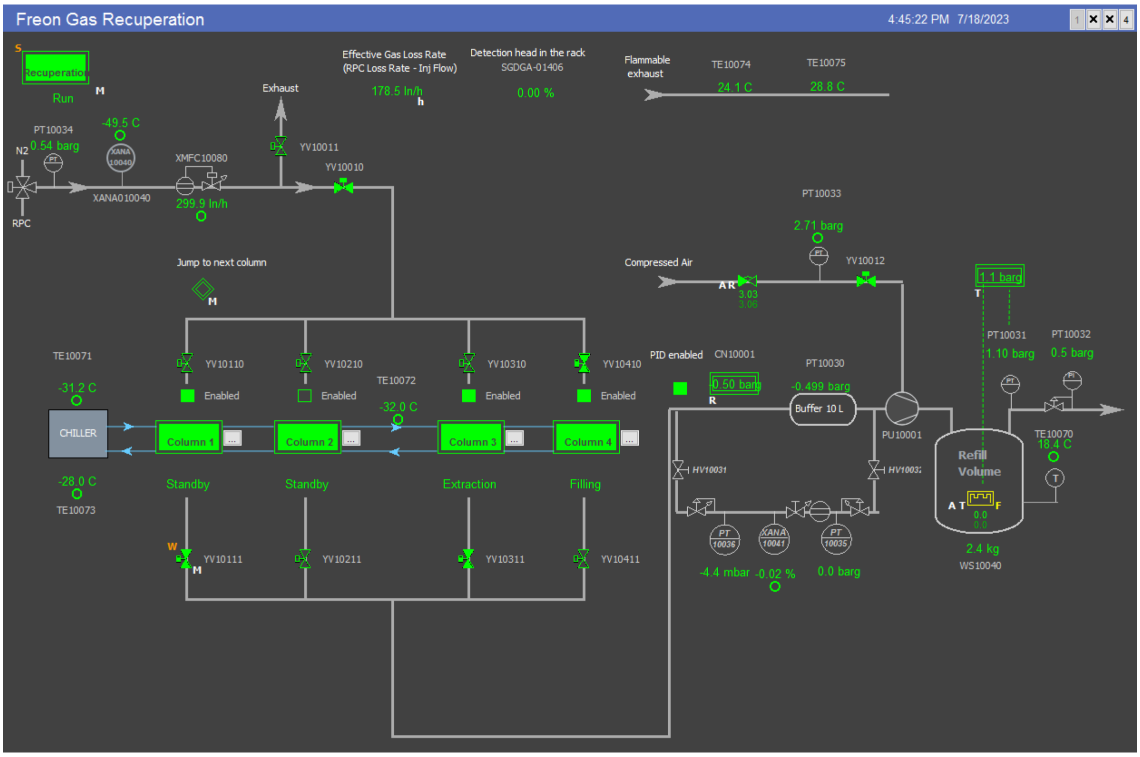

Figure 92: WinCC OA software interface. From the main window the four columns, the compressor and the recovery bottle are displayed, with the possibility to activate and deactivate the pneumatic valves, modify the input flowrate, read the pressure and temperature measurements.

C Buffers P&ID

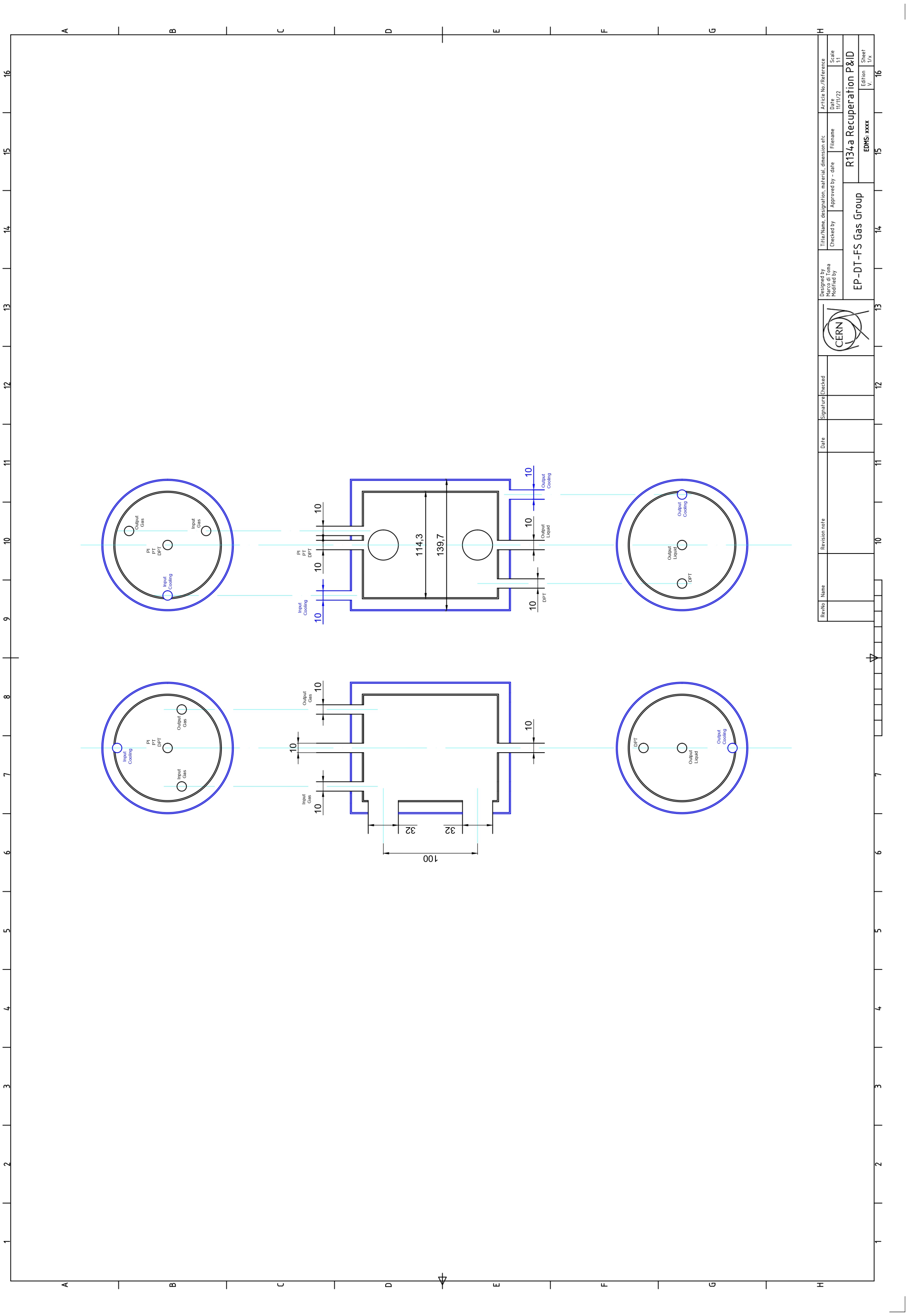

Figure 93: Buffer with a 10 cm height, used as bottom buffers for columns 1 and 2.

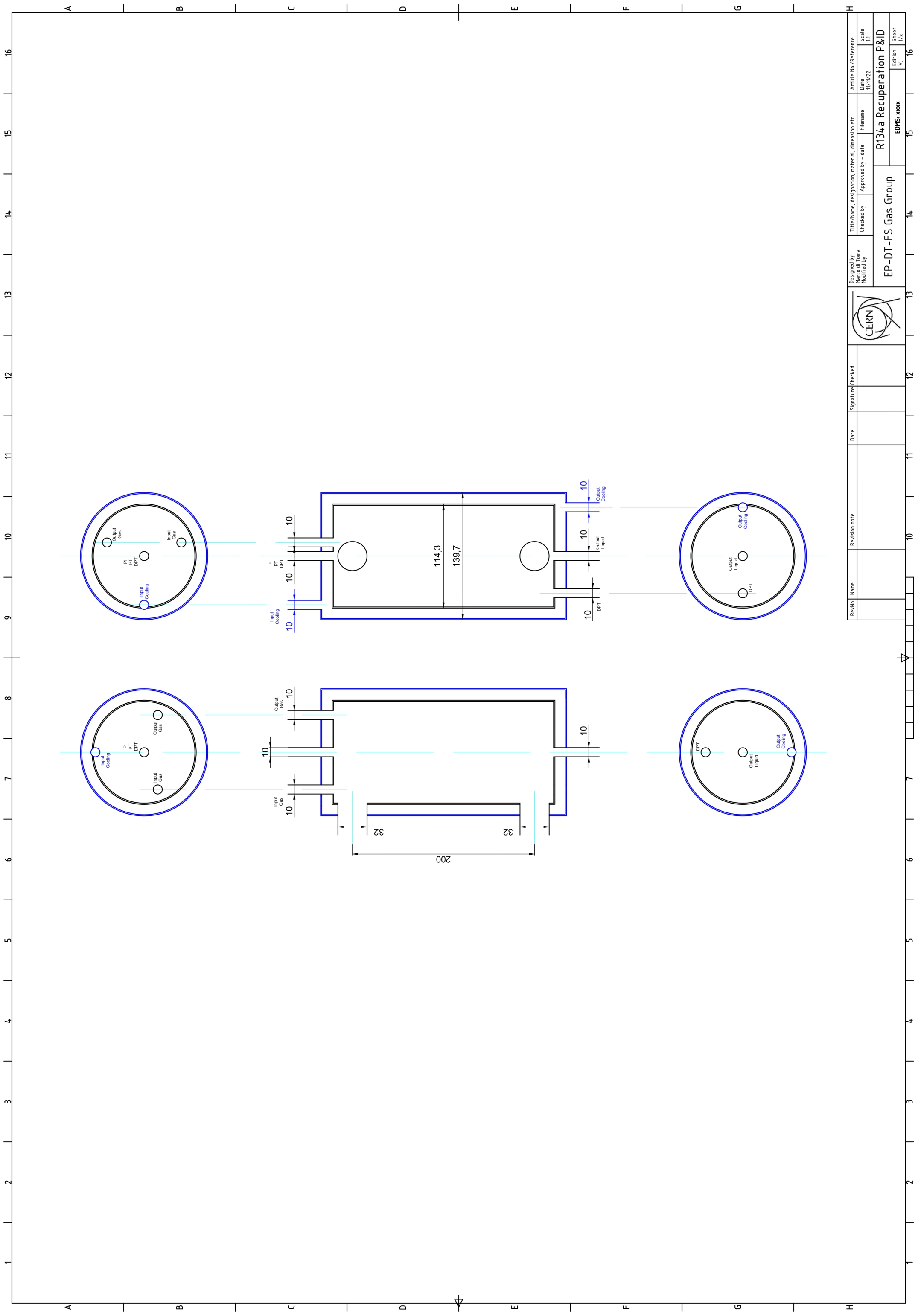

Figure 94: Buffer with a 20 cm height, used as top and bottom buffers for columns 3 and 4.

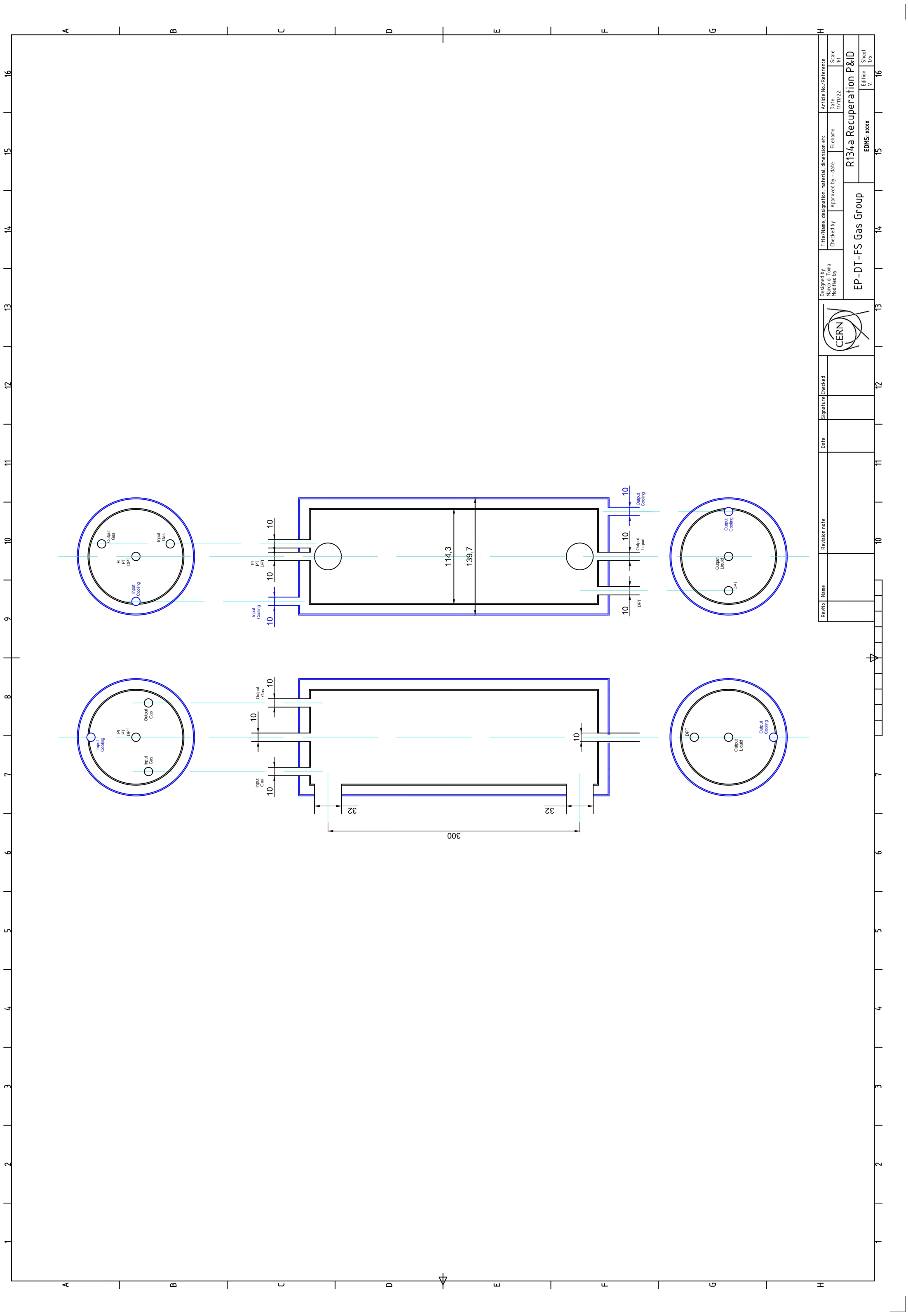

Figure 95: Buffer with a 30 cm height, used as top buffers for columns 1 and 2.

D Equilibrium diagrams

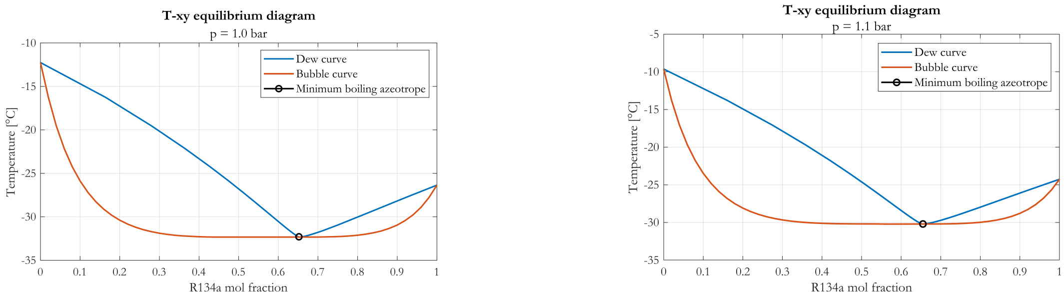

(a) 1.0 bara. **(b)** 1.1 bara.

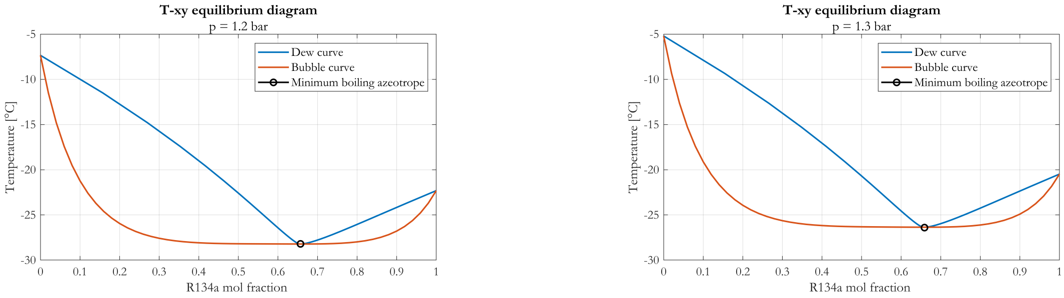

(c) 1.2 bara. **(d)** 1.3 bara.

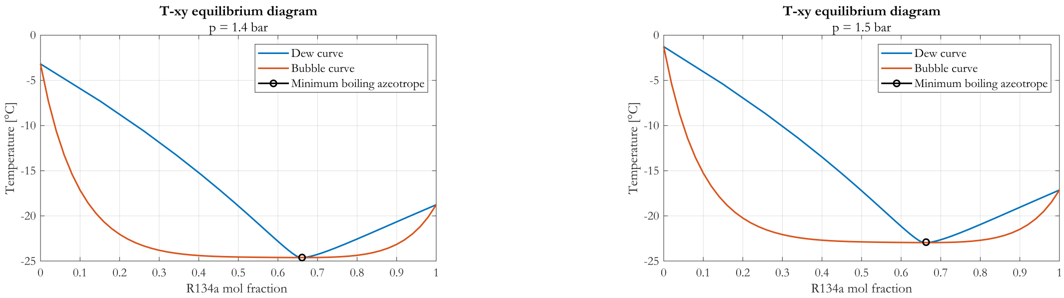

(e) 1.4 bara. **(f)** 1.5 bara.

Figure 96: Equilibrium diagrams for 6 different pressure values, from 1.0 bara to 1.5 bara.

References

[1] United Nations. Paris agreement, 2015.

[2] Resistive plate chambers overview. `https://project-cms-rpc-endcap.web.cern.ch/rpc/ISR/CMS%20presentations/TDR/cms-rpc-tech-note.pdf`.

[3] R. Guida and B. Mandelli. R&D strategies for optimizing greenhouse gases usage in the lhc particle detection systems. *Nuclear Instruments and Methods in Physics Research Section A: Accelerators, Spectrometers, Detectors and Associated Equipment*, 958:162135, 2020. Proceedings of the Vienna Conference on Instrumentation 2019.

[4] Ozone Protection and Synthetic Greenhouse Gas Management Regulations. Global warming potential values of hydrofluorocarbon refrigerants. `https://www.dcceew.gov.au/environment/protection/ozone/rac/global-warming-potential-values-hfc-refrigerants`, 1995.

[5] United States Environmental Protection Agency. Overview of grenhouse gases - emissions of fluorinated gases. `https://www.epa.gov/ghgemissions/overview-greenhouse-gases`, 2021.

[6] United States Environmental Protection Agency. Inventory of u.s. greenhouse gas emissions and sinks. `https://www.epa.gov/ghgemissions/inventory-us-greenhouse-gas-emissions-and-sinks`, 2021.

[7] R. Guida, M. Capeans, F. Hahn, S. Haider, and B. Mandelli. The gas systems for the *lhc* experiments. In *2013 IEEE Nuclear Science Symposium and Medical Imaging Conference (2013 NSS/MIC)*, pages 1–7, 2013.

[8] European Parliament and Council. Regulation (eu) no 517 on fluorinated greenhouse gases. `https://eur-lex.europa.eu/legal-content/EN/TXT/PDF/?uri=CELEX:32014R0517&from=EN`, 2014.

[9] Bukola O. Bolaji. Theoretical assessment of new low global warming potential refrigerant mixtures as eco-friendly alternatives in domestic refrigeration systems. *Scientific African*, 10, 2020.

[10] United States Environmental Protection Agency. Sulfur hexafluoride (sf6) basics. `https://www.epa.gov/eps-partnership/sulfur-hexafluoride-sf6-basics`, 2023.

[11] Beatrice Mandelli, Mara Corbetta, Roberto Guida, and Gianluca Rigoletti. Strategies for reducing the use of greenhouse gases from particle detectors operation at the cern lhc experiments. *Journal of Physics: Conference Series*, 2374(1):012159, nov 2022.

[12] Rolf-Dieter Heuer. The future of the large hadron collider and cern. *Philosophical Transactions of the Royal Society A: Mathematical, Physical and Engineering Sciences*, 370(1961):986–994, 2012.

[13] CERN. CERN's accelerator complex. `https://home.cern/science/accelerators/accelerator-complex`.

[14] CERN. The third run of the Large Hadron Collider has successfully started. `https://home.cern/news/news/cern/third-run-large-hadron-collider-has-successfully-started`.

[15] CERN. The CMS detector, CMS experiment. `https://cms.cern/detector`.

[16] *Basics of Resistive Plate Chambers*, chapter 3, pages 45–110. John Wiley & Sons, Ltd, 2018.

[17] The CMS Collaboration and S Chatrchyan and G Hmayakyan and V Khachatryan and A M Sirunyan and W Adam and T Bauer and T Bergauer and H Bergauer and M Dragicevic. The CMS experiment at the CERN LHC. *Journal of Instrumentation*, 3(08):S08004, aug 2008.

[18] CERN. Resistive Plate Chambers. `https://cms.cern/detector/detecting-muons/resistive-plate-chambers`.

[19] US Lepartment of Labor. Occupational safety and health administration. `https://www.osha.gov/chemicaldata/577`.

[20] S. T. Sehgal, R. Sehgal, and Lalit Mohan Pant. Humidifier for rpc gas mixture for bakelite rpcs. *Proceeding on of the DAE Symp. on Nucl Phys.*, 56:1062–1063, 2011.

[21] R. Guida and B. Mandelli. A portable gas recirculation unit for gaseous detectors. *Journal of Instrumentation*, 12(10), 2017.

[22] M. di Toma. Development of a prototype for the recovery of R134a from the mixture of RPCs detectors. *Politecnico di Torino, EP-DT-FS gas group*, March 2023.

[23] F. Cambié. R134a separation and recuperation from the gaseous mixture used in the Resistive Plate Chamber detectors at the CMS Experiment. *Università di Pavia, EP-DT-FS gas group*, October 2021.

[24] National Institute of Standards and Technology. NIST Chemistry WebBook, Standard Reference Database Number 69. `https://webbook.nist.gov/chemistry/#CreditsControl`, 2023.

[25] AspenTech. AspenPlus v10. `https://www.aspentech.com/en/products/engineering/aspen-plus`.

[26] Siemens. SIMATIC WinCC OA - Basic Software. `https://www.siemens.com/global/en/products/automation/industry-software/automation-software/scada/simatic-wincc-oa/wincc-oa-basic-software.html`.

[27] Hydraulic International Inc. Pumps Division. Air driven gas boosters - low pressure, high flow, oil-free. `https://hiipumps.com/wp-content/uploads/GB502C.pdf`.

[28] Robert Ewald Treybal. *Mass-transfer Operations*. Chemical engineering series. McGraw-Hill, 1980.

[29] G. Fieg. Distillation Design and Control Using Aspen Simulation. Von W. L. Luyben. *Chemie Ingenieur Technik*, 87, 03 2015.

[30] M. Iggland and M. Mazzotti. Introduction to Chemical Engineering for Lecture 7: Flash Distillation. `https://ethz.ch/content/dam/ethz/special-interest/mavt/process-engineering/separation-processes-laboratory-dam/documents/education/tvt%20exercises/notes_2020/ICE_Script_Flash.pdfl`.

[31] Univarsity of Washington. Distillation columns. `https://faculty.washington.edu/finlayso/Polyeth/Group_A/page5a.html`.

[32] B.S. Thirumalesh and V. Ramesh. Case study on multicomponent distillation and distillaton column sequencing. *International Journal of Engineering Science & Research Technology*, 4:609–623, 2015.

[33] Douw Faurie, Justin Mbwebwe, and Molelekoa Mosesane. Gas chromatography calibration curve for siloxanes analysis. 11 2018.

[34] B. Mandelli and M. Corbetta. Gas chromatograph. 1 2019.

[35] M Capeans, Rosa Guida, F Hahn, Stefan Haider, and B Mandelli. RPC performances and gas quality in a closed loop gas system for the new purifiers configuration at LHC experiments. *Journal of Instrumentation*, 8:T08003, 08 2013.

[36] COMSOL. COMSOL Multiphysics Simulation Software. `https://www.comsol.com/comsol-multiphysics`.

[37] Aspen Technology, Inc. Aspen Plus User Guide, Version 10.2. `https://web.ist.utl.pt/ist11038/acad/Aspen/AspUserGuide10.pdf`.

[38] T.L. Bergman, A.S. Lavine, and D.P. DeWitt. *Introduction to Heat Transfer, 6th Edition*. Wiley, 2011.

[39] COMSOL. Two Methods for Modeling Free Surfaces in COMSOL Multiphysics. `https://www.comsol.com/blogs/two-methods-for-modeling-free-surfaces-in-comsol-multiphysics/`, 2018.

[40] Fang Chen. A survey of interface tracking methods in multi-phase fluid visualization. volume 19, pages 11–19, 01 2010.

[41] COMSOL. Two-Phase Flow Modeling Guidelines. `https://www.comsol.com/support/learning-center/article/Two-Phase-Flow-Modeling-Guidelines-46471`.

[42] COMSOL. The Wetted Wall Coupling Feature. `https://doc.comsol.com/6.0/doc/com.comsol.help.cfd/cfd_ug_fluidflow_multi.09.011.html`.

[43] D. Burragato. R134a separation and recuperation prototype for the Resistive Plate Chamber detectors at the CMS Experiment. *Università di Pavia, EP-DT-FS gas group*, 2022.

[44] LAUDA. Operating instructions, Integral XT, Process thermostats and High-temperature thermostats. `https://www.lauda.de/de/]`.

[45] Huber. Operation manual, Unistat-Pilot ONE. `https://www.huber-online.com/]`.

[46] Zimmerli. Messtechnik Ad Manual . `https://www.zimmerliag.com/wp-content/uploads/datenblatt_pdf/druckregler/ZM-R15/GS_ZM-R15_def_R05.pdf]`.

Acknowledgement

Un sentito grazie a tutte le persone che mi hanno permesso di arrivare fin qui e di portare a termine il mio percorso di studi.

Per prima cosa, vorrei ringraziare i miei relatori, Roberto Guida, Vittorio Verda e Martina Capone per i preziosi consigli e per la disponibilità.

Un ringraziamento speciale va ai colleghi e amici del gas team del CERN, in particolare a Maria Cristina, Damiano, Fabio, Stefania, Gianluca, Mattia V., Mattia B. e Bianca, per il loro supporto e per tutti i momenti trascorsi insieme.

Ringrazio i miei genitori e mio fratello Francesco, per la loro infinita pazienza e costante presenza in ogni istante del percorso di studi.

Grazie a tutti gli amici caragliesi, con un pensiero particolare a Filippo, che da lassù mi guida nelle scelte più difficili, agli amici di Torino e del Collegio Universitario Crocetta, per tutti i momenti di difficoltà e spensieratezza condivisi insieme.